

Effective field theory description of halo nuclei

H.-W. Hammer^{1,2}, C. Ji^{3,4}, and D. R. Phillips⁵

¹ Institut für Kernphysik, Technische Universität Darmstadt, 64289 Darmstadt, Germany

² ExtreMe Matter Institute EMMI, GSI Helmholtzzentrum für Schwerionenforschung, 64291 Darmstadt, Germany

³ ECT*, Villa Tambosi, 38123 Villazzano (Trento), Italy

⁴ INFN-TIFPA, Trento Institute for Fundamental Physics and Applications, Trento, Italy

⁵ Institute of Nuclear and Particle Physics and Department of Physics and Astronomy, Ohio University, Athens, OH 45701, USA

E-mail: hammer@theorie.i.kp.physik.tu-darmstadt.de, ji@ectstar.eu, phillid1@ohio.edu

Abstract. Nuclear halos emerge as new degrees of freedom near the neutron and proton driplines. They consist of a core and one or a few nucleons which spend most of their time in the classically-forbidden region outside the range of the interaction. Individual nucleons inside the core are thus unresolved in the halo configuration, and the low-energy effective interactions are short-range forces between the core and the valence nucleons. Similar phenomena occur in clusters of ^4He atoms, cold atomic gases near a Feshbach resonance, and some exotic hadrons. In these weakly-bound quantum systems universal scaling laws for s-wave binding emerge that are independent of the details of the interaction. Effective field theory (EFT) exposes these correlations and permits the calculation of non-universal corrections to them due to short-distance effects, as well as the extension of these ideas to systems involving the Coulomb interaction and/or binding in higher angular-momentum channels. Halo nuclei exhibit all these features. *Halo EFT*, the EFT for halo nuclei, has been used to compute the properties of single-neutron, two-neutron, and single-proton halos of s-wave and p-wave type. This review summarizes these results for halo binding energies, radii, Coulomb dissociation, and radiative capture, as well as the connection of these properties to scattering parameters, thereby elucidating the universal correlations between all these observables. We also discuss how Halo EFT's encoding of the long-distance physics of halo nuclei can be used to check and extend *ab initio* calculations that include detailed modeling of their short-distance dynamics.

Contents

1	Introduction	3
2	s-wave halos	8
2.1	Lagrangian	8
2.2	Two-body amplitude	10
2.3	Applications: one-neutron s-wave halos	14
2.4	Applications: unbound s-wave neutron-core systems	16
2.5	The three-body amplitude	18
2.6	Applications: Efimov states and matter radii	23
2.7	Range corrections in three-body systems	27
3	Halos beyond the s-wave	29
3.1	Lagrangian	29
3.2	Two-body amplitude	30
3.3	Properties of the p-wave two-body bound state	31
3.4	Power counting, pole structure, and bounds from causality	32
3.5	Universality and the unitary limit in p-waves	34
3.6	Applications: ^{11}Be and ^8Li	35
3.7	Application: low-lying $^2\text{P}_{3/2}$ resonance in ^5He	38
3.8	The three-body equations in the case of ^6He	38
3.9	Absence of the Efimov effect	43
3.10	Higher partial waves	44
4	Electromagnetic reactions on halo nuclei	44
4.1	Lagrangian: electromagnetic sector	44
4.2	Coulomb Dissociation of a one-neutron s-wave halo	46
4.3	The role of p-wave final-state interactions	51
4.4	Application to ^{19}C and ^{11}Be	51
4.5	Electric radius for s-wave halos	52
4.6	Application: electric radii of one-neutron halos	54
4.7	Sum rules for the dipole strength	55
4.8	Bound-state observables for p-wave halos	55
4.9	Application: radius of and E1 transition to $1/2^-$ state in ^{11}Be	58
4.10	Radiative capture into a p-wave halo	59
4.11	Electromagnetic radii of two-neutron halos	62
4.12	Coulomb dissociation of two-neutron halos	63
5	Halo EFT with Coulomb	63
5.1	Formalism	63
5.2	Renormalization	67
5.3	Applications to Scattering	69

5.4	Form Factors	71
5.5	Radiative Capture	73
5.6	Fine tuning in s-wave proton halos	77
5.7	Radiative capture in p-wave proton halos: ${}^7\text{Be}(p, \gamma){}^8\text{B}$ and solar neutrinos	79
6	Comparison with other approaches	83
7	Conclusion, sins of omission, and future paths	88
7.1	Summary	88
7.2	Sins of omission	89
7.3	Future paths	91

1. Introduction

The emergence of new degrees of freedom is an intriguing aspect of the physics of nuclei away from the valley of stability. In particular, certain nuclei near the neutron and proton driplines form halo states which consist of a tightly bound core and a few halo nucleons that are weakly bound to the core [1, 2, 3, 4, 5]. Neutron halos were discovered in the 1980s at radioactive beam facilities and are characterized by an unusually large interaction radius [6]. Jonson and Hansen showed that this large radius is connected to a small separation energy of the halo neutrons [7]. The emergence of the halo structures can be considered a consequence of the quantum tunneling of halo neutrons out of the effective potential of the core to the classically forbidden region.

The simplest example of a halo nucleus is the deuteron, which can be considered a one-neutron halo nucleus with a proton core. The root mean square charge radius of the deuteron is about three times as large as the size of the constituent proton. We shall discuss other examples of one-neutron halo nuclei, with more complex cores, below. Meanwhile, halo nuclei with two valence nucleons exhibit three-body dynamics. The case in which the corresponding one-nucleon halo is beyond the dripline is particularly interesting, as then none of the two-body subsystems in the three-body system is bound. This makes the two-neutron halo an example of a Borromean three-body problem; the name stems from the heraldic symbol of the Borromeo family of Italy, in which three rings are interlocked in such a way that if any one of the rings is removed all three separate. The most carefully studied Borromean halo nuclei are ${}^6\text{He}$ and ${}^{11}\text{Li}$, each of which has two weakly bound valence neutrons [1]. In the case of ${}^6\text{He}$, the core is a ${}^4\text{He}$ nucleus. The two-neutron separation energy for ${}^6\text{He}$ is about 1 MeV, and thus small compared to the binding and excitation energies of the ${}^4\text{He}$ core which are about 28 and 20 MeV, respectively. There is a strong p-wave resonance in the $J^P = 3/2^-$ channel of $n\alpha$ -scattering—sometimes referred to as “ ${}^5\text{He}$ ”, even though the nucleus is not bound. This resonance is crucial for the binding of ${}^6\text{He}$, and so ${}^6\text{He}$ can be regarded as dominated by configurations consisting of an α -particle and two neutrons, both of which are in a $p_{3/2}$ wave relative to the α core.

The separation of scales in halo nuclei can be exploited using effective field theory (EFT) †. EFT provides a general framework to calculate the low-energy behavior of a physical system in an expansion of short-distance over large-distance scales. The underlying principle is that short-distance physics is not resolved at low energies and may be included implicitly in “low-energy constants”, while long-distance physics must be treated explicitly. For the dynamics of the halo nucleons, the substructure of the core can be considered short-distance physics, although low-lying excited states of the core sometimes have to be included explicitly.

Halo nuclei can be described by extensions of the pionless EFT for few-nucleon systems [14, 15, 16, 17]. One assumes the core to be structureless and treats the nucleus as a few-body system of the core and the valence nucleons, introducing independent field operators for the halo nucleons and the core. At leading order the core is thus a structureless object. Corrections from its structure appear at higher orders in the EFT expansion, and can be accounted for in perturbation theory. The philosophy of Halo EFT is similar to that of cluster models but EFT organizes different cluster-model effects into a controlled expansion based on the scale separation, thereby facilitating estimation of the theory’s uncertainties. A new facet compared to few-nucleon systems is the appearance of resonant interactions in higher partial waves—as in the neutron- α system [18, 19]. This leads to a much richer structure of the EFT. However, there are many halo nuclei where s-wave interactions are dominant, such as ^{19}C and ^{22}C .

In order to motivate the Halo EFT approach, we start with these simpler systems. The scattering of the core and halo nucleons at sufficiently low energy is then determined by their s-wave scattering length a_0 . We consider distinguishable particles of equal mass m and degenerate pair scattering lengths a_0 for simplicity. This scenario applies approximately to the triton considered as a two-neutron halo nucleus. If a_0 is much larger than the range of the interaction R , the system shows universal properties [20, 21, 22]. The simplest example is the existence of a shallow two-body bound state with binding energy and mean square separation

$$B_2 = \frac{1}{ma_0^2} \quad \text{and} \quad \langle r^2 \rangle = a_0^2/2, \quad (1)$$

if a_0 is large and positive. ‡ The leading corrections to these universal expressions are of relative order R/a_0 and can be calculated using the EFT discussed in this review. The deuteron binding energy is described by Eq. (1) to within 35% accuracy; this improves to 12% accuracy if the leading range correction is included.

If a third particle is added the two-particle s-wave scattering length no longer determines the low-energy properties of the system. Observables such as the binding energy of three-body bound states and low-energy scattering phase shifts are markedly affected by short-distance physics in the three-body system [23, 24]. This additional dynamics can be characterized by a single “three-body parameter”, κ_* . All low-energy observables in the three-body system are then functions of a_0 and κ_* —to leading order

† Those desiring a pedagogical introduction to EFT are referred to Refs. [8, 9, 10, 11, 12, 13].

‡ We use natural units with $\hbar = c = 1$ throughout this review.

in R/a_0 . For fixed scattering length, this implies universal correlations between different three-body observables such as the Phillips line [25]. Moreover, the Efimov effect [26] generates a universal spectrum of three-body bound states with binding energy †

$$B_3 = -\frac{1}{ma_0^2} + [e^{-2\pi n} f(\xi)]^{1/s_0} \frac{\kappa_*^2}{m}, \quad (2)$$

where the index n labels the three-body states, κ_* is a three-body parameter, $s_0 = 1.00624\dots$ is a transcendental number, $f(\xi)$ is a universal function with $f(-\pi/2) = 1$, and the angle ξ is defined by $\tan \xi = -(mB_3)^{1/2} a_0$. The leading corrections to Eq. (2) are again of relative order R/a_0 . The corresponding spectrum is illustrated in Fig. 1 in

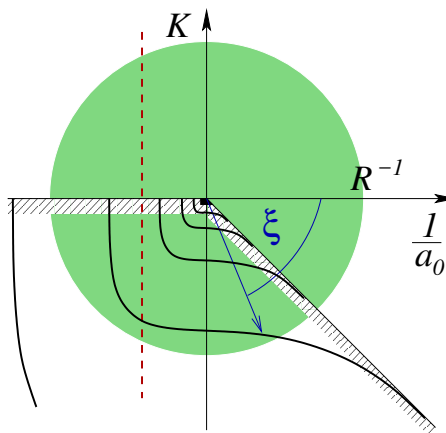


Figure 1. Illustration of the Efimov spectrum: The energy variable $K = \text{sgn}(E)\sqrt{m|E|}$ is shown as a function of the inverse scattering length $1/a_0$. The shaded circular region exhibits the window of universality. The solid lines indicate the Efimov states, while the hashed areas give the scattering thresholds and the dashed vertical line illustrates an exemplary system with fixed scattering length.

the two-dimensional plane spanned by the momentum variable $K = \text{sgn}(E)\sqrt{m|E|}$ and the inverse scattering length $1/a_0$. The shaded circular area of radius R^{-1} indicates the region where universality applies (“window of universality”). The solid lines indicate the Efimov states while the hashed areas give the scattering thresholds below which the bound states can exist. The dashed vertical line illustrates an exemplary system with a fixed scattering length. In the unitary limit $1/a_0 = 0$, Eq. (2) reduces to the geometric spectrum

$$B_3 = e^{-2\pi n/s_0} \frac{\kappa_*^2}{m}, \quad (3)$$

and it is obvious that the three-body parameter κ_* is simply the binding momentum of the state with $n = 0$.

The spectrum shown in Fig. 1 is invariant under discrete scaling transformations by the factor $\lambda_0 = e^{\pi/s_0}$:

$$\kappa_* \longrightarrow \kappa_*, \quad a_0 \longrightarrow \lambda_0^n a_0, \quad B_3 \longrightarrow \lambda_0^{-2n} B_3, \quad (4)$$

† See Ref. [27] for more details.

where n is any integer. This discrete scale invariance holds for all three-body observables. Its manifestation in observables is often referred to as *Efimov physics*.

If more particles are added, no new parameters are needed for renormalization at leading order [28, 29, 30, 31, 32]. As a consequence, in the universal regime all four-body observables are also governed by the discrete scaling symmetry (4), and can be characterized by a_0 and κ_* [33, 34, 35, 36, 37]. A similar behavior is expected for higher-body observables [38, 39, 40, 41, 42, 43, 44, 45, 46, 47, 48]. In ultracold atoms, these properties have now been experimentally verified for up to five particles [49, 50, 51].

The observation of this discrete scaling symmetry in the level spectra of halo nuclei is a topic of current research [52, 53], but the contribution of higher partial waves and partial-wave mixing complicate the situation. While Halo EFT naturally accommodates resonant interactions in higher partial waves [18, 19], there is no Efimov effect in this case [54, 55, 56]. Moreover, universality for resonant p-wave interactions is weaker as two parameters, the p-wave scattering volume and effective range, are required already at leading order in the two-body system. In higher partial waves this pattern gets progressively worse [18, 57, 58]. Nevertheless, universality still provides powerful constraints for the structure and dynamics of halo nuclei [59, 52].

We use the universality of resonant interactions as the starting point for Halo EFT. In principle, this framework is applicable to any system with short-range interactions and large scattering lengths. The breakdown scale M_{core} of this theory is set by the lowest momentum degree of freedom not explicitly included in the theory. The EFT exploits the appearance of a large scattering length $a_0 \gg 1/M_{\text{core}}$, independent of the mechanism generating it. In addition to nuclear halo states, examples include ultracold atoms close to a Feshbach resonance and hadronic molecules in particle physics. The typical momentum scale of the theory is $M_{\text{halo}} \sim 1/a_0 \sim k$, which for the systems under consideration here is usually \sim tens of MeV. Meanwhile, the Halo EFT breakdown scale, M_{core} , varies between 50 and 150 MeV, depending on the system. The expansion is then in powers of $M_{\text{halo}}/M_{\text{core}}$, and for a calculation to order n the omitted short-range physics should affect the EFT's answer by a fractional amount of order $(M_{\text{halo}}/M_{\text{core}})^{n+1}$ —as long as we consider a process at a momentum $\sim M_{\text{halo}}$. (A more sophisticated implementation of this prescription that employs Bayesian methodology to update the size of the error bar based on the convergence of the perturbative series can be found in Refs. [60, 61].) For momenta of the order of the breakdown scale M_{core} or above the EFT expansion diverges: the omitted short-range physics is resolved and has to be treated explicitly.

The fact that the halo nucleons and the core are assigned distinguishable-particle field operators in Halo EFT means that the halo nucleons are not antisymmetrized with nucleons in the core—the latter are not active degrees of freedom in the EFT. (See Fig. 2 for an illustration in the case of ${}^6\text{He}$ treated as $\alpha + n + n$.) However, the contribution of a hypothetical configuration where a nucleon from the core and from the halo are exchanged to an observable is governed by the overlap of the wave functions of the core and the halo. Since the ranges of the core and halo wave functions

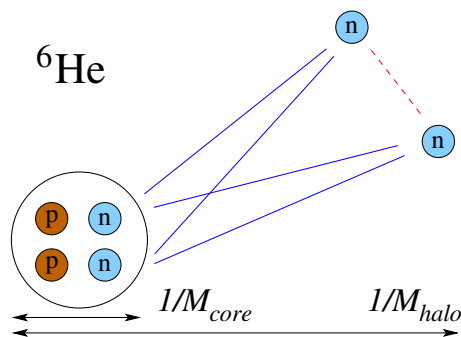


Figure 2. Illustration of the antisymmetrization of neutrons in the halo nucleus ${}^6\text{He}$ treated as $\alpha + n + n$ in the framework of Halo EFT. The exchange illustrated by the dashed line involves active degrees of freedom and is antisymmetric, while the exchanges indicated by the solid lines are not included.

are $1/M_{\text{core}}$ and $1/M_{\text{halo}}$, respectively, the contribution is determined by the standard Halo EFT expansion in $M_{\text{halo}}/M_{\text{core}}$. Therefore, within the domain of applicability of Halo EFT the impact of anti-symmetrization on observables is controlled and can be incorporated together with that of other short-distance effects. In a single-nucleon halo, these effects enter through the low-energy constants of the nucleon-core interaction which is fitted to experimental data or *ab initio* input. In a two-nucleon halo, they also enter through a short-range three-body force. This can be understood as follows: the full anti-symmetrization of the wave function in a theory with active core nucleons will result in additional nodes of the halo wave function since some nucleons must be in excited states to obey the Pauli principle. In a cluster model, these additional nodes are generated by including deep unphysical bound states (ghost states) of the core and the halo (see, e.g., Ref. [62]). In halo EFT such deep unphysical states are not included explicitly. The manifestation of the corresponding physics in halo EFT can be understood by assuming that the unphysical states have been integrated out of the theory. This generates a short-range three-body force between the core and the two halo nucleons (or modifies an already existing three-body force in the theory).

Halo EFT is not meant to replace *ab initio* approaches to halo nuclei, instead it complements *ab initio* approaches by providing universal relations between different halo observables. Thus it presents a unified framework for the description of different halo nuclei and their properties. On the one hand, these universal relations can be combined with inputs from *ab initio* theories or experiments to predict halo properties. On the other hand, they can be used to test calculations and/or measurements of different observables for their consistency. In Section 2.6 we will use such relations to elucidate tensions between different pieces of data on the ${}^{21}\text{C}$ and ${}^{22}\text{C}$ isotopes, while in Section 4.4 we will revisit the story of ${}^{19}\text{C}$, where universal scaling relations, together with accurate Coulomb-excitation data, diagnosed a problem with the one-neutron separation energy assigned to that nucleus [63]. A similar application of universal relations to identify inconsistencies in calculations for systems of ${}^4\text{He}$ atoms can be found in Refs. [64, 65].

Finally, Halo EFT provides a systematic framework to estimate the natural accuracy limits of cluster models, e.g., for electromagnetic observables it can be used to determine the order at which local gauge-invariant couplings to an external current appear.

The review is organized as follows. In Section 2, we review the Halo EFT formalism for s-wave halos and discuss some key applications. The extension to halos beyond the s-wave is presented in Section 3. The inclusion of electromagnetic interactions follows in Section 4, while the case of proton halos—where Coulomb interactions play a key role—is discussed in Section 5. The body of the review ends with a discussion of Halo EFT’s connection to and synergies with other approaches in Section 6. Section 7 gives a brief summary, treats some outstanding points, and describes a few out of the many possible directions for future work.

2. s-wave halos

2.1. Lagrangian

In order to describe halo nuclei in a non-relativistic EFT framework, it is important to establish formulae for observables in halos that are generally suitable for all systems under consideration, and then apply those formulae to specific cases under consideration. We first focus on one- and two-neutron halos with s-wave interactions between the core and the valence neutrons. We introduce an effective Lagrangian density \mathcal{L} to describe a general s-wave halo consisting of a core (c) with spin ζ_c and mass m_c and one or two valence neutrons (n) with spin 1/2 and mass m_n . \mathcal{L} is written as a sum of one-, two-, and three-body components,

$$\mathcal{L} = \mathcal{L}_1 + \mathcal{L}_2 + \mathcal{L}_3. \quad (5)$$

The one-body part contains the kinetic terms for the neutron spin-doublet field $n \equiv \begin{pmatrix} n_\uparrow \\ n_\downarrow \end{pmatrix}$ and the core $(2\zeta_c + 1)$ -component spinor field c

$$\mathcal{L}_1 = n^\dagger \left(i\partial_0 + \frac{\nabla^2}{2m_n} \right) n + c^\dagger \left(i\partial_0 + \frac{\nabla^2}{2m_c} \right) c. \quad (6)$$

The two-body s-wave neutron-neutron (nn) and neutron-core (nc) short-range interactions are represented by contact terms. The two valence neutrons interact in a spin-singlet state, which has an unnaturally large scattering length. The neutron and the core couple into states with total spin s , whose values can be $s_- = |\zeta_c - 1/2|$ and $s_+ = \zeta_c + 1/2$ †. We write the two-body Lagrangian containing both the nn and nc contact interactions as

$$\mathcal{L}_2 = -C_{nn} [nn]_{0,0}^\dagger [nn]_{0,0} - C_{nc(-)} [nc]_{s_-, \beta_-}^\dagger [nc]_{s_-, \beta_-} - C_{nc(+)} [nc]_{s_+, \beta_+}^\dagger [nc]_{s_+, \beta_+}. \quad (7)$$

The notation $[] \dots$ represents the spin coupling through Clebsch-Gordan coefficients [66].

The nn spin singlet is given by

$$[nn]_{0,0} = \sum_\delta \left(\frac{1}{2} \delta \frac{1}{2} - \delta \middle| 00 \right) n_\delta n_{-\delta}, \quad (8)$$

† In the case of a spinless core, the nc interaction forms only one state with $s = 1/2$.

with $\delta = \pm 1/2$ denoting the spin projection of the neutrons. The nc pair in a spin- s state, with the projection β running from $-s$ to s , is represented by

$$[nc]_{s,\beta} = \sum_{\delta} \left(\frac{1}{2} \delta \zeta_{c\beta} - \delta \Big|_{s\beta} \right) n_{\delta} c_{\beta-\delta}. \quad (9)$$

All possible values of the repeated spin-projection indices in Eq. (7) are summed over through a scalar product. For example,

$$[nc]_{s,\beta}^{\dagger} [nc]_{s,\beta} = \sum_{\delta\delta'\beta} \left(\frac{1}{2} \delta \zeta_{c\beta} - \delta \Big|_{s\beta} \right) \left(\frac{1}{2} \delta' \zeta_{c\beta} - \delta' \Big|_{s\beta} \right) c_{\beta-\delta}^{\dagger} n_{\delta}^{\dagger} n_{\delta'} c_{\beta-\delta'}. \quad (10)$$

If a two-body system has a large scattering length, $a_0 \sim 1/M_{\text{halo}}$, and forms either a weakly bound state or a shallow virtual state, it becomes convenient to reformulate the two-body Lagrangian by introducing a dimer field. This was first discussed in Ref. [67], and has been extensively applied in the description of few nucleon systems, e.g., in Refs. [68, 69, 70, 71]. In this formalism, the nn part of the two-body Lagrangian in Eq. (7) is recast via the introduction of a nn spin-singlet dimer field d :

$$\mathcal{L}_{nn}^0 = d^{\dagger} \left[w_d \left(i\partial_0 + \frac{\nabla^2}{2M_d} \right) + \Delta_d \right] d - \frac{g_d}{\sqrt{2}} (d^{\dagger} [nn]_{0,0} + \text{h.c.}), \quad (11)$$

where Δ_d can be interpreted as the residual mass of the non-relativistic d field. $M_d \equiv 2m_n$ denotes the total masses of the nn system. w_d is a parameter that is chosen to be either 0 (for leading-order results) or -1 . The minus sign ensures that the effective range in the nn system is positive. If we drop the kinetic term of the dimer in Eq. (11) we may explicitly do the Gaussian integral over the dimer field in the path integral (i.e., perform a Hubbard-Stratonovich transformation) [70]. This shows that the Lagrangian (11) is equivalent to the one with the nn contact term in Eq. (7).

A one-neutron halo will only exist if one of the nc spin channels has a scattering length that is much larger than the range of the interaction. Therefore, we can introduce a nc spin- s auxiliary field (σ) to the Lagrangian in the corresponding *unnatural* channel, where the scattering length $a_0 \sim 1/M_{\text{halo}}$:

$$\mathcal{L}_{nc}^s = \sigma^{\dagger} \left[w_{\sigma} \left(i\partial_0 + \frac{\nabla^2}{2M_{\sigma}} \right) + \Delta_{\sigma} \right] \sigma - g_{\sigma} \left(\sigma_{s,\beta}^{\dagger} [nc]_{s,\beta} + \text{h.c.} \right). \quad (12)$$

Similarly to Eq. (11), Δ_{σ} is the residual mass of the σ field, $M_{\sigma} \equiv m_n + m_c$ is the total mass of the nc system, and $w_{\sigma} = \mp 1$ gives the appropriate sign to the nc effective range in the spin- s state. The two-body Lagrangian in a nc spin channel with a *natural* scattering length, $a_0 \sim 1/M_{\text{core}}$, retains its form in Eq. (7).

The three-body Lagrangian \mathcal{L}_3 does not contribute to a one-neutron halo nucleus but, in our EFT description of a two-neutron halo nucleus, arises from the requirement that the three-body problem be properly renormalized. For simplicity, we express \mathcal{L}_3 with the explicit inclusion of a dimer field. In the s-wave $2n$ halo system, whose ground state has spin ζ_c , \mathcal{L}_3 can be represented by the coupling between σ field with spin s and the n field with spin $1/2$, resulting in a scalar expression

$$\mathcal{L}_3 = -h \left([n\sigma]_{\zeta_c,a}^{\dagger} [n\sigma]_{\zeta_c,a} + \text{h.c.} \right), \quad (13)$$

where h is the three-body coupling constant.

Based on the Lagrangian density, we build formalisms for calculating observables in halo systems. The accuracy of the calculation can be progressively improved via the systematic expansion in $M_{\text{halo}}/M_{\text{core}}$. In the following we use a shorthand notation, denoting calculations done at leading, next-to-leading, and k th (for $k \geq 2$) order in this expansion as LO, NLO, and $N^k\text{LO}$.

2.2. Two-body amplitude

Here we derive the Feynman rules and calculate the corresponding two-body amplitude. The Feynman propagator of a free single-particle field S_y (with $y = n, c$) is written as a function of the four-dimensional momentum (p_0, \mathbf{p}) , which yields

$$iS_y(p_0, \mathbf{p}) = \frac{i}{p_0 - \mathbf{p}^2/2m_y + i\epsilon}. \quad (14)$$

For the two-body system in an unnaturally enhanced channel, the bare propagator of the dimer field d or σ is given by

$$iD_x^{(\text{bare})}(E, \mathbf{P}) = \frac{i}{w_x(E - \mathbf{P}^2/2M_x + i\epsilon) + \Delta_x}, \quad (15)$$

with $x = d, \sigma$ labeling the relevant dimer field. E and \mathbf{P} are, respectively, the energy and momentum of the dimer.

The dimer propagator is dressed by corrections from the s-wave pairwise interaction coupling the dimer propagator with two single particle fields. The dressed propagator D_x is obtained by an iterative sum of the one-loop self-energy to all orders. This summation corresponds to the Dyson equation shown in Fig. 3, whose solution yields

$$iD_x(E, \mathbf{P}) = \frac{i}{w_x(E - \mathbf{P}^2/2M_x + i\epsilon) + \Delta_x - \Sigma_x(E, \mathbf{P})}, \quad (16)$$

where $\Sigma_x(E, \mathbf{P})$ denotes the one-loop self-energy of the dimer field. Using dimensional regularization with power-law divergence subtraction (PDS) [72, 73, 74], Σ_x is calculated as

$$\begin{aligned} \Sigma_x(E, \mathbf{P}) &= -ig_x^2 \left(\frac{\Lambda}{2}\right)^{4-D} \int \frac{d^D q}{(2\pi)^D} iS_n(q_0, \mathbf{q}) iS_y(E - q_0, \mathbf{P} - \mathbf{q}) \\ &= \frac{\mu_x g_x^2}{2\pi} \left[\sqrt{2\mu_x \left(\frac{\mathbf{P}^2}{2M_x} - E - i\epsilon\right)} - \Lambda \right], \end{aligned} \quad (17)$$

where $y = n$ in the channel $x = d$, and $y = c$ in the channel $x = \sigma$. μ_x indicates the reduced mass in the two-body center-of-mass (C.M.) system. $\mu_d = m_n/2$ and $\mu_\sigma = Am_n/(A+1)$, where $A \equiv m_c/m_n$ denotes the core-neutron mass ratio. Λ in Eq. (17) represents a renormalization scale in the PDS scheme. This result is equivalent, in the large Λ limit, to a regularization scheme using a sharp ultraviolet momentum cutoff Λ in the integral at $D = 4$, where one only needs to replace Λ in the last line of Eq. (17) by $2\Lambda/\pi$ [74].

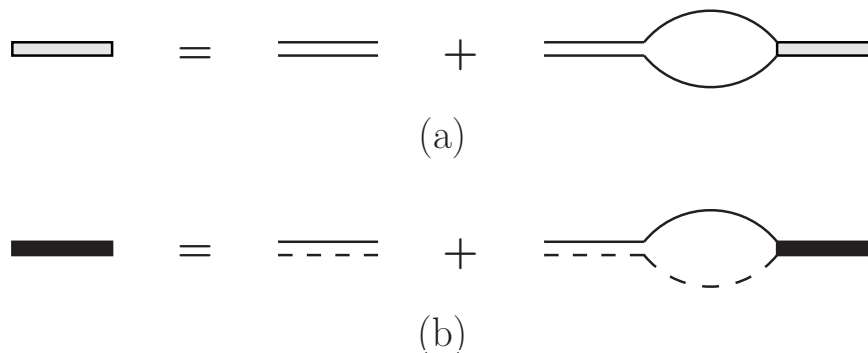


Figure 3. The Dyson equations for the dressed d (a) and σ (b) propagators. The dashed line indicates the field for the core, and the solid line is the neutron. The solid-solid and solid-dashed double lines are, respectively, the bare d and σ propagators. The grey and black rectangles are, respectively, the dressed d and σ propagators.

The dimer propagator in the C.M. frame can be matched to the two-body s-wave scattering amplitude in the channel $x = d, \sigma$ by

$$\langle \mathbf{k}' | t_{0,x}(E) | \mathbf{k} \rangle = g_x^2 D_x \left(\frac{k^2}{2\mu_x}, \mathbf{0} \right) = \frac{2\pi}{\mu_x} \left[\frac{1}{a_{0,x}} - \frac{r_{0,x}}{2} k^2 + ik \right]^{-1}, \quad (18)$$

where $|\mathbf{k}| = |\mathbf{k}'| = k = \sqrt{2\mu_x E}$ is the on-shell relative momentum in the C.M. frame. Eq. (18) matches the effective-range expansion (ERE) with terms of $\mathcal{O}(k^4)$ being omitted. For $k \sim M_{\text{halo}}$, this approximation is accurate at orders $(M_{\text{halo}}/M_{\text{core}})^2$. $a_{0,x}$ indicates the s-wave scattering length, which is related, in the unnaturally enhanced channel, to the low-momentum scale by $a_{0,x} \sim 1/M_{\text{halo}}$. $r_{0,x}$ denotes the s-wave effective range; it is associated with the breakdown scale, i.e., $r_{0,x} \sim 1/M_{\text{core}}$.

The renormalization conditions that yield Eq. (18) require tuning Δ_x and g_x in Eq. (16) to satisfy

$$a_{0,x} = \left(\frac{2\pi\Delta_x}{\mu_x g_x^2} + \Lambda \right)^{-1}; \quad (19a)$$

$$r_{0,x} = -w_x \frac{2\pi}{\mu_x^2 g_x^2}. \quad (19b)$$

This also indicates that the unitary term ik is invariant under regularization. In this way we obtain the renormalized dimer propagator

$$D_x(E, \mathbf{P}) = \frac{2\pi}{\mu_x g_x^2} \left[\frac{1}{a_{0,x}} - r_{0,x} \mu_x \left(E - \frac{\mathbf{P}^2}{2M_x} + i\epsilon \right) - \sqrt{2\mu_x \left(\frac{\mathbf{P}^2}{2M_x} - E - i\epsilon \right)} \right]^{-1}. \quad (20)$$

In the presence of an unnaturally large scattering length, the scattering amplitude $t_{0,x}$ can be expanded around the low-energy bound- or virtual-state pole at $k = i\gamma_{0,x}$, where $\gamma_{0,x}$ is the binding momentum of the two-body s-wave bound state ($\gamma_{0,x} > 0$) or virtual state ($\gamma_{0,x} < 0$). At the level of accuracy of Eq. (20) the binding momentum is related to the scattering length $a_{0,x}$ and the effective range $r_{0,x}$ by

$$\frac{1}{a_{0,x}} = \gamma_{0,x} - \frac{1}{2} r_{0,x} \gamma_{0,x}^2. \quad (21)$$

Therefore, physics of scale $k \sim |\gamma_{0,x}|$ is enhanced due to the pole structure of the scattering amplitude. The EFT is constructed based on a systematic expansion in $\gamma_{0,x}r_{0,x}$ or $r_{0,x}/a_{0,x}$. In the zero-range limit ($r_{0,x} = 0$ by taking $w_x = 0$ in Eq. (19b)) or the unitary limit ($a_{0,x} \rightarrow \pm\infty$), we have $\gamma_{0,x} = 1/a_{0,x}$: the leading order of the EFT expansion in Eq. (21) becomes exact.

Near the pole, the dimer propagator in the C.M. frame can be expanded about the pole at $-\gamma_{0,x}^2/(2\mu_x)$. Regardless of the value of $r_{0,x}$:

$$D_x(E, \mathbf{0}) = \frac{Z_x}{E + \gamma_{0,x}^2/(2\mu_x)} + \text{regular}, \quad (22)$$

with the residue of the pole obtained by

$$\frac{1}{Z_x} = \left. \frac{\partial D_x^{-1}(E, \mathbf{0})}{\partial E} \right|_{E=-\gamma_{0,x}^2/2\mu_x} = \frac{\mu_x^2 g_x^2}{2\pi\gamma_{0,x}} (1 - \gamma_{0,x}r_{0,x}). \quad (23)$$

Z_x is the x -field wave-function renormalization in the EFT.

In a bound one-neutron halo, Z_σ is connected to the asymptotic normalization coefficient (ANC) of the bound-state wave function. To see this we relate the interacting Green's function for this non-relativistic system to the two-body scattering amplitude $t(E)$ via

$$\frac{1}{E - H} = \frac{1}{E - H_0} + \frac{1}{E - H_0} t(E) \frac{1}{E - H_0}. \quad (24)$$

Any bound-state pole resides in the second piece on the right-hand side of Eq. (24). Just as we did for D_σ , we use the Laurent expansion for G to obtain the Green's function in the vicinity of the pole at $E = -\gamma_{0,\sigma}^2/(2\mu_\sigma)$. In the s-wave case, we insert into Eq. (24) the expression for $\langle \mathbf{k}' | t_{0,\sigma}(E) | \mathbf{k} \rangle$ from Eq. (18) and keep only the pole part to obtain:

$$\langle \mathbf{k}' | \frac{1}{E - H} | \mathbf{k} \rangle = \frac{\psi_0(\mathbf{k}') \psi_0^*(\mathbf{k})}{E + \gamma_{0,\sigma}^2/(2\mu_\sigma)} + \text{regular}, \quad (25)$$

where $\psi_0(\mathbf{k})$ is the asymptotic wave function for an s-wave neutron-core bound state, whose co-ordinate space representation is

$$\psi_0(\mathbf{r}) = C_\sigma Y_{00}(\hat{r}) \frac{\exp(-\gamma_{0,\sigma} r)}{r}, \quad (26)$$

with C_σ the ANC in the neutron-core s-wave bound state. Matching Eq. (25) to Eq. (22) shows that C_σ is related to Z_σ via

$$C_\sigma = \frac{\mu_\sigma g_\sigma}{\sqrt{\pi}} \sqrt{Z_\sigma} = \sqrt{\frac{2\gamma_{0,\sigma}}{1 - \gamma_{0,\sigma} r_{0,\sigma}}}. \quad (27)$$

Therefore, one can use the ANC C_σ and the binding momentum $\gamma_{0,\sigma}$ to determine the EFT parameters g_σ and Δ_σ , instead of fixing them from the scattering parameters $a_{0,\sigma}$ and $r_{0,\sigma}$. At LO, $C_{\sigma,LO} = \sqrt{2\gamma_{0,\sigma}}$ is determined by the binding momentum. At NLO, the effect of a finite effective range enters and produces an ANC ratio different from one:

$$C_\sigma/C_{\sigma,LO} = 1/\sqrt{1 - \gamma_{0,\sigma} r_{0,\sigma}}. \quad (28)$$

Note that $C_\sigma/C_{\sigma,LO} > 1$ if $\gamma_{0,\sigma} > 0$ (i.e. the one-neutron halo is bound) and $r_{0,\sigma} > 0$. The extent to which this ratio deviates from one then indicates the short range of the neutron-core potential, compared to the extent of the bound state. Marked enhancement of the asymptotic wave function over the LO prediction correlates with a strong neutron-core potential that pushes the tail of the wave function up.

Although C_σ is not an observable that is directly measured in neutron-core scattering experiments, it can be extracted from such data by an analytic continuation of the scattering amplitude to negative energies. There t_σ has the pole structure

$$\langle \mathbf{k}' | t_\sigma(E) | \mathbf{k} \rangle = \frac{2\pi C_\sigma^2 / C_{\sigma,LO}^2}{\mu_\sigma \gamma_{0,\sigma} + ik} + \text{regular}. \quad (29)$$

As compared to the ERE, which is an expansion in powers of $r_{0,\sigma}/a_{0,\sigma}$ around $k = 0$, this parameterization in terms of an ANC, dubbed the “ z -parameterization” in Ref. [75], is a more convenient choice for bound-state calculations. Using this parameterization, the pole at $k = i\gamma_{0,\sigma}$ is exactly reproduced at each order, and the residue of the scattering amplitude, $C_\sigma^2/C_{\sigma,LO}^2$, is expanded into a LO piece = 1 and an NLO piece = $(C_\sigma^2/C_{\sigma,LO}^2 - 1)$. N²LO and higher corrections to the ANC are then zero by definition. The z -parameterization of the scattering amplitude is accurate at relative orders $(M_{\text{halo}}/M_{\text{core}})^2$, beyond which a new ERE parameter at $\mathcal{O}(k^4)$ enters.

Here we illustrate the utility of the z -parameterization in the calculation of the matter form factor of one-neutron halos. The neutron-core form factor is the Fourier transform of the coordinate-space probability density distribution:

$$F_{nc}(|\mathbf{q}|) = \int d^3r |\psi_\sigma(\mathbf{r})|^2 \exp(i\mathbf{q} \cdot \mathbf{r}). \quad (30)$$

At LO, we use the zero-range two-body wave function by inserting $C_{\sigma,LO} = \sqrt{2\gamma_{0,\sigma}}$ in Eq. (26) and obtain

$$F_{nc}^{(0)}(|\mathbf{q}|) = \frac{2\gamma_{0,\sigma}}{|\mathbf{q}|} \arctan\left(\frac{|\mathbf{q}|}{2\gamma_{0,\sigma}}\right). \quad (31)$$

The NLO F_{nc} is calculated from Eq. (30) using the full C_σ , with an additional insertion of a constant piece that ensures the matter form factor is properly normalized [75, 76], i.e., $F_{nc}(0) = 1$. Therefore the NLO correction to F_{nc} is [75]

$$F_{nc}^{(1)}(|\mathbf{q}|) = -(C_\sigma^2/C_{\sigma,LO}^2 - 1) \left[1 - \frac{2\gamma_{0,\sigma}}{|\mathbf{q}|} \arctan\left(\frac{|\mathbf{q}|}{2\gamma_{0,\sigma}}\right) \right]. \quad (32)$$

Since the low-momentum expansion of the form factor in the one-neutron halo is related to the mean squared distance between the neutron and the core $\langle r_{nc}^2 \rangle$ via

$$F_{nc}(|\mathbf{q}|) = 1 - \frac{1}{6} \langle r_{nc}^2 \rangle \mathbf{q}^2 + \mathcal{O}(\mathbf{q}^4), \quad (33)$$

we obtain $\langle r_{nc}^2 \rangle$ by calculating the first-order derivative of F_{nc} with respect to q^2 at zero. $\langle r_{nc}^2 \rangle^{1/2}$ at NLO is then

$$\langle r_{nc}^2 \rangle^{1/2} = \frac{C_\sigma / C_{\sigma,LO}}{\sqrt{2\gamma_{0,\sigma}}}. \quad (34)$$

With the neutron-core radius in hand we can calculate the matter radius, which is defined, in the point-nucleon limit, as the average distance-squared from all nucleons in a halo nucleus to the center of mass [77]:

$$\langle r_m^2 \rangle_{1n\text{-halo}} = \frac{A}{(A+1)} \langle r_m^2 \rangle_{\text{core}} + \frac{A}{(A+1)^2} \langle r_{nc}^2 \rangle, \quad (35)$$

where the first term is the correction from the matter radius of the core.

A more rigorous method of keeping the form factor normalized to $F_{nc}(0) = 1$ involves imposing gauge invariance of the Lagrangian in the presence of an external gauge field. We defer detailed discussion of this approach to Sec. 4 when we consider the coupling of electromagnetic fields to the halo system.

2.3. Applications: one-neutron s-wave halos

Here we demonstrate several examples of one-neutron s-wave halos, whose properties measured in experiments or predicted by Halo EFT are listed in Table 1.

The deuteron has a spin-triplet ground state ($J^P = 1^+$), which is dominated by an s-wave component. The deuteron binding energy as determined by the 2012 Atomic Mass Evaluation (AME2012) [78, 79] is $S_{1n} = 2.224573(2)$ MeV. (Here we use $S_{1n} \equiv \text{sgn}(\gamma_{0,\sigma})\gamma_{0,\sigma}^2/(2\mu_\sigma)$ to denote the neutron-core separation energy in a one-neutron halo, with $S_{1n} > 0$ (< 0) corresponding to a bound (virtual) s-wave state.) In the language of Halo EFT, the low scale here is $M_{\text{halo}} \sim \gamma_{0,\sigma} = \sqrt{m_n S_{1n}} = 45.7$ MeV. A naive estimation of the high scale is set by the excitation of the nucleon into the $\Delta(1232)$ isobar resonance, i.e., $M_{\text{core}} \sim m_\Delta - m_n \approx 293$ MeV. However, the nucleon-nucleon interaction has a range that is set by the exchange of pions among nucleons; it brings the high scale down to $M_{\text{core}} \approx 140$ MeV: the pion mass is lower than the $m_\Delta - m_n$ scale [96]. But, for physics at scales well below the pion mass, nuclear potentials can still be considered as short ranged by integrating out the pion degrees of freedom. The pionless EFT calculation of the deuteron is then based on the expansion parameter $M_{\text{halo}}/M_{\text{core}} \approx 1/3$.

The low energy physics of the deuteron can also be related to np scattering data. In the s-wave spin-triplet channel, the scattering parameters $a_{0,\sigma} = 5.4112(15)$ fm and $r_{0,\sigma} = 1.7436(19)$ fm are determined from an analysis of np elastic scattering data [90]. Their values indicate that the effective range is of natural size ($r_{0,\sigma} \sim 1/M_{\text{core}}$) while the scattering length is unnaturally large, i.e., $a_{0,\sigma} \sim 1/M_{\text{halo}}$. An EFT expansion based on $r_{0,\sigma}/a_{0,\sigma}$ is highly consistent with the $1/3$ estimated above. Using Eq. (27) we obtain the ANC for the deuteron s-wave wave function [75] to be $C_\sigma = 1.295$. The deuteron structure radius in the point-nucleon limit, equivalent to $0.5\langle r_{np}^2 \rangle^{1/2}$, is thus calculated from Eq. (34) to be 1.977 fm, which overlaps with the value extracted from elastic electron-deuteron scattering [83] and agrees with calculations based on realistic nucleon-nucleon potentials [97].

Another example of a one-neutron halo is ^{19}C , whose ground state was determined from the Coulomb dissociation spectrum [63] to be $J^P = 1/2^+$, with a separation energy

	${}^2\text{H}$	${}^{11}\text{Be}$	${}^{15}\text{C}$	${}^{19}\text{C}$
Experiment				
J^P	1^+	$1/2^+$	$1/2^+$	$1/2^+$
S_{1n} [MeV]	2.224573(2)	0.50164(25)	1.2181(8)	0.58(9)
E_c^* [MeV]	293	3.36803(3)	6.0938(2)	1.62(2)
$\langle r_{nc}^2 \rangle^{1/2}$ [fm]	3.936(12) ¹	6.05(23) ³	4.15(50) ⁶	6.6(5) ⁶
	3.95014(156) ²	5.7(4) ⁴	7.2 \pm 4.0 ⁷	6.8(7) ⁸
		5.77(16) ⁵	4.5(5) ⁸	5.8(3) ⁹
EFT				
$M_{\text{halo}}/M_{\text{core}}$	0.33	0.39	0.45	0.6
$r_{0,\sigma}/a_{0,\sigma}$	0.32	0.38	0.43	0.33
$C_\sigma/C_{\sigma,LO}$	1.295	1.44 ¹¹	1.63 ¹²	1.3
$r_{0,\sigma}$ [fm]	1.7436(19) ¹⁰	3.5 ¹¹	2.67 ¹²	2.6 ¹³
$\langle r_{nc}^2 \rangle_{\text{theo}}^{1/2}$ [fm]	3.954	6.85	4.93	5.72

Table 1. Properties of one-neutron halos. S_{1n} is the one-neutron separation energy from AME2012 [78, 79]. The first core excitation energies E_c^* for $A > 1$ halos are taken from the TUNL database [80, 81, 82]. M_{halo} and M_{core} are estimated using S_{1n} and E_c^* , except for the deuteron, where we take $M_{\text{core}} = 140$ MeV.

- 1 From the structure radius deduced from electron-deuteron scattering [83] ($\times 2$).
- 2 From the structure radius determined by isotope shift spectroscopy [84] ($\times 2$).
- 3 Extracted by Ref. [77] using matter radii [85] determined from σ_I .
- 4 From GSI Coulomb dissociation data [86]
- 5 From RIKEN Coulomb dissociation data [87]
- 6 Extracted by Ref. [88] using reanalyzed matter radii from σ_I data in [89].
- 7 Extracted by Ref. [88] using charge radii determined from σ_{cc} data in [88].
- 8 From the halo radius obtained in Ref. [88] by fitting both σ_I and σ_{cc} ($\times (A+1)/A$).
- 9 From the halo radius obtained in RIKEN Coulomb dissociation data [63] ($\times (A+1)/A$).
- 10 From an analysis of np scattering data [90].
- 11 Value of $C_\sigma/C_\sigma^{\text{LO}}$ (or $r_{0,\sigma}$) obtained in an *ab initio* calculation [91].
- 12 Using EFT [92] to fit $C_\sigma/C_\sigma^{\text{LO}}$ (or $r_{0,\sigma}$) to the neutron capture data [93].
- 13 Using EFT [94] to fit $r_{0,\sigma}$ to the E1 data [63, 95].

$S_{1n} = 0.53(13)$ MeV between the ${}^{18}\text{C}$ core ($J^P = 0^+$) and the last neutron. This result is consistent with $S_{1n} = 0.65(15)$ MeV from one-neutron knock out reactions [98], and $S_{1n} = 0.58(9)$ MeV in AME2012 [78, 79]. The first excitation energy of ${}^{18}\text{C}$ is $E_c^* = 1.62(2)$ MeV [80]. These values suggest a separation of low and high scales by $M_{\text{halo}}/M_{\text{core}} \sim \sqrt{S_{1n}/E_c^*} \approx 0.6$. Ref. [94] performed an EFT analysis on the ${}^{19}\text{C}$ Coulomb dissociation data [63, 95], where the theoretical constraints on S_{1n} and the ANC were determined from those data. We will describe how the ANC is determined from Coulomb dissociation or radiative capture processes using EFT analysis in Sec. 4. Ref. [94] extracted $C_\sigma/C_{\sigma,LO} = 1.31$, together with $S_{1n} = 0.575(55)(20)$ MeV—the latter in agreement with the extraction in Ref. [63] and the evaluation of Refs. [78, 79]. These correspond to ERE parameters $a_{0,\sigma} = 7.75(35)(30)$ fm and $r_{0,\sigma} = 2.6_{-0.9}^{+0.6} \pm 0.1$

fm. The ratio $r_{0,\sigma}/a_{0,\sigma} = 0.33$ suggests that the EFT converges faster than the naive dimensional estimate, $M_{\text{halo}}/M_{\text{core}} \approx 0.6$. For all of these ^{19}C observables the first and second errors come from, respectively, the 1σ statistical uncertainty of the data fitting and the N³LO systematic uncertainties of the EFT, which are estimated to be of relative size $(r_{0,\sigma}/a_{0,\sigma})^3$.

The above ^{19}C results imply an s-wave binding momentum $\gamma_{0,\sigma} = 32.0$ MeV in ^{19}C . This, together with the extracted ANC, yields the neutron-core distance from Eq. (34) to be $\langle r_{nc}^2 \rangle^{1/2} = 5.72$ fm, which agrees with values deduced by the E1 sum rule of Coulomb dissociation [63] and extracted from charge-changing cross section [88] measurements (see Table 1).

Other examples of one-neutron halos are ^{11}Be and ^{15}C . Their ground states both have spin-parity quantum numbers $J^P = 1/2^+$, with one valence neutron attached to the ^{10}Be and ^{14}C cores ($J^P = 0^+$). The one-neutron separation energies S_{1n} of ^{11}Be and ^{15}C are determined in the atomic mass evaluation [78, 79]; while the first excitation energies of the cores E_c^* are obtained from the nuclear data evaluation [81, 82] (see Table 1).

Based on naive dimensional analysis the EFT expansion parameter in ^{11}Be is $M_{\text{halo}}/M_{\text{core}} \sim \sqrt{S_{1n}/E_c^*} = 0.39$. The ANC in the ^{11}Be ground state was recently obtained in an *ab initio* calculation that used the No-Core Shell Model with Continuum approach (described further in Sec. 6) as $C_\sigma/C_{\sigma,LO} = 1.44$ [91]. This corresponds to $r_{0,\sigma} = 3.5$ fm, which yields $r_0/a_0 = 0.38$ in ^{11}Be , in agreement with the expansion parameter inferred from $M_{\text{halo}}/M_{\text{core}}$. ^{11}Be will be discussed further in Sec. 3.6, after we have developed the formalism to describe the p-waves that play a prominent role there.

EFT calculations for ^{15}C were performed in Refs. [92, 99]. By fitting the Halo EFT neutron capture cross section to experiment [93], Rupak, Fernando, and Vaghani determined the ANC ratio $C_\sigma/C_{\sigma,LO} = 1.63$, or equivalently, an effective range $r_{0,\sigma} = 2.67$ fm. Their calculation suggested an unnatural scale for the effective range, with $r_{0,\sigma} \sim 1/M_{\text{halo}}$ [92], implying that the z-parameterization, $C_\sigma^2/C_{\sigma,LO}^2 - 1$, becomes non-perturbative in this system. However, this conclusion may be associated with the specific choice of power counting in the n - ^{14}C p-wave channel used in Ref. [92], as we will explain in further detail in Sec. 3. If we adopt the ANC extracted in Ref. [92] we obtain $r_0/a_0 = 0.43$, which, while it is a somewhat large effective range, is still consistent with $M_{\text{halo}}/M_{\text{core}} \approx 0.45$.

2.4. Applications: unbound s-wave neutron-core systems

Halo-like features also exist in unbound neutron-core systems, if such systems display a large negative scattering length. In the np spin singlet state, the parameters $a_{0,d}^{(np)} = -23.7148(43)$ fm and $r_{0,d}^{(np)} = 2.750(18)$ fm are determined from an analysis of low-energy np elastic-scattering data [90]. The nn singlet state is also thought to be unbound, with a scattering length $a_{0,d}^{(nn)} = -18.6(5)$ fm obtained from the neutron time-of-flight spectrum in the reaction $\pi^-d \rightarrow \gamma nn$ [100]. The similar, large values of

the spin-singlet scattering length for np and nn pairs suggest that isospin is a good approximate symmetry for nuclear forces. Isospin symmetry and the $r_{0,d}/a_{0,d}$ expansion mean that pionless EFT can predict universal features shared by the np and nn singlet states.

It was argued in Ref. [101] that the pion-deuteron capture experiment [100] only determines the magnitude of $a_{0,d}^{(nn)}$ but is insensitive to its sign, which raises the possibility that a weakly bound dineutron state exists. Using pionless EFT at NLO, Ref. [101] analyzed the constraint on the value of $a_{0,d}^{(nn)}$ from the ${}^3\text{H}$ - ${}^3\text{He}$ binding energy difference and the neutron-deuteron s-wave doublet scattering phase shifts. (See Ref. [102] for an earlier, LO, treatment.) Hammer and König concluded that a bound dineutron cannot be excluded by an NLO pionless EFT analysis of these data. In fact, in the EFT changing the scattering length from a large positive value to a large negative value, referred to as the unitary crossing, requires only slight variation of Δ_d in Eq. (19a) around the pole in $a_{0,d}$. The continuity of Δ_d at the unitary limit indicates that isospin symmetry can still be a good approximation even if $a_{0,d}^{(nn)}$ and $a_{0,d}^{(np)}$ have opposite signs. This argument is consistent with the finding of Ref. [101]: that the ${}^3\text{H}$ - ${}^3\text{He}$ binding energy difference is a continuous function of $1/a_{0,d}^{(nn)}$ around $1/a_{0,d}^{(nn)} = 0$. The unitary crossing is also an important idea in atomic physics, where it is referred to as the BCS-BEC crossover, and generates important many-body phenomena. The unitary crossing will play an important role in our later discussion of three-body problems in halo nuclei, see Sec. 2.6.

${}^{11}\text{Li}$, whose ground state has spin-parity $J^P = 3/2^-$ was one of the first halo nuclei [103] beyond the few-nucleon systems to be discovered. ${}^{11}\text{Li}$ is a Borromean two-neutron halo, where the neutron-core is unbound. Here we focus on the separation of scales in ${}^{10}\text{Li}$ and refer to later sections for properties of ${}^{11}\text{Li}$. The ground state of the ${}^9\text{Li}$ core has $J^P = 3/2^-$ and a first excitation energy $E_c^* = 2.691(5)$ MeV [81], which sets the M_{core} scale. The M_{halo} scale is associated with the ${}^{10}\text{Li}$ ground state, which is an unbound s-wave neutron-core virtual state ($J^P = 1^-$ or 2^-) with $S_{1n} = -25(15)$ keV [81]. The EFT expansion parameter for ${}^{10}\text{Li}$ is estimated as $M_{\text{halo}}/M_{\text{core}} \sim \sqrt{|S_{1n}|/E_c^*} \approx 10\%$. A proton removal reaction experiment [104] observed two resonance states of ${}^{10}\text{Li}$ at energies $E_{2,1+} = 110(40)$ keV and $E_{2,2+} = 500(100)$ keV above the neutron-core threshold. These are expected to be p-wave states. As such they enter at higher orders in the EFT compared to the s-wave virtual state, whose unnaturally large scattering length promotes it to LO.

${}^{21}\text{C}$ is another unbound neutron-core system [105]. The ratio between the one-neutron separation energies of ${}^{21}\text{C}$ [78, 79] and ${}^{20}\text{C}$ [80] provides a valid expansion parameter in EFT. The neighboring isotope ${}^{22}\text{C}$ has recently been identified as a weakly-bound two-neutron halo and is the dripline nucleus of carbon isotopes. A Glauber-model analysis of the reaction cross section of ${}^{22}\text{C}$ on a hydrogen target [106] suggests that $n-{}^{20}\text{C}$ is preferentially in $1/2^+$ configuration. This finding is supported by the measurement of the two-neutron removal reaction on the ${}^{22}\text{C}$ target [107]. The two-neutron halo structure of ${}^{22}\text{C}$ implies that ${}^{21}\text{C}$ occupies an s-wave virtual state near the

unitary limit. However, a recent study of the $n-^{21}\text{C}$ decay spectrum via one-proton removal from the ^{22}N beam [108] implies that the $n-^{20}\text{C}$ scattering length is limited to $|a_{0,\sigma}| < 2.8$ fm (or equivalently $S_{1n} < -2.8$ MeV): much smaller than expected in an unnaturally enhanced channel. Therefore, further studies on the properties of ^{21}C are needed.

2.5. The three-body amplitude

Here we describe two-neutron halos as a neutron-neutron-core three-body system. We use the Jacobi momentum plane-wave state $|\mathbf{p}, \mathbf{q}\rangle_i$ to represent the kinematics of the three-body system in the C.M. frame. The index i indicates that these momenta are defined in the two-body fragmentation channel (i, jk) , in which particle i is the spectator and (jk) the interacting pair. Based on this definition, \mathbf{p} represents the relative momentum in the pair (jk) ; while \mathbf{q} denotes the relative momentum between the spectator i and the (jk) pair. The plane-wave states are normalized as [109]:

$${}_i\langle \mathbf{p}\mathbf{q} | \mathbf{p}'\mathbf{q}' \rangle_i = (2\pi)^6 \delta^{(3)}(\mathbf{p} - \mathbf{p}') \delta^{(3)}(\mathbf{q} - \mathbf{q}'). \quad (36)$$

The Jacobi momenta are related to the momenta in the direct product of three single-particle states $|\mathbf{k}_1, \mathbf{k}_2, \mathbf{k}_3\rangle$ in the C.M. frame (i.e., $\mathbf{k}_1 + \mathbf{k}_2 + \mathbf{k}_3 = 0$) by

$$\langle \mathbf{k}_1, \mathbf{k}_2, \mathbf{k}_3 | \mathbf{p}\mathbf{q} \rangle_i = (2\pi)^6 \delta^{(3)} \left(\mathbf{p}_i - \mu_{jk} \left[\frac{\mathbf{k}_j}{m_j} - \frac{\mathbf{k}_k}{m_k} \right] \right) \delta^{(3)} \left(\mathbf{q}_i - \mu_{i(jk)} \left[\frac{\mathbf{k}_i}{m_i} - \frac{\mathbf{k}_j + \mathbf{k}_k}{M_{jk}} \right] \right), \quad (37)$$

where $M_{jk} = m_j + m_k$, $\mu_{jk} = m_j m_k / M_{jk}$, and $\mu_{i(jk)} = m_i M_{jk} / (m_i + M_{jk})$. From Eqs. (36) and (37), the projection between different partitions must obey

$${}_n\langle \mathbf{p}\mathbf{q} | \mathbf{p}'\mathbf{q}' \rangle_c = (2\pi)^6 \delta^{(3)}(\mathbf{p} + \boldsymbol{\pi}_1(\mathbf{q}', \mathbf{q})) \delta^{(3)}(\mathbf{p}' - \boldsymbol{\pi}_2(\mathbf{q}, \mathbf{q}')), \quad (38a)$$

$${}_n\langle \mathbf{p}\mathbf{q} | \mathcal{P} | \mathbf{p}'\mathbf{q}' \rangle_n = (2\pi)^6 \delta^{(3)}(\mathbf{p} - \boldsymbol{\pi}_3(\mathbf{q}', \mathbf{q})) \delta^{(3)}(\mathbf{p}' + \boldsymbol{\pi}_3(\mathbf{q}, \mathbf{q}')), \quad (38b)$$

where \mathcal{P} denotes the permutation between the two valence neutrons. The momenta $\boldsymbol{\pi}_1$, $\boldsymbol{\pi}_2$ and $\boldsymbol{\pi}_3$ are defined as

$$\boldsymbol{\pi}_1(\mathbf{q}, \mathbf{q}') = \mathbf{q} + A\mathbf{q}' / (A + 1), \quad (39a)$$

$$\boldsymbol{\pi}_2(\mathbf{q}, \mathbf{q}') = \mathbf{q} + \mathbf{q}' / 2, \quad (39b)$$

$$\boldsymbol{\pi}_3(\mathbf{q}, \mathbf{q}') = \mathbf{q} + \mathbf{q}' / (A + 1). \quad (39c)$$

To discuss the spin and parity of a halo nucleus, we introduce the partial-wave-decomposed representation. The relative orbital angular momentum and the spin of the pair (jk) are defined as l_i and s_i . They are coupled to form the total angular momentum j_i in the pair. We also define the spin of the spectator i as ς_i , the relative orbital angular momentum between the spectator i and the pair (jk) as λ_i , and the corresponding total angular momentum as I_i . The overall orbital angular momentum, spin and total angular momentum of the three-body system are denoted by L_i , S_i and J . We then have:

$$\mathbf{L}_i = \mathbf{l}_i + \boldsymbol{\lambda}_i, \quad (40a)$$

$$\mathbf{S}_i = \mathbf{s}_i + \boldsymbol{\varsigma}_i, \quad (40b)$$

$$\mathbf{J} = \mathbf{L}_i + \mathbf{S}_i = \mathbf{j}_i + \mathbf{I}_i. \quad (40c)$$

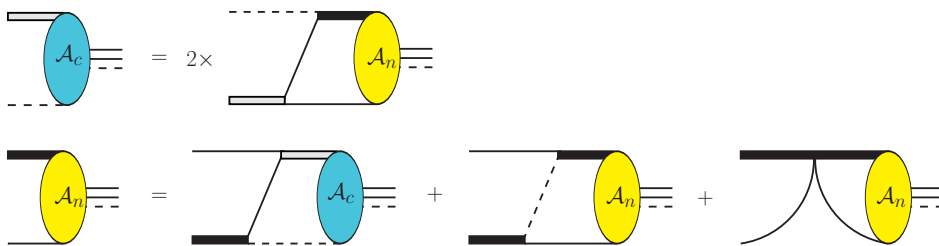


Figure 4. The transition amplitudes \mathcal{A}_c and \mathcal{A}_n in coupled integral equations. The last piece represents the contribution from the nnn three-body force.

Knowing the spin and orbital-angular-momentum quantum numbers, we can construct an eigenstate of a three-body system with respect to the spin and orbital-angular-momentum operators. Note that J for a given three-body eigenstate is a conserved quantum number, which is independent of the choice of partition representations given in Eq. (40c). We decompose the Jacobi momenta with respect to these spin and orbital- and total-angular-momentum quantum numbers by [109]

$$|p, q; \Omega_i\rangle_i = \sum_{L_i S_i} \sqrt{\widehat{j}_i \widehat{I}_i \widehat{L}_i \widehat{S}_i} \begin{Bmatrix} l_i & s_i & j_i \\ \lambda_i & \varsigma_i & I_i \\ L_i & S_i & J \end{Bmatrix} |p, q; (l_i, \lambda_i) L_i; (s_i, \varsigma_i) S_i; (L_i S_i) J\rangle_i, \quad (41)$$

where \widehat{j}_i denotes $2j_i + 1$ (the same holds for \widehat{I}_i , \widehat{L}_i and \widehat{S}_i), $p \equiv |\mathbf{p}|$, and $q \equiv |\mathbf{q}|$. The collective symbol Ω_i represents all conserved spin, orbital- and total-angular-momentum quantum numbers in the partition (i, jk) .

In this section we focus on s-wave two-neutron halos, where $l_i = \lambda_i = L_i = 0$ and the values of the total angular momenta are equal to their corresponding spins. Therefore, one can solely use spins to represent the decomposed plane-wave state in s-wave $2n$ halos as $|p, q; (s_i, \varsigma_i) S\rangle_i$, where the three-body total spin S is the same in different partitions. In the (c, nn) partition, $S = \varsigma_c$ since the two-neutron pair is spin singlet ($s_c = 0$). Therefore, in the (n, nc) partition, the neutron-core pair with spin $s_n = |\varsigma_c \pm 1/2|$ couples with the second neutron with spin $\varsigma_n = 1/2$ to form the three-body total spin $S = \varsigma_c$.

Here we assume that the neutron-core states with $s_n = |\varsigma_c \pm 1/2|$ are degenerate and have equal scattering lengths. Under this assumption, the three-body formalism in s-wave halos with a spin-zero core becomes general for an arbitrary s-wave two-neutron halo with spin ς_c . Just as in the Faddeev formalism [110, 109, 111], the three-body wave function is decomposed into components corresponding to different partitions. In the EFT, $2n$ -halo nuclei are described by the transition amplitudes, \mathcal{A}_c and \mathcal{A}_n , connecting the spectator and the interacting pair to the three-body bound state. \mathcal{A}_c and \mathcal{A}_n are represented by functions of the Jacobi momentum \mathbf{q} between the spectator and the pair, and are the solution of coupled-channel homogeneous integral equations [112, 113] which are illustrated with Feynman diagrams in Fig. 4.

At leading order, one can take $r_{0,x} \rightarrow 0$ for $x = d, \sigma$ and rewrite the dimer

propagator D_x as

$$D_x^{(0)}(E, \mathbf{P}) = -\frac{2\pi}{\mu_x g_x^2 - \gamma_{0,x} + \sqrt{2\mu_x (\mathbf{P}^2/2M_x - E - i\epsilon)}}. \quad (42)$$

Therefore, the integral equations for LO \mathcal{A}_n and \mathcal{A}_c are constructed to be

$$\begin{aligned} i\mathcal{A}_c(B_3, \mathbf{q}) &= \int \frac{d^4q'}{(2\pi)^4} iS_n(q'_0, \mathbf{q}') \left[-\sqrt{2}g_d g_\sigma iS_n(-B_3 - q'_0 - \frac{\mathbf{q}^2}{2m_c}, -\mathbf{q} - \mathbf{q}') \right] \\ &\quad \times iD_\sigma^{(0)}(-B_3 - q'_0, -\mathbf{q}') i\mathcal{A}_n(B_3, \mathbf{q}') \end{aligned} \quad (43a)$$

$$\begin{aligned} i\mathcal{A}_n(B_3, \mathbf{q}) &= \int \frac{d^4q'}{(2\pi)^4} iS_c(q'_0, \mathbf{q}') \left[-\sqrt{2}g_d g_\sigma iS_n(-B_3 - q'_0 - \frac{\mathbf{q}^2}{2m_n}, -\mathbf{q} - \mathbf{q}') \right] \\ &\quad \times iD_d^{(0)}(-B_3 - q'_0, -\mathbf{q}') i\mathcal{A}_c(B_3, \mathbf{q}') \\ &\quad + \int \frac{d^4q'}{(2\pi)^4} iS_n(q'_0, \mathbf{q}') \left[-g_\sigma^2 iS_c(-B_3 - q'_0 - \frac{\mathbf{q}^2}{2m_n}, -\mathbf{q} - \mathbf{q}') - ih \right] \\ &\quad \times iD_\sigma^{(0)}(-B_3 - q'_0, -\mathbf{q}') i\mathcal{A}_n(B_3, \mathbf{q}'). \end{aligned} \quad (43b)$$

We then rescale the amplitudes to $\tilde{\mathcal{A}}_c(\mathbf{q}) \equiv \sqrt{2}g_d^{-1}\mathcal{A}_c(B_3, \mathbf{q})$ and $\tilde{\mathcal{A}}_n(\mathbf{q}) \equiv g_\sigma^{-1}\mathcal{A}_n(B_3, \mathbf{q})$ to absorb the explicit dependence on the two-body coupling constants. After integrating out the time component of the loop momentum, we obtain

$$\tilde{\mathcal{A}}_c(\mathbf{q}) = 2 \int \frac{d^3q}{4\pi^2} G_0^c(\pi_2(\mathbf{q}', \mathbf{q}), q; B_3) \tau_\sigma(q'; B_3) \tilde{\mathcal{A}}_n(\mathbf{q}') \quad (44a)$$

$$\begin{aligned} \tilde{\mathcal{A}}_n(\mathbf{q}) &= \int \frac{d^3q'}{4\pi^2} G_0^c(\pi_2(\mathbf{q}, \mathbf{q}'), q'; B_3) \tau_d(q'; B_3) \tilde{\mathcal{A}}_c(\mathbf{q}') \\ &\quad + \int \frac{d^3q'}{4\pi^2} \left[G_0^n(\pi_3(\mathbf{q}', \mathbf{q}), q; B_3) + \frac{H(\Lambda)}{\Lambda^2} \right] \tau_\sigma(q'; B_3) \tilde{\mathcal{A}}_n(\mathbf{q}'), \end{aligned} \quad (44b)$$

where G_0^n and G_0^c are the three-body Green's functions expressed in two different partitions:

$$G_0^n(p, q; B_3) = \left(m_n B_3 + \frac{A+1}{2A} p^2 + \frac{A+2}{2(A+1)} q^2 \right)^{-1}, \quad (45a)$$

$$G_0^c(p, q; B_3) = \left(m_n B_3 + p^2 + \frac{A+2}{4A} q^2 \right)^{-1}. \quad (45b)$$

The dimer propagators, embedded in the three-body integral equations (44a) and (44b), are rescaled via $\tau_x(q; B_3) \equiv -(m_n g_x^2/2\pi) D_x^{(0)}$ for $x = d, \sigma$, which yields

$$\tau_d(q; B_3) = \frac{2}{-\gamma_{0,d} + \sqrt{m_n B_3 + \frac{A+2}{4A} q^2}}, \quad (46a)$$

$$\tau_\sigma(q; B_3) = \frac{(A+1)/A}{-\gamma_{0,\sigma} + \sqrt{\frac{A}{A+1} (2m_n B_3 + \frac{A+2}{A+1} q^2)}}. \quad (46b)$$

In Eq. (44b), $H(\Lambda) \equiv -\Lambda^2 h/(m_n g_\sigma^2)$ is the dimensionless three-body force parameter.

By projecting the three-body transition amplitudes to s-waves, we simplify the integral equations to the expressions given in Refs. [112, 113]

$$\tilde{\mathcal{A}}_c(q) = \frac{2}{\pi} \int_0^\Lambda dq' q'^2 X_{00}^n(q', q; B_3) \tau_\sigma(q'; B_3) \tilde{\mathcal{A}}_n(q') \quad (47a)$$

$$\begin{aligned}\tilde{\mathcal{A}}_n(q) &= \frac{1}{\pi} \int_0^\Lambda dq' q'^2 X_{00}^n(q, q'; B_3) \tau_d(q'; B_3) \tilde{\mathcal{A}}_c(q') \\ &\quad + \frac{1}{\pi} \int_0^\Lambda dq' q'^2 \left[X_{00}^c(q', q; B_3) + \frac{H(\Lambda)}{\Lambda^2} \right] \tau_\sigma(q'; B_3) \tilde{\mathcal{A}}_n(q')\end{aligned}\quad (47b)$$

where the kernel functions are

$$X_{00}^n(q, q'; B_3) = \frac{1}{2} \int_{-1}^1 d(\hat{\mathbf{q}} \cdot \hat{\mathbf{q}}') G_0^c(\pi_2(\mathbf{q}, \mathbf{q}'), q'; B_3) = -\frac{1}{qq'} Q_0(z_{nc}), \quad (48a)$$

$$X_{00}^c(q, q'; B_3) = \frac{1}{2} \int_{-1}^1 d(\hat{\mathbf{q}} \cdot \hat{\mathbf{q}}') G_0^n(\pi_3(\mathbf{q}, \mathbf{q}'), q'; B_3) = -\frac{A}{qq'} Q_0(z_{nn}) \quad (48b)$$

with Q_l the Legendre function of the second kind, which is related to the Legendre polynomial P_l by $Q_l(z) \equiv \frac{1}{2} \int_{-1}^1 dx P_l(x)/(z-x)$. The arguments z_{nn} and z_{nc} of Q_l in Eqs. (48a) and (48b) are defined by

$$z_{nc} = -\frac{1}{qq'} \left(m_n B_3 + q^2 + \frac{A+1}{2A} q'^2 \right), \quad (49a)$$

$$z_{nn} = -\frac{A}{qq'} \left(m_n B_3 + \frac{A+1}{2A} (q^2 + q'^2) \right). \quad (49b)$$

For bound states $B_3 > 0$, so all z 's are < -1 and no singularities of the Q_l 's are encountered. The superscript of X_{00}^y , $y = n, c$, indicates the particle y exchanged between the dimers in two different partitions; the subscripts denote the angular momenta of the spectator particles in the incoming/outgoing partitions. This notation is different from G_0^y , where y represents the spectator in the individual (either the incoming or outgoing) partition.

To solve the coupled integral equations, we look for an energy $E = -B_3$ where the eigenvalue of the integral-equation kernel is one. In Eqs. (47a) and (47b), regularization with a sharp ultraviolet cutoff is introduced in the momentum integration. To keep calculated low-energy observables regularization invariant the parameter $H(\Lambda)$ is tuned so that one three-body observable, such as the binding energy B_3 , is held fixed as Λ is varied. In two-neutron halos with three pairs resonantly interacting in s-waves, the resulting asymptotic running of H is characterized by a limit cycle [114, 115, 23, 24, 116, 117]. In particular, the discrete scale invariance of this problem in the ultra-violet results in $H(\Lambda)$ being a log-periodic function of Λ . Our numerical results for various A are well described by:

$$H(\Lambda) = c_A \frac{\sin(s_0 \log(\Lambda/\Lambda_*) + \arctan(s_0) + d_A)}{\sin(s_0 \log(\Lambda/\Lambda_*) - \arctan(s_0))} + e_A. \quad (50)$$

Here c_A , d_A , and e_A are constants that depend on the core/neutron mass ratio A with $d_A = e_A = 0$ when $A = 1$ and Λ_* is the renormalization parameter determined by one observable in a given two-neutron halo. The period of the limit cycle is $\exp(\pi/s_0)$, where s_0 is the solution of a transcendental equation [22, 118]:

$$\cosh^2\left(\frac{\pi s_0}{2}\right) - \cosh\left(\frac{\pi s_0}{2}\right) \frac{2 \sinh(\theta_1 s_0)}{s_0 \sin(2\theta_1)} - \frac{8 \sinh^2(\theta_2 s_0)}{s_0^2 \sin^2(2\theta_2)} = 0 \quad (51)$$

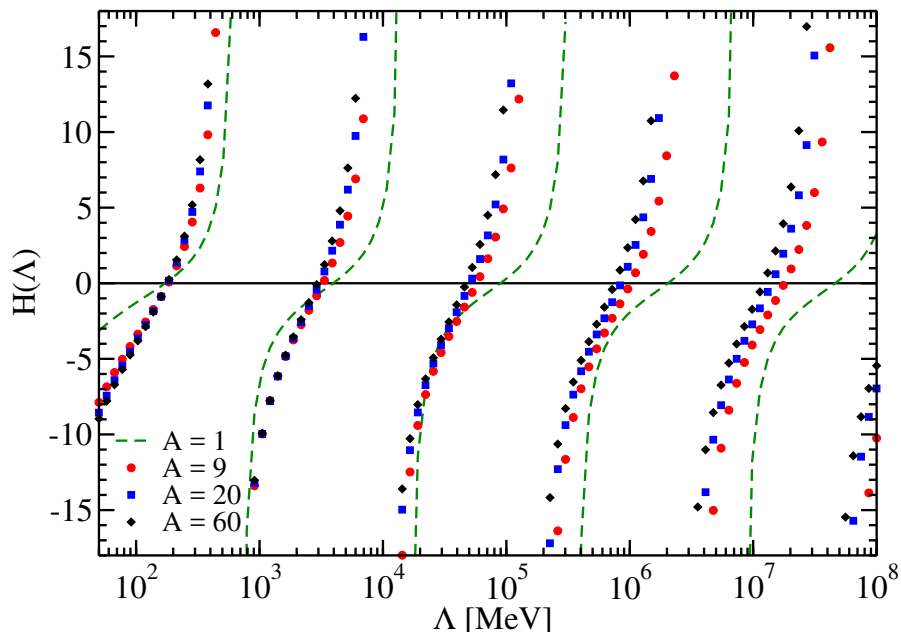


Figure 5. (Color online) The running of $H(\Lambda)$ as a function of the cutoff Λ for systems with $A = 1$ (green dashed line), $A = 9$ (red circles), $A = 20$ (blue squares), and $A = 60$ (black diamonds). The numerical results are obtained by setting $\gamma_{0,d}, \gamma_{0,\sigma} = 0$ and $B_3 = 1$ MeV.

where $\theta_1 = \arcsin(1/(1+A))$, $\theta_2 = \arcsin \sqrt{A/(2+2A)}$. Eq. (50) was first derived in systems of three equal-mass particles [23, 24], where $s_0 = 1.00624$ is obtained from Eq. (51). This corresponds to a discrete scaling factor $\exp(\pi/s_0) = 22.694$ and reveals the presence of the Efimov effect in that case [20]. The log-periodicity of $H(\Lambda)$ persists when the core and neutron masses are not equal. The running of $H(\Lambda)$, shown in Fig. 5, clearly indicates that the limit-cycle behavior is present for values of $A > 1$. The numerical results shown there are obtained by setting $\gamma_{0,d} = \gamma_{0,\sigma} = 0$ (i.e., working in the unitary limit) and $B_3 = 1$ MeV, but the log periodicity persists for finite but small two-body binding momenta, i.e., as long as $\gamma_{0,d}, \gamma_{0,\sigma} \ll \Lambda$.

The three-body wave function Ψ can then be obtained by connecting the three-body transition amplitudes with external one-body propagators and dimer propagators, see the Feynman diagrams in Fig. 6. The wave function can be represented in two different Jacobi partitions labeled by the spectator n or c . In s-wave two-neutron halos, we obtain [112, 113]

$$\begin{aligned} \Psi_n(p, q) = G_0^n(p, q; B_3) & \left[\tau_\sigma(q; B_3) \tilde{A}_n(q) + \frac{1}{2} \int_{-1}^1 d(\hat{\mathbf{p}} \cdot \hat{\mathbf{q}}) \tau_\sigma(\pi_3(\mathbf{p}, -\mathbf{q}); B_3) \tilde{A}_n(\pi_3(\mathbf{p}, -\mathbf{q})) \right. \\ & \left. + \frac{1}{2} \int_{-1}^1 d(\hat{\mathbf{p}} \cdot \hat{\mathbf{q}}) \tau_d(\pi_1(\mathbf{p}, -\mathbf{q}); B_3) \tilde{A}_c(\pi_1(\mathbf{p}, -\mathbf{q})) \right], \end{aligned} \quad (52)$$

and with the core as a spectator:

$$\Psi_c(p, q) = G_0^c(p, q; B_3) \left[\tau_d(q; B_3) \tilde{A}_c(q) + \int_{-1}^1 d(\hat{\mathbf{p}} \cdot \hat{\mathbf{q}}) \tau_\sigma(\pi_2(\mathbf{p}, -\mathbf{q}); B_3) \tilde{A}_n(\pi_2(\mathbf{p}, -\mathbf{q})) \right].$$

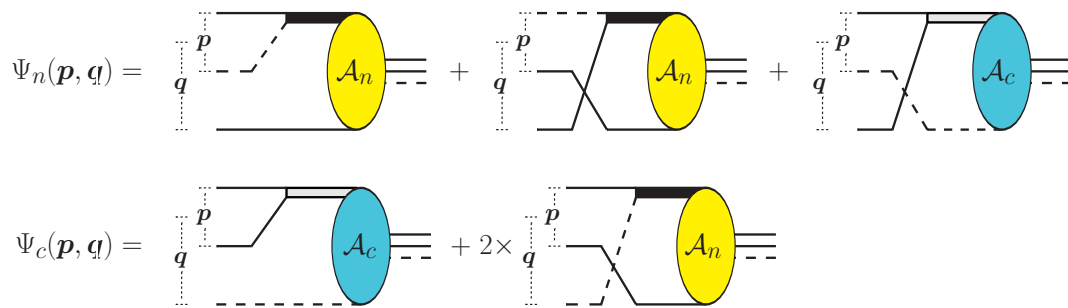


Figure 6. The bound-state $2n$ halo wave function in Jacobi momentum space representations.

(53)

With the wave function, we calculate the one-body matter-density form factors in s-wave $2n$ halos by

$$F_y(|\mathbf{k}|) = \int d^3p \int d^3q \Psi_y(p, q) \Psi_y(p, |\mathbf{q} - \mathbf{k}|), \quad (54)$$

with $y = n, c$ depending on the Jacobi partitions. For normalized wave functions $F_y(0) = 1$. The mean-square distance between the valence neutron and the center of mass of the neutron-core pair, $\langle r_{n-nc}^2 \rangle$, can be extracted from the form factor F_n via

$$F_n(|\mathbf{k}|) = 1 - \frac{1}{6} \mathbf{k}^2 \langle r_{n-nc}^2 \rangle + \dots, \quad (55)$$

and the mean-square distance between the core and the center of mass of the two-neutron pair, $\langle r_{c-nn}^2 \rangle$, is determined by

$$F_c(|\mathbf{k}|) = 1 - \frac{1}{6} \mathbf{k}^2 \langle r_{c-nn}^2 \rangle + \dots \quad (56)$$

The geometry of the neutron-neutron-core three-body system then leads to the following formula for the matter radius in a $2n$ halo:

$$\langle r_m^2 \rangle_{2n\text{-halo}} = \frac{2(A+1)^2}{(A+2)^3} \langle r_{n-nc}^2 \rangle + \frac{4A}{(A+2)^3} \langle r_{c-nn}^2 \rangle + \frac{A}{A+2} \langle r_m^2 \rangle_{\text{core}}, \quad (57)$$

where the last term is the correction from the finite matter radius of the core.

2.6. Applications: Efimov states and matter radii

In the zero-range limit, long-distance observables in three-body systems are correlated by few-body universality. One example is the Efimov effect, which is characterized by discrete scale invariance in the three-body system. In Eq. (50), the running of the three-body coupling, which is a log-periodic function of the ultraviolet cutoff, is characterized by a limit cycle with a period $\exp(\pi/s_0)$. As a consequence of the limit cycle, the three-body s-wave bound states in the unitary limit display a geometric progression. The ratio of three-body binding energies in two consecutive states is given by $\exp(2\pi/s_0)$.

Discrete scale invariance has been observed in experiments on ultracold atomic gases, where the atom-atom scattering length is tuned using a magnetic field in

the vicinity of a Feshbach resonance. Near the unitary limit, the scattering lengths associated with threshold features in atom-dimer collisions and three-atom recombination are also correlated through the scaling factor $\exp(\pi/s_0)$ (see Refs. [22, 119] for reviews).

In an s-wave $2n$ halo nucleus, $a_{0,d}$ and $a_{0,\sigma}$ are large but finite, and the three-body binding energy is characterized by the two-neutron separation energy, i.e., $S_{2n} = B_3$. In such systems, the number of possible Efimov-like halo states is determined by the two ratios E_{nn}/S_{2n} and S_{1n}/S_{2n} , where $E_{nn} = -\gamma_{0,d}^2/(2\mu_d)$ is the neutron-neutron virtual energy. Frederico, Tomio and collaborators suggested to use a universal function of the ratios E_{nn}/S_{2n} and S_{1n}/S_{2n} to explore possible Efimov states in halo nuclei, and carried out this study in a zero-range three-body model [120, 121]. Following this approach, Canham and Hammer applied EFT to explore the Efimov scenario in s-wave $2n$ halos [112]. They tuned the three-body coupling $H(\Lambda)$ so that there was an excited state of the two-neutron halo at threshold, i.e. $B_3^* = \max\{0, E_{nn}, S_{1n}\}$. The S_{2n} of the two-neutron halo is then predicted as all LO two-body and three-body EFT couplings are fixed. At this value of S_{2n} LO EFT predicts the existence of an Efimov excited state at threshold in the halo system. This, in turn, defines (for fixed A) a contour in the (S_{1n}/S_{2n}) versus (E_{nn}/S_{2n}) plane:

$$g^{(LO)}\left(\frac{E_{nn}}{S_{2n}}, \frac{S_{1n}}{S_{2n}}; A\right) = 1. \quad (58)$$

Inside the contour the three-body bound state is deep enough, or the two-body nc system is near enough to unitarity, for an Efimov state to appear in the two-neutron halo. This region is depicted in Fig. 7, and is in good agreement with an analogous study in a zero-range model [122]. The curves for different values of core-neutron mass ratio A quickly accumulate to the same region when A increases. The specific cases of ${}^3\text{H}$, ${}^{11}\text{Li}$, ${}^{12}\text{Be}$, ${}^{20,22}\text{C}$ and ${}^{62}\text{Ca}$ are indicated by mapping their up-to-date experimental data from AME2012 [78, 79] onto this two-dimensional plane.

In Fig. 7, we highlight the case of ${}^{20}\text{C}$ since the EFT analysis there is updated from Ref. [112] with new experimental data. Because of the large uncertainty in S_{1n} at the time of publication, Ref. [112] suggested that ${}^{20}\text{C}$ may display an excited Efimov state. However, experimental data on the Coulomb dissociation of ${}^{19}\text{C}$ ($S_{1n} = 0.53(13)$ MeV [63]) included in AME2012 ($S_{1n} = 0.58(9)$ MeV [78, 79]) now preclude this possibility.

The Efimov-effect correlation between bound and excited-state energies is just one example of the way in which universality imposes relations between different three-body observables. The point matter radius $\langle r_m^2 \rangle_{\text{pt}}$ of a ground-state two-neutron halo, defined by subtracting the core-size contribution from the radius of the halo in Eq. (57), is also determined by a universal function of S_{1n} and S_{2n} at LO:

$$\langle r_m^2 \rangle_{\text{pt}} \equiv \langle r_m^2 \rangle_{2n\text{-halo}} - \frac{A}{A+2} \langle r_m^2 \rangle_{\text{core}} = \frac{1}{m_n S_{2n}} f^{(LO)}\left(\frac{E_{nn}}{S_{2n}}, \frac{S_{1n}}{S_{2n}}; A\right). \quad (59)$$

Such correlations have been investigated using EFT for different s-wave two-neutron halos [112, 113, 123].

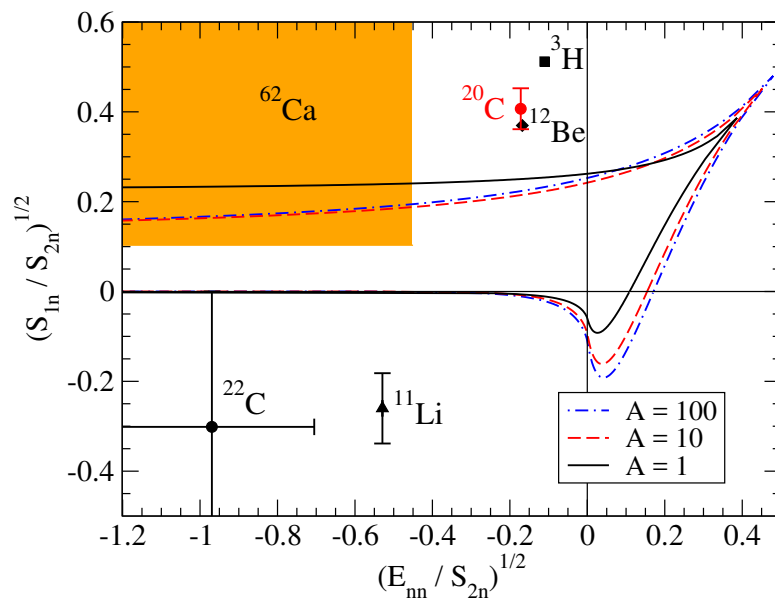


Figure 7. The contour plot in $\text{sgn}(E_{nn})\sqrt{|E_{nn}|/S_{2n}}$ versus $\text{sgn}(S_{1n})\sqrt{|S_{1n}|/S_{2n}}$ for the ground-state $2n$ halos with core-neutron mass ratios $A = 1, 10, 100$. The hypothetical bound di-neutron regime with $E_{nn} > 0$ is also included in the theoretical calculation to complete the contour.

^{22}C is a Borromean two-neutron halo. The matter radius of ^{22}C was determined in the reaction cross section measurement on a proton target to be $\langle r_m^2 \rangle_{2n\text{-halo}}^{1/2} = 5.4(9)$ fm [106]. A recent interaction cross-section measurement on a carbon target obtained a more precise result of $\langle r_m^2 \rangle_{2n\text{-halo}}^{1/2} = 3.44(8)$ fm [124], suggesting a smaller halo configuration in ^{22}C .

The $2n$ separation energy of ^{22}C is not yet directly constrained by experiment. In order to obtain an indirect constraint, Acharya *et al.* [113] performed an EFT calculation of the correlations among $\langle r_m^2 \rangle_{2n\text{-halo}}^{1/2}$, S_{1n} , and S_{2n} of ^{22}C . Using the data $\langle r_m^2 \rangle_{2n\text{-halo}}^{1/2} = 5.4(9)$ fm [106] known at the time of publication, they predicted an upper bound on S_{2n} of 0.1 MeV. This is consistent with the AME2012. It is also 20% lower than the calculation in a zero-range three-body model [125], and 50% lower than other model-dependent calculations [126]. (Note that the same matter-radius data from Ref. [106] was also used in Refs. [125, 126] as input.)

Using the recent data $\langle r_m^2 \rangle_{2n\text{-halo}}^{1/2} = 3.44(8)$ fm and the matter radius of the ^{20}C core, $\langle r_m^2 \rangle_{\text{core}}^{1/2} = 2.97_{-0.05}^{+0.03}$ fm [124], we infer a point matter radius squared $\langle r_m^2 \rangle_{\text{pt}} = 3.81_{-0.71}^{+0.82}$ fm². With this, updated, input to the LO Halo EFT calculation of Ref. [113] we obtain the correlation between S_{2n} and $-S_{1n}$ shown in Fig. 8. The three shaded regions are obtained by fixing the three-body datum $\langle r_m^2 \rangle_{\text{pt}}$ to its experimental 1σ lower bound, mean value, and upper bound respectively. The bands then depict the estimated uncertainty of our LO calculation in each case. Here we have assumed that the ^{20}C rms radius sets the scale $1/M_{\text{core}}$, and then the relative error of this LO calculation is determined by the maximum of $1/(a_{0,d}^{(nn)} M_{\text{core}})$, $\sqrt{2m_n|S_{1n}|}/M_{\text{core}}$, and

$\sqrt{2m_n S_{2n}}/M_{\text{core}}$. This contour plot determines an upper limit of $S_{2n} \leq 0.4$ MeV in ^{22}C , given the constraint that ^{22}C is a Borromean system. This value suggests a more deeply bound ^{22}C compared to the conclusion in Ref. [113]. If the information on neutron-core energy $|S_{1n}| \geq 2.8$ MeV, determined by Mosby *et al.* from the proton-removal reaction [108] is accurate, S_{2n} Fig. 8 further constrains S_{2n} to be ≤ 0.18 MeV.

The correlations unveiled in the EFT analysis allow consistency checks among different experimental results for ^{21}C and ^{22}C : it was already clear from the correlation published in Ref. [113] that a ^{22}C radius as large as that claimed by Tanaka *et al.* could only be consistent with Mosby *et al.*'s constraint on $|S_{1n}|$ if ^{22}C was incredibly weakly bound ($S_{2n} < 0.02$ MeV). The picture is clearer with the new radius measurement of $\langle r_m^2 \rangle_{2n\text{-halo}}^{1/2} = 3.44(8)$ fm, but to determine whether ^{22}C is bound by the < 0.2 MeV that is required for consistency of that number with the $|S_{1n}|$ measurement from Mosby *et al.* [108], or perhaps lies closer to the upper limit around $S_{2n} \approx 0.4$ MeV in Fig. 8, requires more precise experiments on these drip-line carbon isotopes.

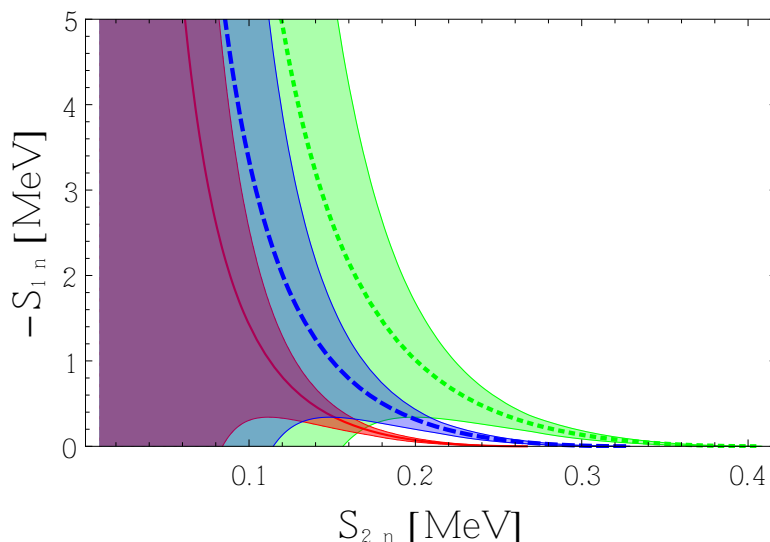


Figure 8. The correlation curve of S_{2n} versus S_{1n} in ^{22}C with fixed values of the $2n$ -halo point matter radius at $\langle r_m^2 \rangle_{\text{pt}} = 3.81$ fm² (blue, dashed), 4.63 fm² (red, solid), and 3.10 fm² (green, dotted). The shaded bands indicate the theoretical errors based on estimates of higher-order EFT corrections beyond LO.

^{62}Ca , highlighted in Fig. 7, is a special case where data are not known experimentally but are instead predicted in theory. EFT correlations were applied in Ref. [123] to investigate ^{62}Ca as a candidate for the heaviest $2n$ halo nucleus. In their work, the n - ^{60}Ca scattering parameters were extracted from the n - ^{60}Ca s-wave scattering phase shift, obtained in a coupled-cluster calculation based on chiral two- and three-nucleon interactions. This *ab initio* calculation indicated a large scattering length $a_{0,\sigma} = 54(1)$ fm and an effective range $r_{0,\sigma} = 9.0(2)$ fm for the n - ^{60}Ca system, where the error is estimated based on the spread of the coupled-cluster calculations at two small harmonic oscillator frequencies [123]. This would make ^{61}Ca a very shallow

($S_{1n} \approx 7$ keV) one-neutron halo. Using $a_{0,\sigma}$ and $r_{0,\sigma}$ as input parameters ‡, Ref. [123] performed an EFT analysis on ^{62}Ca as a n - n - ^{60}Ca two-neutron halo and searched for possible signatures of Efimov states. The EFT expansion parameter in this system is estimated from the *ab initio* results to be $M_{\text{halo}}/M_{\text{core}} \sim r_{0,\sigma}/a_{0,\sigma} = 1/6$. Ref. [123] analyzed the LO Halo EFT correlation between the n - ^{61}Ca scattering length and the two-neutron separation energy S_{2n} of the ground state of ^{62}Ca . The conclusion was that if $S_{2n} \geq 230$ keV ^{62}Ca will have an excited bound state of Efimovian character: for this value of S_{2n} , an excited state of ^{62}Ca appears at the n - ^{61}Ca threshold. Correlations among S_{2n} and the electric and matter radii of ^{62}Ca were also computed in Ref. [123].

2.7. Range corrections in three-body systems

Beyond the leading-order prediction, universal physics in two-neutron halos is affected by the finite effective range which enters EFT calculations at next-to-leading order. To calculate range effects, the three-body transition amplitudes \mathcal{A}_y (for $y = n, c$) are solved in integral equations (43a) and (43b), with the LO dimer propagator $D_x^{(0)}$ (for $x = d, \sigma$) in Eq. (42) replaced by the range-modified propagator D_x (20). However, the D_x of Eq. (20) contains a spurious pole at momenta $\approx 2/r_{0,x} \sim M_{\text{core}}$ —in addition to the physical bound- or virtual-state pole at momentum $\sim M_{\text{halo}}$. The spurious pole is outside the domain of validity of Halo EFT, but it is encountered in the integrals in the three-body equation, which probe the two-body amplitude at arbitrarily large negative energies. It can be avoided by choosing a small integration cutoff in Eqs. (43a) and (43b). However, regulation effects at such a small cutoff then complicate systematic uncertainty estimates in EFT predictions. An alternative approach is to expand D_x in powers of $r_{0,x}$. The expression at NLO is then

$$D_{x,NLO}(E, \mathbf{P}) = -\frac{2\pi}{\mu_x g_x^2 - \gamma_{0,x} + \sqrt{2\mu_x (\mathbf{P}^2/2M_x - E - i\epsilon)}} \times \left[1 + \frac{r_{0,x}}{2} \left(\gamma_{0,x} + \sqrt{2\mu_x (\mathbf{P}^2/2M_x - E - i\epsilon)} \right) \right]. \quad (60)$$

The amplitudes \mathcal{A}_y at NLO are then solved in the range-modified integral equations by the insertion of Eq. (60) into Eqs. (43a) and (43b). This partial resummation technique was used in studies of range effects for the triton [127] and was adopted in Ref. [128] to investigate range corrections in two-neutron halos. † The partial resummation formalism iterates both the LO and NLO parts of the dimer propagators in the integral equations, and thereby arbitrarily includes higher-order range corrections above NLO. These higher-order corrections are small if the regularization cutoff Λ is kept below or close to M_{core} (see e.g., Refs. [127, 65, 129] for detailed discussions on this issue).

‡ A negative $a_{0,\sigma}$ obtained from calculations at a larger harmonic oscillator frequency was not considered in the EFT analysis in Ref. [123], because that result displayed strong infrared regulator effects in these threshold parameters.

† Strictly speaking, instead of Eq. (60), which is a result for an infinitely large cutoff, D_x in Ref. [128] was obtained by regularizing the neutron-neutron and neutron-core interactions with a gaussian regulator of finite width.

	¹¹ Li	¹⁴ Be	²² C	
$\langle r_m^2 \rangle_{\text{pt}}$ [fm ²]	EFT _{LO}	5.76 ± 2.13	1.23 ± 0.96	8.99 ^{+∞} _{-5.01}
	EFT _{NLO}	6.16 ± 0.84	1.40 ± 0.85	9.28 ^{+∞} _{-5.17}
	expt	5.34 ± 0.15 [89]	4.24 ± 2.42 [89]	21.1 ± 9.7 [85, 106]
			2.90 ± 2.25 [89]	3.81 ^{+0.82} _{-0.71} [124]

Table 2. The point matter radius $\langle r_m^2 \rangle_{\text{pt}} = \langle r_m^2 \rangle_{2n\text{-halo}} - \frac{A}{A+2} \langle r_m^2 \rangle_{\text{core}}$ from EFT predictions at LO and NLO, and from experiments.

The rescaled amplitudes at NLO accuracy, $\tilde{\mathcal{A}}_{y,NLO}$, are then the solution of Eqs. (44a) and (44b), but with the τ_x 's replaced by their NLO expressions:

$$\tau_{d,NLO}(q; B_3) = \frac{2(1 + r_{0,d}\gamma_{0,d})}{-\gamma_{0,d} + \sqrt{m_n B_3 + \frac{A+2}{4A}q^2}} + r_{0,d}, \quad (61a)$$

$$\tau_{\sigma,NLO}(q; B_3) = \frac{(1 + r_{0,\sigma}\gamma_{0,\sigma})(A+1)/A}{-\gamma_{0,\sigma} + \sqrt{\frac{A}{A+1}(2m_n B_3 + \frac{A+2}{A+1}q^2)}} + \frac{A+1}{2A}r_{0,\sigma}. \quad (61b)$$

Then, in order to calculate the two-neutron halo wave functions Ψ_y at NLO, one again replaces τ_x and $\tilde{\mathcal{A}}_y$ in Eqs. (52) and (53) with the corresponding NLO quantities, i.e., $\tau_d \tilde{\mathcal{A}}_c \rightarrow \tau_{d,NLO} \tilde{\mathcal{A}}_{c,NLO}$ and $\tau_\sigma \tilde{\mathcal{A}}_n \rightarrow \tau_{\sigma,NLO} \tilde{\mathcal{A}}_{n,NLO}$.

An alternative, fully perturbative, EFT calculation of range corrections was recently carried out for two-neutron halos at NLO by Vanasse [130]. This implemented the method for calculating such perturbative insertions that he introduced and applied up to N³LO in the three-nucleon system [131, 132, 133]. Results for charge and matter form factors and radii in two neutron halos were obtained with good accuracy. We refer to Refs. [130, 133] for detailed discussions of this rigorous perturbative treatment of range effects in three-body systems.

Using the perturbative approach, Vanasse calculated the point matter radii, $\langle r_m^2 \rangle_{\text{pt}} = \langle r_m^2 \rangle_{2n\text{-halo}} - \frac{A}{A+2} \langle r_m^2 \rangle_{\text{core}}$ at NLO accuracy [130]. In Table 2, we quote Vanasse's LO and NLO point matter radii and compare with experimental results for ¹¹Li, ¹⁴Be, and ²²C [85, 89, 106, 124]. Note that to obtain his NLO numbers Vanasse estimated $r_{0,\sigma}$ by assuming it is set by the pion mass, i.e. $r_{0,\sigma} \approx 1.4$ fm. Errors were then determined as $(r_{0,\sigma} \sqrt{2m_n S_{2n}})^j$, where $j = 1$ ($j = 2$) for the LO (NLO) results shown in the first (second) column. The matter radii in two-neutron halos were previously calculated to LO in Halo EFT by Canham and Hammer [112]. Using partial resummation, they also predicted the average neutron-core and neutron-neutron distances in the neutron-neutron-core configuration at NLO accuracy [128]. The results in Refs. [112, 128, 130] are consistent with each other.

3. Halos beyond the s-wave

3.1. Lagrangian

First we consider a one-neutron halo involving p-wave interactions between the neutron and a core of spin ζ_c and mass m_c . (The case of proton halos is dealt with in Sec. 5.) Once again writing

$$\mathcal{L} = \mathcal{L}_1 + \mathcal{L}_2 + \mathcal{L}_3, \quad (62)$$

the one-body part is exactly the same as in Eq. (6).

To construct the two-body part we first note that in the case of p-wave interactions between the core and the neutron we must consider operators involving the combination of fields

$$n_\delta(i \overleftrightarrow{\partial}_i) c_a^{(\zeta_c)}, \quad (63)$$

where we have labeled the c fields according to its spin, so—as in Sec. 2.1—its subscript runs over $a = -\zeta_c, \dots, \zeta_c$. We employ the Galilean invariant derivative, $\overleftrightarrow{\partial}_i \equiv [(\overleftarrow{m}\overleftarrow{\nabla} - \overrightarrow{m}\overrightarrow{\nabla})/(\overleftarrow{m} + \overrightarrow{m})]_i$ ($i = -1, 0, 1$) with \overleftarrow{m} (or \overrightarrow{m}) the mass of the field operated on by $\overleftarrow{\nabla}$ (or $\overrightarrow{\nabla}$). By doing so we ensure that interactions constructed out of this interpolating field are invariant under Galilean boosts. We also include a factor of i in this construction so as to guarantee that, if the fields have standard time-reversal properties, it is straightforward to write down the Hermitian conjugate of interactions involving this field. The interpolating field (63) is constructed out of one derivative as well as the c and n fields, and so is the product of three irreducible representations of the rotation group. In consequence it has pieces corresponding to irreducible representations with values of j from $j = |\zeta_c - 3/2|$ to $j = \zeta_c + 3/2$. In the non-relativistic systems we consider here the total spin s is also a conserved quantum number, so we decompose the product field (63) into irreducible representations of the rotation group corresponding to particular values of j and s using Clebsch-Gordon coefficients [66]:

$$[n(i \overleftrightarrow{\partial}) c]_m^{(sj)} = \sum_{\delta=-1/2}^{1/2} \sum_{i=-1}^1 \sum_{a=-\zeta_c}^{\zeta_c} \left(\frac{1}{2} \delta_{\zeta_c a} \left| s m - i \right. \right) \left(1 i s m - i \left| j m \right. \right) n_\delta^{(1/2)}(i \overleftrightarrow{\partial}_i) c_a^{(\zeta_c)}. \quad (64)$$

In order to account for channels in which the p-wave interaction is enhanced at low energies we introduce p-wave dimer fields in those channels. For example, the one-neutron halo ^{11}Be has a spin-zero core and an enhanced p-wave interaction for the $j = 1/2$ channel, so the leading-order p-wave \mathcal{L}_2 is [66]:

$$\begin{aligned} \mathcal{L}_2^{(1/2)} = & \pi_\delta^{(1/2)\dagger} \left[w_\pi \left(i\partial_0 + \frac{\nabla^2}{2M_\sigma} \right) + \Delta_\pi^{(1/2)} \right] \pi_\delta^{(1/2)} \\ & - \frac{g_\pi^{(1/2)}}{2} \left(\pi_\delta^{(1/2)\dagger} \left[n(i \overleftrightarrow{\partial}) c \right]_\delta^{(1/2 \ 1/2)} + \left[n(i \overleftrightarrow{\partial}) c \right]_\delta^{(1/2 \ 1/2)\dagger} \pi_\delta^{(1/2)} \right). \end{aligned} \quad (65)$$

Note that repeated indices are implicitly summed, and that since the total mass is unaffected by the angular-momentum channel in which the dimer is formed $M_\sigma = m_n + m_c$ appears again here.

Channels where the p-wave interaction is of natural size will generally be suppressed by several orders in the EFT expansion. For example, the n - ^{10}Be p-wave interaction in the $j = 3/2$ channel is described by

$$\mathcal{L}_2^{(3/2)} = -\frac{C^{(3/2)}}{4} [n(i \overleftrightarrow{\partial})c]_{\beta}^{(1/2 \ 3/2)\dagger} [n(i \overleftrightarrow{\partial})c]_{\beta}^{(1/2 \ 3/2)} \quad (66)$$

where the possible values of the repeated index $\beta = -3/2, \dots, 3/2$ are summed over.

In Sec. 3.8 we consider the case of a three-body halo nucleus that is bound by p-wave interactions: we take ^6He as it is the prototypical example. In that case the dominant low-energy resonance is in the $^2\text{P}_{3/2}$ channel, in direct contrast to the situation in ^{11}Be . For this system we therefore have a four-component p-wave dimer, $\pi_{\beta}^{(3/2)}$. The three-body Lagrangian, \mathcal{L}_3 , then describes a p-wave contact interaction between this dimer and the other neutron in the system:

$$\mathcal{L}_3 = -h \left[\pi^{(3/2)} [\overleftrightarrow{\partial} n]^{(1/2 \ 3/2)} \right]^{0\dagger} \left[\pi^{(3/2)} [\overleftrightarrow{\partial} n]^{(1/2 \ 3/2)} \right]^0, \quad (67)$$

where the outer square brackets with superscript 0 indicate that the two spin-3/2 fields are coupled to form a rotational scalar.

3.2. Two-body amplitude

We now wish to compute the propagator of a dimer field of total spin j , $D_{\pi}^{(j)}(p)_{m'm}$. We proceed as we did for the s-wave dimer in Sec. 2: assuming the Lagrangian (65) the dimer obeys a Dyson equation analogous to that depicted in Fig. 3. Rather than computing the self-energy of the π field directly it is easier to compute the self-energy for the product field $n_{\delta}(i \overleftrightarrow{\partial}_i)c_a$ and then project out the piece that corresponds to the j of interest. Starting with the one-loop self-energy $\Sigma_{\pi}(E, \mathbf{P})_{i'i, \delta'\delta, a'a}$, we have

$$\Sigma_{\pi}(E, \mathbf{P})_{i'i, \delta'\delta, a'a} = \delta_{i'i} \delta_{\delta'\delta} \delta_{a'a} \Sigma(E, \mathbf{P}), \quad (68)$$

where the scalar function:

$$\Sigma(E, \mathbf{P}) = -\frac{\mu_{\sigma}(g_{\pi}^{(j)})^2}{6\pi} 2\mu_{\sigma} \left(E - \frac{\mathbf{P}^2}{2M_{\sigma}} \right) \left[i \sqrt{2\mu_{\sigma} \left(E - \frac{\mathbf{P}^2}{2M_{\sigma}} + i\epsilon \right)} + \frac{3}{2}\Lambda \right]. \quad (69)$$

Here μ_{σ} is, as above, the reduced mass in the nc channel. We have also used PDS (with scale denoted by Λ) and performed the momentum traces in three dimensions \dagger .

Since Σ is independent of δ , a and i completeness of the Clebsch-Gordon coefficients guarantees that it is also diagonal in m . That is:

$$\begin{aligned} D_{\pi}^{(j)}(E, \mathbf{P})_{m'm} &= \delta_{m'm} D_{\pi}(E, \mathbf{P}) \\ D_{\pi}(E, \mathbf{P}) &= \frac{1}{\Delta_{\pi}^{(j)} + w_{\pi}[E - \mathbf{P}^2/(2M_{\sigma})] - \Sigma(p)}. \end{aligned} \quad (70)$$

\dagger Here we have chosen to treat the factor of $1/(D-1)$ that arises in the replacement $p_i p_j \rightarrow \frac{\delta_{ij}}{D-1} p^2$ as part of the function that is analytically continued to $D = 3$ space-time dimensions when PDS is implemented. This differs from what was done in Ref. [66].

Even though it does not appear in PDS, the fact that Σ has a cubic divergence means that both parameters, $\Delta_\pi^{(j)}$ and $g_\pi^{(j)}$, are needed for renormalization [18].

Coupling the p-wave dimer to nc initial and final states generates a core-neutron amplitude in the $^{2s+1}P_j$ channel that is (in the center-of-mass frame):

$$\langle \mathbf{k}' | t_1^{(s)}(E) | \mathbf{k} \rangle = g_\pi^{(j)2} \mathbf{k}' \cdot \mathbf{k} D_\pi(E, \mathbf{0}) = \frac{6\pi}{\mu_\sigma} \frac{k^2 \cos \theta}{1/a_1^{(j)} - \frac{1}{2}r_1^{(j)}k^2 + ik^3}, \quad (71)$$

with $\cos \theta = \hat{\mathbf{k}}' \cdot \hat{\mathbf{k}}$ and $k = \sqrt{2\mu_\sigma E} = |\mathbf{k}'| = |\mathbf{k}|$ for on-shell scattering. So we have reproduced the p-wave effective-range expansion up to $\mathcal{O}(k^2)$, with $a_1^{(j)}$ the scattering volume, and $r_1^{(j)}$ the p-wave “effective range” in the channel with total angular momentum j . Note that if there are two spin channels corresponding to the same j then the couplings of fields $[n(i \overleftrightarrow{\partial})c]^{(sj)}$ for those different values of s to a spin- j dimer will, in general, be different. This, in turn, leads to different ERE parameters in those channels. This is the situation in, e.g., ^8Li , but there is only one spin channel for a spin-zero core, as is the case in ^{11}Be . The renormalization conditions that produce Eq. (71) are:

$$\frac{1}{a_1^{(j)}} = \frac{6\pi\Delta_\pi^{(j)}}{\mu_\sigma(g_\pi^{(j)})^2}; \quad (72)$$

$$r_1^{(j)} = -w_\pi \frac{6\pi}{\mu_\sigma^2(g_\pi^{(j)})^2} - 3\Lambda. \quad (73)$$

Note that $w_\pi > 0 \Rightarrow r_1^{(j)} < 0$.

3.3. Properties of the p-wave two-body bound state

As in the s-wave case (see Eq. (21)) we can use Eq. (71) to determine the positions of poles in our amplitude, and so infer the energy of any bound states. We have:

$$D_\pi(E, \mathbf{P}) = -\frac{6\pi}{\mu_\sigma^2(g_\pi^{(j)})^2} \frac{1}{r_1^{(j)} + 3\gamma_1} \frac{1}{E - \mathbf{P}^2/(2M_\sigma) + B_1} + \text{regular}. \quad (74)$$

Here $\gamma_1 = \sqrt{2\mu_\sigma B_1}$ is the solution of

$$\frac{1}{a_1^{(j)}} + \frac{1}{2}r_1^{(j)}\gamma_1^2 + \gamma_1^3 = 0. \quad (75)$$

The wave-function renormalization for the dressed π propagator can be read off as the residue of the pole:

$$Z_\pi = -\frac{6\pi}{\mu_\sigma^2 g_\pi^{(j)2}} \frac{1}{r_1^{(j)} + 3\gamma_1}. \quad (76)$$

Now, proceeding as we did for the s-wave amplitude (see discussion around Eq. (25)) we can connect this wave-function renormalization to the asymptotic normalization coefficients (ANCs) of the p-wave bound state. This time the Laurent expansion of the interacting Green’s function $G(E)$ around $E = -B_1$ takes the form:

$$\langle \mathbf{k}' | \frac{1}{E - H} | \mathbf{k} \rangle \xrightarrow{E \rightarrow -B} C_1^2 \times \sum_m \frac{\phi_m(\mathbf{k}')\phi_m^*(\mathbf{k})}{E + B_1} + \dots, \quad (77)$$

where C_1 is the ANC and $\phi_m(\mathbf{k})$ is the asymptotic wave function for a p-wave state whose eigenvalue of J_z is m . Ignoring spin for the time being, ϕ 's co-ordinate space representation is:

$$\phi_m(\mathbf{r}) = \left(1 + \frac{1}{\gamma_1 r}\right) Y_{1m}(\hat{r}) \frac{e^{-\gamma_1 r}}{r}, \quad (78)$$

while

$$C_1^{(j)2} = g_\pi^{(j)2} \frac{\gamma_1^2 \mu_\sigma^2}{3\pi} Z_\pi = -\frac{2\gamma_1^2}{r_1^{(j)} + 3\gamma_1}. \quad (79)$$

As a result, the EFT parameters, $\Delta_\pi^{(j)}$ and $g_\pi^{(j)}$ —or equivalently the scattering parameters $a_1^{(j)}$ and $r_1^{(j)}$ —can be fixed using the p-wave state's two-body binding energy, B_1 and the ANC, C_1 . Similar connections between ANCs and effective-range parameters have previously been obtained without the use of EFT, e.g. in deriving S -factor parameterizations of radiative-capture cross sections [134, 135].

In principle *ab initio* calculations can be used to determine both B_1 and C_1 . However, observables in halo systems are extremely sensitive to the two-body binding energy, so it is always wise to fix B_1 from data. Ref. [136] did obtain ANCs from an *ab initio* method: Variational Monte Carlo was used there, but any underlying theory of the neutron-core bound state could be employed. ANCs can also be measured in transfer reactions, see, e.g., Ref. [137].

3.4. Power counting, pole structure, and bounds from causality

In order to analyze the physical meaning of these poles we must specify the sizes and signs of the ERE parameters a_1 and r_1 . For causal scattering there are bounds on the parameter r_1 which imply that r_1 is always negative [138, 139, 140, 141]. Therefore, throughout what follows, we assume $r_1 < 0$. Both signs are possible for a_1 . a_1 and r_1 have dimensions, respectively, of $1/M^3$ and M . If natural scattering occurs in the p-waves then the only M that enters here is the high scale M_{core} . But, in this circumstance, all three poles of the t-matrix t_1 occur at momenta $\sim M_{\text{core}}$, and so are inaccessible to the EFT. There is thus no utility to the introduction of dimer fields in this case: all p-wave interactions are perturbative (see Sec. 4.2 below for a specific example of the order at which they enter a physical process).

For there to be a low-energy bound state or resonance, one or both of these ERE parameters must contain a power of the low scale, M_{halo} . The first paper on Halo EFT assumed

$$a_1 \sim \frac{1}{M_{\text{halo}}^3}, \quad r_1 \sim M_{\text{halo}}, \quad (80)$$

i.e., that two fine tunings, one in each of these effective-range parameters, were present [18]. In this situation all three poles in the t-matrix occur at momenta of order M_{halo} . These poles are the solutions of Eq. (75). If $a_1 < 0$ then two of them have the form $\pm k_R + ik_I$. They represent a broad, low-energy resonance that occurs at an energy $\sim \frac{M_{\text{halo}}^2}{2\mu_\sigma}$ and has a width of order that energy. The third pole is a (shallow)

bound state. (For full details on the pole structure under the power counting (80) we refer the reader to Ref. [18].)

Reference [19] pointed out that a low-energy bound state or resonance could still occur even with only one fine tuning. They suggested a scaling:

$$a_1 \sim \frac{1}{M_{\text{halo}}^2 M_{\text{core}}}, \quad r_1 \sim M_{\text{core}}. \quad (81)$$

In fact, the causality arguments referred to above guarantee that, at least for the single-channel case, r_1 is negative and at least of size M_{core} , since the range of the nc interaction in the underlying theory will typically be $1/M_{\text{core}}$. This power counting is consistent with that bound. It is then useful to rewrite t_1 as:

$$t_1(\mathbf{k}', \mathbf{k}; E) = \frac{12\pi}{\mu_\sigma |r_1|} \frac{k^2 \cos \theta}{k^2 - k_R^2 + i \frac{2k^3}{|r_1|}}, \quad (82)$$

where we have assumed $r_1 < 0$ and introduced $k_R^2 = \frac{2}{a_1 r_1} \sim M_{\text{halo}}^2$ as the momentum characteristic of the low-energy pole. If $a_1 > 0$ then this is a bound-state pole, and, up to higher-order corrections in $M_{\text{core}}/M_{\text{halo}}$, $k_R = i\gamma_1$. If $a_1 < 0$ it corresponds to a resonance, centered at $k = k_R$, and with width $\Gamma \approx \frac{2k_R^3}{\mu_\sigma |r_1|}$. Note that this width—whose presence ensures the amplitude is unitary—is parametrically small: it is of order $\frac{M_{\text{halo}}}{M_{\text{core}}}$ higher than the resonance energy $E_R \sim \frac{M_{\text{halo}}^2}{2\mu_\sigma}$ [142]. Irrespective of the sign of a_1 the expression (82) also exhibits a bound-state pole at a momentum $k \approx i|r_1|/2$. We note that this is a real, not a virtual bound state, but that since $r_1 \sim M_{\text{core}}$, it is a deep bound state that is outside the domain of validity of Halo EFT. Full formulae for the pole positions in terms of a_1 and r_1 can be found in Refs. [18] and [143].

Reference [19] then argued (following Ref. [96] for the $\Delta(1232)$ resonance in chiral EFT) that the power counting for the amplitude (82) depends fundamentally on whether k is close to k_R or not. If $|k - k_R| \gg M_{\text{halo}}^2/M_{\text{core}}$, as will generically be the case, then the LO amplitude becomes

$$t_1(\mathbf{k}', \mathbf{k}; E) = \frac{12\pi}{\mu_\sigma |r_1|} \frac{k^2 \cos \theta}{k^2 - k_R^2}. \quad (83)$$

Note that the spurious deep pole that was present in Eq. (82) has disappeared. As long as $|k - k_R| \gg M_{\text{halo}}^2/M_{\text{core}}$, the imaginary piece of the amplitude, that generates a width for the resonance at $k = k_R$, enters the p-wave amplitude only at NLO: it can be treated in perturbation theory. However, if $|k - k_R|$ is smaller, i.e., we consider a point that is kinematically close to the LO pole, then a perturbative treatment fails, because there $i \frac{2k^3}{|r_1|}$ is not small compared to $k^2 - k_R^2$. In other words, within a region around the LO poles in the k -plane whose radius is $\sim M_{\text{halo}}^{3/2}/M_{\text{core}}^{1/2}$, this unitarity piece of the amplitude must be resummed.

If $a_1 > 0$ this region of the k -plane lies within the bound-state region. Thus, when scattering is calculated the p-wave interactions can be taken as perturbative (see Eq. (85) below). This is the situation for the n - ^{10}Be system. Conversely, if $a_1 < 0$ the pole is in the scattering region, and can be neglected for bound-state calculations.

That situation prevails in computations of ${}^6\text{He}$ that assume the power counting (81). However, in either case, unitarity corrections are essential in certain situations. If $a_1 > 0$ they must be resummed when bound-state properties are computed. Similarly, in, for example, ${}^5\text{He}$ -neutron scattering, which enters in calculations of resonances in the ${}^6\text{He}$ system (cf. Ref. [144]), it is necessary to resum the unitarity correction, and so generate the finite width of ${}^5\text{He}$, within a window around $k = k_R$. Such a resummation moves the resonance pole away from the real axis, thereby rendering the scattering amplitude finite for real k . Crucially, this resummation is not necessary for large k , and so, if implemented carefully, it need not generate any spurious (deep) poles. The power counting (81) therefore reproduces the pole structure in all of the examples we will consider: ${}^5\text{He}$ ($a_1 < 0$), ${}^8\text{Li}$ and ${}^{11}\text{Be}$ (both $a_1 > 0$). Unless otherwise stated, we will assume it throughout the remainder of our article.

Finally, we give the formulae for scattering phase shifts, in both the resummed and non-resummed cases. Eq (82) implies

$$k^3 \cot \delta_1 = \frac{1}{2} r_1 (k^2 - k_R^2), \quad (84)$$

if no expansions are made. Since $|r_1| \gg k, k_R$ we generically have $\cot \delta_1$ large, which implies that δ_1 is approximately zero. Indeed

$$\delta_1 = \frac{2}{r_1} \frac{k^3}{k^2 - k_R^2} + O\left(\frac{M_{\text{halo}}}{M_{\text{core}}}\right), \quad (85)$$

again, p.v. $|k - k_R| \gg M_{\text{halo}}^2/M_{\text{core}}$. Small phase shifts imply weak scattering, which is why the imaginary part of t_1^{-1} can be treated perturbatively.

3.5. Universality and the unitary limit in p-waves

An intriguing theoretical aspect of the s-wave ERE is the ability to take the limit $r_0 \rightarrow 0$. This produces an amplitude that is “universal”, in that it depends only on the two-body scattering length and not on short-distance details of the two-particle potential. In the p-wave case, however, the causality bound [139, 140, 141] guarantees that—for short-range, energy-independent interactions— r_1 is negative and of order the breakdown scale. This is in accordance with a Wilsonian renormalization group analysis of the p-wave case [57].

In particular, the causality bound on r_1 in the limit $|a_1| \rightarrow \infty$ reads $r_1 \leq -2/R$, where R is the range of the interaction [140, 141]. As a consequence, for short-range, energy-independent interactions, the “unitary limit” $|a_1| \rightarrow \infty$ and $r_1 \rightarrow 0$ is not allowed by causality. To let $|a_1| \rightarrow \infty$, we can take the scale $M_{\text{halo}} \rightarrow 0$, which corresponds to sending $k_R \rightarrow 0$. The on-shell amplitude will then assume the form:

$$t_1(\mathbf{k}', \mathbf{k}; E) = \frac{6\pi}{\mu_\sigma} \frac{\cos \theta}{\frac{|r_1|}{2} + ik}, \quad (86)$$

for k close to zero. The arguments of the previous subsection make it clear that—at least in our preferred power counting—there is no physical justification for taking a purely unitary amplitude as a starting point for analyses of p-wave systems.

In the power counting of Ref. [18] it seems that an amplitude with $a_1 \rightarrow 0$, $r_1 \rightarrow 0$ might be physically realizable [56]. If we first take the limit $k_R \rightarrow 0$ then, in this power counting, the form (86) applies throughout the domain of validity of the EFT. The problem with this is that the pole at $k = \frac{i|r_1|}{2}$ then corresponds to a real bound state, and its residue is computed from Eq. (86) to be $Z_\pi^{\text{deep}} = -\frac{24\pi}{\mu_\sigma r_1^2} < 0$. The fact that this pole has a negative residue means it does not correspond to a normalizable state [55] (see also Ref. [54]). For poles that are outside the domain of validity of the theory (i.e. those at momenta $\sim M_{\text{core}}$) this does not have any physical consequences. However, if $r_1 \sim M_{\text{halo}}$, then, once $k_R \rightarrow 0$, the effective-range expansion (71) generates a low-energy pole with a negative residue. It follows that the limit $k_R \rightarrow 0$ can only yield a physical scattering amplitude if we have $r_1 \sim M_{\text{core}}$, and the amplitude (86) emerges only in a small region near $k = 0$. Requiring that all (physical) poles in the quantum-mechanical theory be normalizable can thus be understood as an alternative (bound-state) version of Wigner's causality argument for p-waves. Eq. (76) also implies that this requirement, when imposed on the shallow bound-state pole, fixes $r_1 < 0$ and $|r_1| > 3\gamma_1$.

3.6. Applications: ^{11}Be and ^8Li

The ^{11}Be nucleus has both a shallow s-wave state ($J^P = \frac{1}{2}^+$) and a shallow p-wave bound state ($J^P = \frac{1}{2}^-$). The binding energy of the later is the one-neutron separation energy from this state, i.e., $S_{1n}(\frac{1}{2}^-) = B_1$. The extended nature of these states ensures that ^{11}Be has a strong enhancement of the E1 transition strength at low excitation energies [87]. In this section we examine the EFT treatment of the p-wave bound state, first developed in Ref. [66]. We then discuss the similarities and differences to the case of ^8Li , where the p-wave bound state is the ground state [136, 145, 146].

Using the value $S_{1n}(\frac{1}{2}^-) = 180$ keV from Ref. [147], we infer $\gamma_1 = 17.5$ MeV. The natural scale for the core in this system is $M_{\text{core}} \approx \hbar c / (2 \text{ fm}) = 100$ MeV, see Table 1. The scattering volume a_1 of n- ^{10}Be scattering in the $\frac{1}{2}^-$ channel extracted in Ref. [148]:

$$a_1^{(1/2)} = (457 \pm 67) \text{ fm}^3, \quad (87)$$

is then of the expected size: $a_1^{(1/2)} \sim M_{\text{halo}}^{-2} M_{\text{core}}^{-1}$.

The LO amplitude (83) relates the value of $r_1^{(1/2)}$ to the values of $a_1^{(1/2)}$ and γ_1 :

$$r_1^{(1/2)} = -\frac{2}{\gamma_1^2 a_1^{(1/2)}} \quad (88)$$

and produces $r_1^{(1/2)} = (-0.54 \pm 0.08) \text{ fm}^{-1}$. This number should, however, be taken as indicative only, although it already shows that $r_1^{(1/2)} \sim M_{\text{core}}$. At NLO, Eq. (88) is corrected to:

$$r_1^{(1/2)} = -\frac{2}{\gamma_1^2 a_1^{(1/2)}} - 2\gamma_1, \quad (89)$$

which, again using Eq. (87), alters $r_1^{(1/2)}$ to $(-0.72 \pm 0.08) \text{ fm}^{-1}$. Such a $\approx 30\%$ correction is in line with the anticipated expansion parameter of Halo EFT in the ^{11}Be system.

In the case of ${}^8\text{Li}$ the core, ${}^7\text{Li}$, is a $\frac{3}{2}^-$ nucleus, and so there are two possible spin channels that contribute to the formation of ${}^8\text{Li}$: $s = 1$ and $s = 2$. ${}^8\text{Li}$ is a 2^+ state, which is bound by 2.03 MeV with respect to the n - ${}^7\text{Li}$ threshold. This implies the bound-state pole momentum $\gamma_1 = 58$ MeV. M_{core} is associated with the core breakup ${}^7\text{Li} \rightarrow t + {}^4\text{He}$ which requires 2.5 MeV of energy; this translates to $M_{\text{core}} \approx 90$ MeV.

In fact, ${}^8\text{Li}$ also has a p-wave excited state ($J^P = 1^+$), ${}^8\text{Li}^*$, that is bound by only 1.05 MeV with respect to the n - ${}^7\text{Li}$ threshold, and so is an even better halo than the ground state: its bound-state pole momentum is $\tilde{\gamma}_1 = 42$ MeV. In this system γ_1 and $\tilde{\gamma}_1$ are then considered small with respect to M_{core} , which yields a nominal expansion parameter $M_{\text{halo}}/M_{\text{core}} \approx 0.5$. Note, however, that the result found in Ref. [136], and reported below, is that the p-wave effective ranges in $j = 1$ ${}^7\text{Li}$ - n scattering are $r_1^{(2)} \approx -1.4$ fm $^{-1}$; this suggests a higher M_{core} and hence a more convergent EFT expansion.

The EFT is designed to work for bound-state energies of 1–2 MeV so it should also describe n - ${}^7\text{Li}$ scattering for neutron energies in this range. However, at approximately 0.22 MeV above the n - ${}^7\text{Li}$ threshold there is a 3^+ resonance. This resonance dominates the total cross section in a narrow window around the resonance energy, but does not affect threshold capture into either of the ${}^8\text{Li}$ bound states. The 3^+ resonance can be added as an additional dynamical degree of freedom in the EFT [145]. The set of states relevant for the low-energy dynamics of the coupled $n + {}^7\text{Li}$ - ${}^8\text{Li}$ system is depicted in Fig. 9.

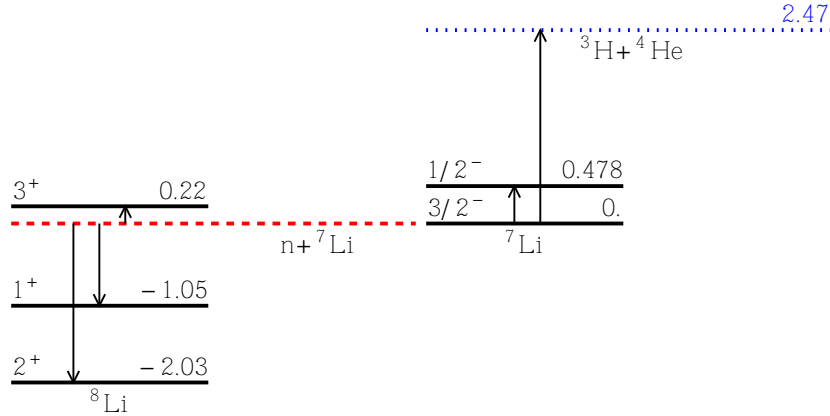


Figure 9. Our level scheme for the coupled $n + {}^7\text{Li}$ - ${}^8\text{Li}$ system. Data from Ref. [149], with all energies in MeV and measured relative to the $n + {}^7\text{Li}$ threshold. The $n - {}^7\text{Li}$ threshold is indicated by the red dashed line. The ${}^3\text{H}$ - ${}^4\text{He}$ threshold in the ${}^7\text{Li}$ system is indicated by the blue dotted line. Figure constructed using the LevelScheme scientific figure preparation package [150].

Another complication in the ${}^8\text{Li}$ system is that the first excited state of ${}^7\text{Li}$ ($J^P = 1/2^-$) has an excitation energy of only $E_* = 0.478$ MeV. Refs. [146, 145] argued that this state, which we denote here by ${}^7\text{Li}^*$, could be integrated out of the EFT. In contrast, Ref. [136] included ${}^7\text{Li}^*$ as an explicit degree of freedom in the EFT for ${}^8\text{Li}$,

	$C_{(3P_2)}$	$C_{(5P_2)}$	$C_{(3P_2^*)}$	$\tilde{C}_{(3P_1)}$	$\tilde{C}_{(5P_1)}$	$\tilde{C}_{(1P_1^*)}$	$\tilde{C}_{(3P_1^*)}$
VMC	-0.283(12)	-0.591(12)	-0.384(6)	0.220(6)	0.197(5)	-0.195(3)	-0.214(3)
EXP	-0.284(23)	-0.593(23)		0.187(16)	0.217(13)		

Table 3. ^8Li ANCs ($\text{fm}^{-\frac{1}{2}}$) for different channels. For the *ab initio* (VMC) ANCs, the $^7\text{Li} + n$ ANCs can be found in Ref. [152], while $^7\text{Li}^* + n$ ANCs are from Ref. [136]. The measured (EXP) $^7\text{Li} + n$ ANCs are from Ref. [137]. The first three ANCs pertain to the ground state of ^8Li , and the last four to $^8\text{Li}^*$.

since its excitation energy is small compared with the neutron separation energy of ^8Li . Ref. [136] argued that the importance of this core excitation is borne out by the ANCs for ^8Li in the asymptotic channels $n + ^7\text{Li}$ and into $n + ^7\text{Li}^*$: they are of similar size.

However, spin and angular-momentum considerations mean that $^7\text{Li}^*$ can only contribute in the $s = 1$ channel. The effective-range expansion (71) therefore governs n - ^7Li scattering in the 5P_2 channel. But, in the 3P_2 channel that conventional ERE only prevails when $k \ll \sqrt{2\mu_\sigma E_*}$. Ref. [136] derived a modified ERE that accounts for the opening of the $^7\text{Li}^* - n$ channel (see also Ref. [151]). This modifies the formulae for the ANCs of ^8Li , introducing terms that depend on the difference of γ_1 and $\sqrt{2\mu_\sigma E_*}$. It also means that we need three ANCs to completely understand the structure of the ^8Li ground state: the $s = 1$ and $s = 2$ ANCs for the n - ^7Li asymptotic state, here denoted $C_{(3P_2)}$ and $C_{(5P_2)}$, together with an $s = 1$ $^7\text{Li}^* - n$ ANC, which we write as $C_{(3P_2^*)}$. $^8\text{Li}^*$ requires four ANCs for a full description; we indicate these excited-state ANCs by \tilde{C}_X where X is a particular asymptotic state.

Ab initio results for all seven of these ANCs were reported in Refs. [152, 136], and are reproduced in Table 3. They were computed from a Hamiltonian consisting of the Argonne v_{18} two-nucleon terms [153] and Urbana IX three-nucleon terms [154] and using the Variational Monte Carlo (VMC) method. VMC wave functions are not as precise as Green's function Monte Carlo (GFMC) wave functions, but are quite accurate for many purposes. The ANCs in Table 3 typically have an error of $< 5\%$ due to Monte Carlo sampling. There is a possibly larger but unknown error from the accuracy of the wave functions and underlying Hamiltonian. However, limited testing with other *ab initio* wave functions suggests that this error is no larger than the experimental errors [152, 155]. On the experimental side, n - ^7Li ANCs were measured in Ref. [137], and these numbers are also given in Table 3. By using the theory ANCs (first line of Table 3) the effective range at NLO in the $j = 2$ channel where the ^8Li bound state lives was determined to be $r_1^{(2)} = -1.43(2) \text{ fm}^{-1}$. This implies that the radius of convergence of the EFT that describes ^8Li is larger than the naive estimate of 90 MeV. However, it is important to note that $|r_1^{(2)} + 3\gamma_1|$ is markedly smaller than $|r_1^{(2)}|$, and so NLO corrections in the ANCs can give large effects, even though they are nominally of order $\gamma_1/|r_1^{(2)}| \sim 1/5$.

‡ In the case of ^8Li we replace the notation $C_1^{(j)}$ for the p-wave ANC by spectroscopic-notation subscripts to make explicit the spin of the different n - ^7Li and n - $^7\text{Li}^*$ channels.

3.7. Application: low-lying ${}^2P_{3/2}$ resonance in ${}^5\text{He}$

The $n\alpha$ interaction has a low-energy resonance in the ${}^2P_{3/2}$ partial wave, as well as an enhanced phase shift in the ${}^2P_{1/2}$ where the resonance is somewhat broader. The first EFT treatment of $n\alpha$ scattering was carried out by Bertulani *et al.* [18], who took both the ${}^2P_{3/2}$ scattering volume $a_1^{(3/2)}$, and the corresponding effective “range”, $r_1^{(3/2)}$, as unnaturally enhanced. In contrast, Bedaque *et al.* [19] showed that the ${}^2P_{3/2}$ phase shift could be described using the power counting of Ref. [96], where the resonance’s width is only re-summed in its immediate vicinity. And indeed, the $n\alpha$ ${}^2P_{3/2}$ scattering parameters $a_1^{(3/2)} = -62.951(3) \text{ fm}^3$ and $r_1^{(3/2)} = -0.8819(11) \text{ fm}^{-1}$ [156] are consistent with the low- and high-momentum scales $M_{\text{halo}} \approx 30 \text{ MeV}$ and $M_{\text{core}} \approx \sqrt{m_n E_\alpha^*} = 140 \text{ MeV}$ in ${}^6\text{He}$. (A more recent analysis of $n\alpha$ data gives $a_1^{(3/2)} = -65.7 \text{ fm}^3$, $r_1^{(3/2)} = -0.84 \text{ fm}^{-1}$ [157], but this barely affects the scales inferred.) In the ${}^2P_{1/2}$ channel we have $a_1^{(1/2)} = -13.821(68) \text{ fm}^3$ and $r_1^{(1/2)} = -0.419(16) \text{ fm}^{-1}$. Ref. [19] took these parameters to be natural, i.e. $a_1^{(1/2)} \sim 1/M_{\text{core}}^3$, $r_1^{(1/2)} \sim M_{\text{core}}$.

The $M_{\text{halo}}/M_{\text{core}}$ expansion then works quite well for some low-energy quantities. Fig. 10 shows the results for the total cross section as a function of the neutron kinetic energy in the lab. frame. The power counting discussed above produces the dashed black line at LO and the dash-dotted line at NLO. The LO calculation incorporates only the ${}^2P_{3/2}$ channel, and omits the unitarity correction there. It does not do a good job of describing the scattering data, in part because it has the wrong threshold behavior. This is remedied at NLO, where the scattering length in the ${}^2S_{1/2}$ channel enters, and the unitarity correction in the ${}^2P_{3/2}$ channel is a perturbative effect. The data are then reproduced up to neutron energies of about $E_n = 0.5 \text{ MeV}$. At this energy one approaches the ${}^2P_{3/2}$ resonance, and so the $n\alpha$ loop effect $\sim ik^3$ can no longer be treated in perturbation theory. In this region we need to resum these loops, thereby generating the resonance width. We show the first two orders of the resummed result as the red dashed (LO) and dash-dotted (NLO) lines. At NLO this reproduces the NLO calculation of Ref. [18]. The resonance shape is well described by this calculation, as is the differential cross section.

3.8. The three-body equations in the case of ${}^6\text{He}$

3.8.1. Scales and quantum numbers The strong interaction between the neutron and ${}^4\text{He}$ in the ${}^2P_{3/2}$ channel leads us to consider a three-body system consisting of an alpha particle and two neutrons. This is a Borromean system, in that no pair of particles of these three forms a bound state, and yet there is a three-body bound system, namely ${}^6\text{He}$, which is bound by 0.975 MeV. ${}^6\text{He}$ was treated using the Gamow Shell Model in Halo EFT in Ref. [161], but that work used the power counting (80), i.e. it assumed a fine-tuned $r_1^{(3/2)}$. Ref. [143] derived the three-body equations for this system for the case (81), i.e. $r_1^{(3/2)} \sim M_{\text{core}}$, and it is those results we present here. Note that Ref. [143] took $n\alpha$ interactions in all other partial waves, including the ${}^2S_{1/2}$, to be zero at leading order, as was also assumed in Sec. 3.7. This is different from the power counting of

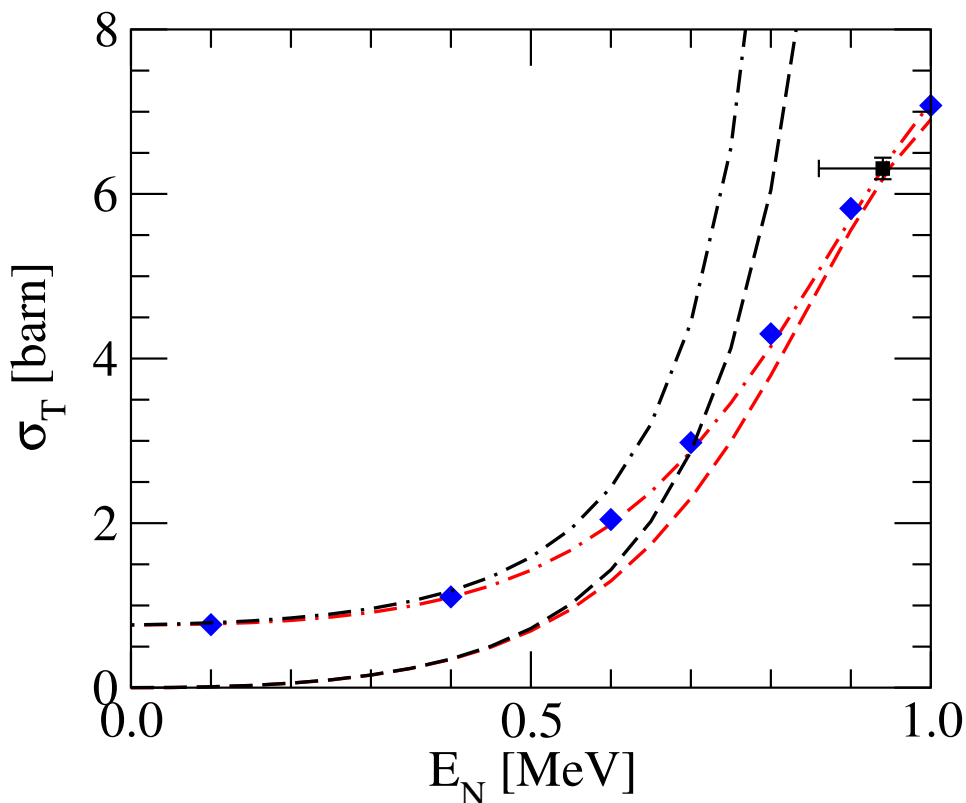


Figure 10. The total cross section for $n\alpha$ scattering (in barns) as a function of the neutron kinetic energy in the lab. frame (in MeV). The diamonds are evaluated data from Ref. [158], and the black squares are experimental data from Refs. [159, 160]. The dashed and dash-dotted black lines show the result in the power counting where $r_1 \sim M_{\text{core}}$ at LO and NLO respectively. The unitarity part of the p-wave amplitude must be resummed in the vicinity of the resonance, which leads to the red dashed and dash-dotted lines [18] [19]. Figure adapted from Ref. [19]

Ref. [19], where s-wave neutron- α scattering is a LO effect. See also Ref. [162] for a recent treatment of ${}^6\text{He}$ in Halo EFT, which considers other, different formulations of the problem at LO.

The ground-state of ${}^6\text{He}$ has total angular momentum and parity $J^P = 0^+$, and so we project our three-body equations onto that state. (For the three-body equations in other total- J channels see Refs. [56, 54].) As in Sec. 2.5 we use Jacobi-momenta \mathbf{q}_i , and \mathbf{p}_i to represent the internal kinematics of the three-body system in the center-of-mass frame. The relative orbital angular momentum, spin, and total angular momentum of the pair (jk) , as well as the relative orbital angular momentum and spin between the spectator i and the pair (jk) are also all denoted as in Sec. 2.5. With the α -core as the spectator, we obtain $l_\alpha = s_\alpha = j_\alpha = 0$, since the nn interaction is dominated by the ${}^1\text{S}_0$ virtual state. Furthermore, at LO $\lambda_\alpha = \varsigma_\alpha = 0$ and it is then straightforward to determine that $S_\alpha = L_\alpha = 0$ in the (α, nn) partition. Alternatively, if we choose a neutron as the spectator, the $n\alpha$ interaction is dominated by the ${}^2\text{P}_{3/2}$ resonance, which means $l_n = 1$, $s_n = 1/2$ and $j_n = 3/2$. In the positive parity ${}^6\text{He}$ ground state,

the spectator neutron must also interact with the $n\alpha$ pair in a p-wave. This results in $\lambda_n = 1$, $\varsigma_n = 1/2$. In the $(n, n\alpha)$ partition, the spin-spin and orbit-orbit couplings then produce two possibilities that contribute to the ${}^6\text{He}$ 0^+ ground state: the overall orbital angular momentum and overall spin can either be both zero ($L_n = S_n = 0$) or both one ($L_n = S_n = 1$). This defines the states in the basis (41) that are of relevance for our calculation of ${}^6\text{He}$.

3.8.2. Equations for the p-wave three-body bound state To obtain the equations that describe the ${}^6\text{He}$ bound state we follow the development of Sec. 2.5. Diagrammatically the equations for the ${}^6\text{He}$ problem are exactly as in Fig. 4. The key difference is technical: this time we want to project one of our equations—that for $\tilde{\mathcal{A}}_n(\mathbf{q})$ —onto a relative p-wave between the neutron and the $n\alpha$ pair. By projecting the Faddeev components $\tilde{\mathcal{A}}_\alpha$ and $\tilde{\mathcal{A}}_n$ onto the partial-wave-decomposed states in their respective partitions we obtain coupled-channel integral equations for the ${}^6\text{He}$ ground state that are formally identical to Eqs. (47a) and (47b):

$$\tilde{\mathcal{A}}_\alpha(q) = \frac{2}{\pi} \int_0^\Lambda q'^2 dq' X_{10}^n(q, q'; B_3) \tau_\pi(q'; B_3) \tilde{\mathcal{A}}_n(q'); \quad (90)$$

$$\begin{aligned} \tilde{\mathcal{A}}_n(q) &= \frac{1}{\pi} \int_0^\Lambda q'^2 dq' X_{10}^n(q, q'; B_3) \tau_d(q'; B_3) \tilde{\mathcal{A}}_\alpha(q') \\ &\quad + \frac{1}{\pi} \int_0^\Lambda q'^2 dq' \left[X_{11}^\alpha(q, q'; B_3) + \frac{qq'}{\Lambda^2} H(\Lambda) \right] \tau_\pi(q'; B_3) \tilde{\mathcal{A}}_n(q'). \end{aligned} \quad (91)$$

Here the ultraviolet cutoff, Λ , is introduced for regularization. Note that a three-body force appears here, just as it did in the s-wave case, although now it corresponds to Eq. (67), and so is a p-wave interaction between the neutron and the ${}^5\text{He}$ dimer. An $nn\alpha$ interaction of this form is consistent with the Pauli exclusion principle.

The s-wave and p-wave equations differ only in the expressions for the dimer propagators τ and for the functions X^α and X^n that encode the exchange of particles between different clusters. Since we are no longer dealing with a purely s-wave problem the exchange functions now include non-trivial recoupling coefficients ${}_i\langle p, q; \Omega_i | p', q'; \Omega_j \rangle_j$ [109] as well as a factor(s) of the pair relative momentum if one or both vertices involves a p-wave state. But the result is still essentially an angular average of the pertinent free-particle Green's function. The result of that calculation (see Ref. [143] for details) is:

$$\begin{aligned} X_{10}^n(q, q'; B_3) &= -\sqrt{2} \left[\frac{A}{A+1} \frac{1}{q'} Q_0(z_{n\alpha}) + \frac{1}{q} Q_1(z_{n\alpha}) \right], \\ X_{11}^\alpha(q, q'; B_3) &= -A \left[\frac{A^2 + 2A + 3}{(A+1)^2} Q_0(z_{nn}) + \frac{2}{A+1} \frac{q^2 + q'^2}{qq'} Q_1(z_{nn}) + Q_2(z_{nn}) \right], \end{aligned} \quad (92)$$

where Q_l are the Legendre functions of the second kind, defined in Sec. 2.5. z_{nn} is also the same here as in that section, see Eq. (49a), and $z_{n\alpha} = z_{nc}$ for the special case of an α core.

Lastly, the dimer propagator τ_d is the intermediate-state propagator for the nn state (α spectator) and is defined as in Sec. 2.5. Meanwhile, τ_π is the intermediate-state propagator of the p-wave dimer (n spectator). It takes the form:

$$\tau_\pi(q; B_3) = -\frac{2}{r_1} \left(\frac{A+1}{A} \right) \frac{1}{\frac{2A}{A+1} \left(m_n B_3 + \frac{A+2}{2(A+1)} q^2 \right) + k_R^2}. \quad (93)$$

Inserting Eq. (90) into (91) produces a single-channel integral equation that includes only the Faddeev component $\tilde{\mathcal{A}}_n$:

$$\begin{aligned} \tilde{\mathcal{A}}_n(q) &= \frac{1}{\pi} \int_0^\Lambda q'^2 dq' \left[X_{11}^\alpha(q, q'; B_3) + \frac{qq'}{\Lambda^2} H(\Lambda) \right] \tau_\pi(q'; B_3) \tilde{\mathcal{A}}_n(q') \\ &+ \frac{2}{\pi} \int_0^\Lambda q'^2 dq' \left[\frac{1}{\pi} \int_0^\Lambda q''^2 dq'' X_{10}(q, q''; B_3) \tau_d(q''; B_3) X_{10}(q', q''; B_3) \right] \tau_\pi(q'; B_3) \tilde{\mathcal{A}}_n(q'). \end{aligned} \quad (94)$$

The resulting integral equation is illustrated in Fig. 11.

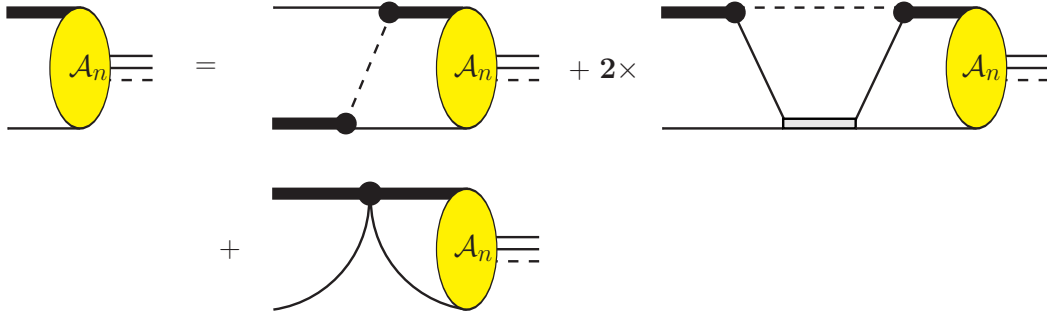


Figure 11. (Color online) The single-channel Faddeev equation for the ${}^6\text{He}$ bound state with the addition of a $nn\alpha$ counterterm in the spectator- n partition.

Eq. (94) allows us to point out a possible inconsistency of this treatment. In our power counting both X_{11}^α and $\int X_{10}\tau_d X_{10}$ are of order Q^0 while τ_π scales as $M_{\text{core}}^{-1}Q^{-2}$, with Q the typical momentum in the loop integral. It follows that each iterate of the integral equation is suppressed by one power of Q/M_{core} compared to the previous one. If the three-body equation is properly renormalized, i.e., only momenta of order M_{halo} contribute to the loop integrations, this then leads to the conclusion that there are no ${}^6\text{He}$ bound states.

Clearly this conclusion is not correct, since ${}^6\text{He}$ exists. The power counting of Ref. [18], which requires two fine-tunings in the $n\alpha$ sector, does not produce this dilemma in the three-body sector. But, in the power counting of Ref. [18] the leading-order ${}^2\text{P}_{3/2}$ dimer propagator includes the unitarity piece of the $n\alpha$ amplitude. The corresponding calculation for ${}^6\text{He}$ was carried out in Ref. [161].

3.8.3. Renormalization of the ${}^6\text{He}$ ground state First we consider the case $H(\Lambda) = 0$. With the hard cutoff Λ imposed on the integrals of Eqs. (90, 91), Ref. [143] obtained

B_3 as a function of Λ . This cutoff dependence is illustrated in Fig. 12: B_3 behaves approximately as Λ^3 at values of Λ that are large compared to k_R , $\gamma_{0,\sigma}$, and $\sqrt{2m_n B_3}$.

It is therefore essential for the $nn\alpha$ interaction $\sim H(\Lambda)$ to be present if the Halo EFT description is to yield meaningful predictions for ${}^6\text{He}$. The three-body force parameter $H(\Lambda)$ is tuned to reproduce the ${}^6\text{He}$ ground-state two-neutron separation energy $B_3 = 0.975$ MeV for all values of Λ . Note that this means that Halo EFT *cannot* predict the ${}^6\text{He}$ binding energy. The final value $B_3 = 0.975$ MeV is influenced by physics at scale M_{core} to a large enough extent that it must be imposed on the theory by hand. Correlations of this binding energy—and other input parameters in the EFT—with other ${}^6\text{He}$ observables can then be explored.

In Fig. 12 we plot the $H(\Lambda)$ that produces the experimental ${}^6\text{He}$ binding energy. The oscillatory behavior in $\log \Lambda$ is reminiscent of the three-body force's behavior in the leading-order s-wave problem (see Ref. [24] and Sec. 2.5). However, here the period of $H(\Lambda)$ in $\log \Lambda$ decreases as Λ increases. This difference in the behavior of H may well arise from the $n\alpha$ p-wave interaction in the ${}^6\text{He}$ system: the symmetry of discrete scale invariance, present in three-body systems with resonant s-wave interactions, is broken by this p-wave interaction.

Once the ${}^6\text{He}$ binding energy is renormalized the Faddeev components $\tilde{\mathcal{A}}_n(q)$, $\tilde{\mathcal{A}}_\alpha(q)$ can be calculated from Eq. (94) and Eq. (90). Fig. 13 shows the Faddeev components $\tilde{\mathcal{A}}_\alpha$ and $\tilde{\mathcal{A}}_n$ as functions of the momentum q for different values of Λ . The cutoff dependence of the low- q part of both $\tilde{\mathcal{A}}_\alpha(q)$ and $\tilde{\mathcal{A}}_n(q)$ is weak for $\Lambda > 200$ MeV.

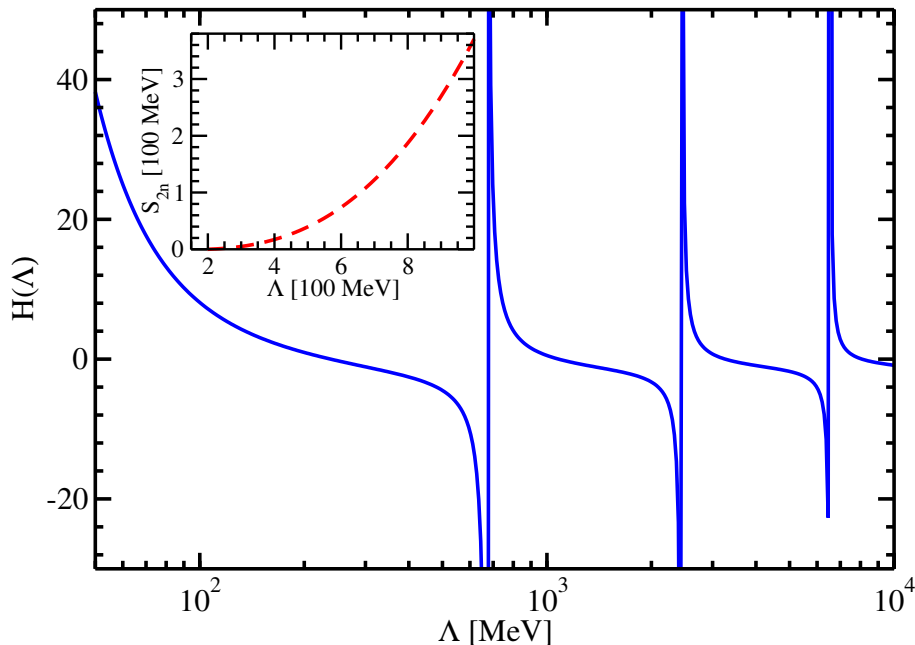


Figure 12. (Color online) The $nn\alpha$ -counterterm parameter H as a function of the cutoff Λ . H is tuned to reproduce $S_{2n} = 0.975$ MeV at each value of Λ . The inner panel shows the result for the ${}^6\text{He}$ two-neutron separation energy S_{2n} as a function of the cutoff Λ , if the equations are solved with only two-body interactions. Figure adapted from Ref. [143].

The integral equation (94) is then renormalized. It generates a shallow bound state, with characteristic momenta $\sim M_{\text{halo}}$. One three-body parameter (e.g., S_{2n}) is needed for renormalization of the LO equations that describe ${}^6\text{He}$ in Halo EFT. This conclusion remains unchanged even if a different form of the three-body force is chosen [162].

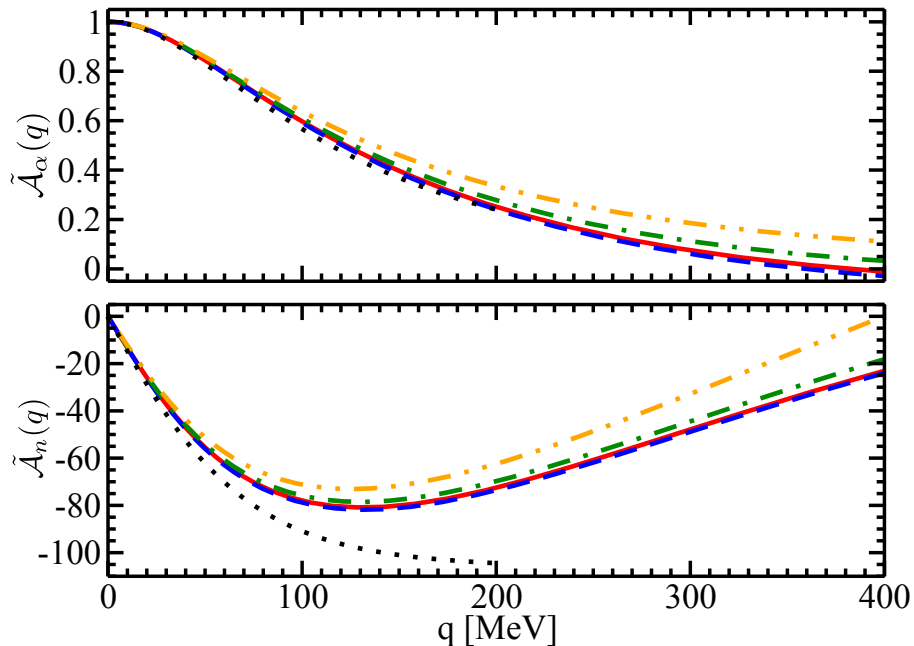


Figure 13. (Color online) The Faddeev components \tilde{A}_α and \tilde{A}_n as functions of q , calculated with cutoff parameters Λ at 200 MeV (black dotted line), 400 MeV (orange dot-dot-dashed line), 800 MeV (green dot-dashed line), 1.6 GeV (blue dashed line) and 3.2 GeV (red solid line). The Faddeev components are normalized to $\tilde{A}_\alpha(0) = 1$. Figure from Ref. [143]

3.9. Absence of the Efimov effect

Resonant pairwise p-wave interactions under the power counting of Ref. [18], were also considered by Braaten *et al.* [56]. These authors attempted to find a scale-free situation in the two-body problem, and examine the corresponding behavior in the three-body problem. In order to do so they took a p-wave “unitary limit” $|a_1| \rightarrow \infty$ and $r_1 \rightarrow 0$. However, as discussed above, this p-wave unitary limit is not physical: it yields a two-body spectrum in which one low-energy state has negative norm. Thus the discrete scale invariance, and corresponding Efimov effect, discovered by Braaten *et al.* in the corresponding three-body problem cannot be realized in nature. This has been shown in Refs. [54, 55], implying that the claim of Ref. [163], that the Efimov effect can occur with p-wave interactions, is not correct. Nishida and Tan have emphasized that this is not surprising: in three dimensions the p-wave case necessarily involves the introduction of a particular scale, namely r_1 , into the two-body interaction, thus the discrete scale invariance that is key to the Efimov effect’s appearance cannot be present [55, 164].

This is in line with the arguments based on the causality bound for p-waves discussed in subsection 3.5.

3.10. Higher partial waves

The power counting for resonant partial waves beyond the p-wave was first discussed in Refs. [18, 19]. Bertulani et al. [18] performed an analysis of the power divergences of the one-loop self energy of a dimer field with resonant interactions and concluded that for $l \geq 1$ the first $l+1$ effective range parameters are required to absorb all divergences. This agrees with a Wilsonian renormalization group analysis [57] which found two relevant parameters for the p-wave case and three relevant parameters for the d-wave case.

In Ref. [18], proper renormalization of the l th partial wave was achieved by requiring that the first $l+1$ effective range parameters must scale with M_{halo} , while all others scale with M_{core} . This power counting scenario requires $l+1$ fine tunings of parameters in the underlying theory to achieve the desired scaling, which makes resonant interactions in higher partial waves quite unlikely. Subsequently, an alternative power counting that requires a minimal number of fine tunings—one—in order to produce a low-energy resonance/bound state in any partial wave was constructed [19]. Power divergences beyond Λ^3 are suppressed by construction in this counting, which also leads to a simplified pole structure of the dimer propagator. A detailed discussion of these two scenarios in the p-wave case was given in subsection 3.4.

In Ref. [58], an alternative power counting for d-wave bound states was proposed and applied to the description of the $J^P = 5/2^+$ excited state of ^{15}C and its E2 transitions to the $J^P = 1/2^+$ ground state. This power counting requires two fine tunings. If it is extended to arbitrary $l \geq 1$, l fine tunings are required in a given partial wave. An earlier application of Halo EFT to d-waves was carried out in Ref. [165]. The authors studied the reaction $d + t \rightarrow n + \alpha$ and found it to be dominated by a ^5He , $J^P = 3/2^+$ intermediate state which couples to an αn pair with $l = 2$ in the final state. However, they used dimensional regularization with minimal subtraction which sets all power-law divergences automatically to zero and thus may have missed some contributions.

4. Electromagnetic reactions on halo nuclei

4.1. Lagrangian: electromagnetic sector

Photons are included in the Lagrangian (5) and (62) via minimal substitution:

$$\partial_\mu \rightarrow D_\mu = \partial_\mu + ie\hat{Q}A_\mu. \quad (95)$$

The charge operator \hat{Q} takes different values, depending on whether it is acting on a c field or an n field. $\hat{Q}n = 0$ for the neutron, and we denote the eigenvalue of the operator \hat{Q} for the c field as Q_c . $e^2 = 4\pi\alpha_{em}$ defines the unit of electric charge in terms of the fine-structure constant, $\alpha_{em} = 1/137.036$.

In this review our focus is on electric properties of halo nuclei. For s- and p-wave halos the dominant pieces of the electric response and electric form factor can be computed using only the Lagrangians previously introduced and the minimal substitution (95). Consequently these quantities are predictions—at least at LO, and in some cases for several orders beyond that—of the EFT. Nevertheless, eventually there will come an order in the computation where operators involving the electric field \mathbf{E} and the fields c , n , σ , and π which are gauge invariant by themselves contribute to observables.

Possible one- and two-derivative operators with one power of the photon field which involve two dimer fields are [66]:

$$\begin{aligned} \mathcal{L}_{EM}^{\sigma\pi} = & -L_{C0}^{(\sigma)} \sigma_\delta^\dagger (\nabla^2 A_0 - \partial_0 (\nabla \cdot \mathbf{A})) \sigma_\delta - L_{E1}^{(j)} \sum_{\alpha\delta} \sigma_\delta \pi_\alpha^{(j)\dagger} \left(\frac{1}{2} \delta_{j\alpha} \Big| 1k \right) (i\nabla_k A_0 - i\partial_0 A_k) \\ & - L_{C0}^{(\pi)} \sum_{\alpha} \pi_\alpha^{(j)\dagger} (\nabla^2 A_0 - \partial_0 (\nabla \cdot \mathbf{A})) \pi_\alpha^{(j)} + \text{h.c.} \end{aligned} \quad (96)$$

These operators enter in, respectively, s-wave-to-s-wave, s-wave-to-p-wave, and p-wave-to-p-wave transitions. We have chosen to write down the versions for a core spin of zero, so σ is always a spin-1/2 field, and we omit its superscript here and in what follows. The p-wave operators only occur in channels with a low-energy resonance or shallow bound state so j could be either 1/2 or 3/2, depending on the system under consideration. E1 transitions can still mediate an s-wave-to-p-wave transition even if there is no such unnatural enhancement of the p-wave scattering though, and in that case there is a non-minimal operator that does not involve the dimer π :

$$\mathcal{L}_{EM}^{\bar{j}} = -L_{E1}^{(\bar{j})} \sum_{\delta\alpha k} \sigma_\delta [n(i\overleftrightarrow{\partial})c]_\alpha^{(1/2\bar{j})\dagger} \left(\frac{1}{2} \delta_{\bar{j}\alpha} \Big| 1k \right) (i\nabla_k A_0 - i\partial_0 A_k). \quad (97)$$

The inclusion of the factor of i in the operators in Eqs. (96) and (97) that involve the electric field ensures that the Hermitian conjugation produces a time-reversal-invariant Lagrangian for real values of the couplings. This factor of i was omitted in Ref. [66], but it makes no difference to the final results presented there. Note that if we were going to consider magnetic properties we would follow a similar strategy, but in that case would construct operators involving $i\nabla_i A_j - i\nabla_j A_i$ and the neutron, core, and bound-state fields.

To determine the order at which these additional electric-field operators enter particular processes we rewrite the Lagrangian (96) and (97) in terms of rescaled fields [71, 66]. We then employ naive dimensional analysis with these fields for the operators that appear in \mathcal{L}_{EM} . This procedure generates the following results for the operators written above.

$$L_{C0}^{(\sigma)} \sim \frac{g_\sigma^2 \mu_\sigma^2}{M_{\text{core}}^3} l_{C0}^{(\sigma)}, \quad (98)$$

$$L_{E1}^{(j)} \sim \frac{g_\sigma g_\pi \mu_\sigma^2}{M_{\text{core}}} l_{E1}^{(j)}, \quad (99)$$

$$L_{C0}^{(\pi)} \sim \frac{g_\pi^2 \mu_\sigma^2}{M_{\text{core}}} l_{C0}^{(\pi)}, \quad (100)$$

$$L_{E1}^{(\bar{j})} \sim \frac{g_\sigma \mu_\sigma}{M_{\text{core}}^4} l_{E1}^{(\bar{j})}, \quad (101)$$

where the dimensionless parameters l_{\dots} are all of order one.

4.2. Coulomb Dissociation of a one-neutron s-wave halo

We first derive the dipole transition strength, $B(E1)$, for the excitation of a one-neutron halo to the core + neutron continuum state. This quantity is probed in Coulomb dissociation experiments, where the one-neutron halo is accelerated to high energies and then impinges, typically peripherally, on a target with a high charge, Q_t . We quote results from the reaction theory of Coulomb dissociation, which allows us to connect the distribution of $B(E1)$ strength with energy to observables measured in Coulomb-dissociation experiments. Coulomb dissociation is also the time-reversed version of the radiative capture process $n + c \rightarrow \sigma + \gamma$, where the halo nucleus is formed by low-energy capture together with the emission of a photon. In the case of ^{15}C this reaction is part of the carbon-nitrogen-oxygen (CNO) cycle by which helium is burnt in asymptotic-giant-branch (AGB) stars and in main-sequence stars of higher mass.

The following presentation here is an abbreviated version of material in Ref. [94]. Let us consider the transition amplitude for an E1 photon impinging on an s-wave one-neutron halo, which we will, following Sec. 2, encode as a field σ . The selection rules for this transition imply that the photon can break up the one-neutron halo into a cn continuum state, but that the lowest partial wave excited there will be a p-wave. Initially we will treat the simplest case, where there are no low-energy resonances that enhance the p-wave rescattering. This is the situation, for example, in ^{19}C . The breakup process for photon momenta $\sim M_{\text{halo}}$ is then represented in Halo EFT via the Feynman diagrams in Fig. 14. (In these, as in all Feynman diagrams in the remainder of this review, time runs from right to left.) The first diagram there scales as $1/Q$ because the core propagator scales as $1/Q^2$, and the photon-core vertex scales as Q . Rescattering in the final nc state is represented by the second diagram. Assuming that there is no low-energy resonance that enhances this rescattering the (p-wave) nc scattering vertex scales as Q^2 . Including a factor of Q for the nc loop we find that this graph is suppressed by $(M_{\text{halo}}/M_{\text{core}})^3$ compared to the first one. Finally, we could also consider a direct transition from the σ state to the nc continuum (now shown here, but see Fig. 28 for the corresponding diagram in the case of radiative capture to an s-wave proton halo). This encodes couplings of the photon to the halo nucleus at short distances and is governed by the coupling $L_{E1}^{(\bar{j})}$ of Eq. (97). This graph scales as Q^3 , being suppressed by four powers of the $M_{\text{halo}}/M_{\text{core}}$ expansion relative to LO. Note that none of the diagrams containing additional couplings and/or final-state interactions appear at NLO or N²LO and so the properties of the s-wave bound state determine the dissociation amplitude up to corrections that are suppressed by $(M_{\text{halo}}/M_{\text{core}})^3$.

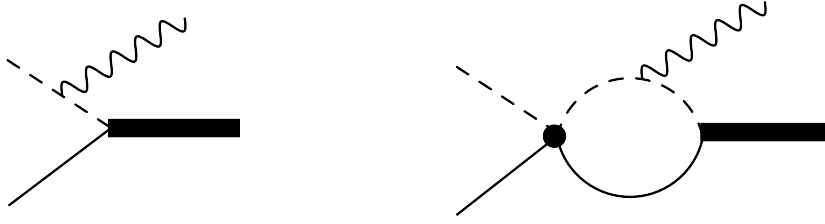


Figure 14. Diagrams contributing to the transition amplitude for the photodissociation of the halo into the core and the neutron. The first diagram represents the leading-order contribution, which is modified at next-to-leading order through multiplication by the wave-function renormalization. The second diagram occurs at $N^3\text{LO}$ in the case that there is no low-energy bound state or resonance in the p-wave that is reached through the E1 transition. Note that here, as in subsequent figures containing Feynman diagrams, time runs from right to left.

With \mathbf{q} the momentum of the photon and \mathbf{p} the final-state momentum of the core in the CM frame of the dissociation products, the amplitude can be written as

$$\mathcal{M} = \sqrt{\frac{2\pi\gamma_{0,\sigma}}{\mu_\sigma^2}} \frac{C_\sigma}{C_{\sigma,LO}} Q_c e \frac{1}{\frac{\gamma_{0,\sigma}^2}{2\mu_\sigma} + \frac{1}{2\mu_\sigma} \left(\mathbf{p} - \frac{m_n}{M_\sigma} \mathbf{q}\right)^2}. \quad (102)$$

Choosing the photon momentum to be aligned with the z-axis, we obtain the matrix element of the dipole operator, $\sqrt{\alpha_{em}} |\mathbf{r}| Y_1^0(\hat{r})$, by picking out the term linear in \mathbf{q} and then dividing by $iq\sqrt{4\pi/3}$, to get

$$\mathcal{M}_{E1}^{(l=1)} = 2\sqrt{6\gamma_{0,\sigma}} \frac{C_\sigma}{C_{\sigma,LO}} \frac{m_n}{M_\sigma} Q_c \sqrt{\alpha_{em}} \frac{p}{(\gamma_{0,\sigma}^2 + p^2)^2} \hat{\mathbf{p}} \cdot \hat{\mathbf{q}}. \quad (103)$$

Equation (103) gives the amplitude in the absence of neutron and core spin. We need to couple this result to the neutron spinor, and project to final states of good total angular momentum. Choosing $\hat{\mathbf{q}}$ parallel to the z-axis and using properties of the Clebsch-Gordan coefficients, we then obtain

$$\mathcal{M}_{E1}^{(j=3/2)} = \sqrt{2} \mathcal{M}_{E1}^{(j=1/2)} = 4\sqrt{\gamma_{0,\sigma}} \frac{C_\sigma}{C_{\sigma,LO}} \frac{m_n}{M_\sigma} Q_c \sqrt{\alpha_{em}} \frac{p}{(\gamma_{0,\sigma}^2 + p^2)^2}, \quad (104)$$

These matrix elements are related to B(E1) by

$$dB(E1) = \left(|\mathcal{M}_{E1}^{(J=1/2)}|^2 + |\mathcal{M}_{E1}^{(J=3/2)}|^2 \right) \frac{d^3p}{(2\pi)^3}, \quad (105)$$

which yields

$$\frac{dB(E1)}{dE} = \frac{12}{\pi^2} \frac{\mu_\sigma^3}{m_c^2} Q_c^2 \alpha_{em} \gamma_{0,\sigma} \frac{C_\sigma^2}{C_{\sigma,LO}^2} \frac{p^3}{(\gamma_{0,\sigma}^2 + p^2)^4}, \quad (106)$$

with $E = \frac{p^2}{2\mu_\sigma}$. The LO result is found by setting $C_\sigma = C_{\sigma,LO}$. Although here we derived the result for a spin-zero core, the same result is also found for arbitrary core spin ζ_c , as

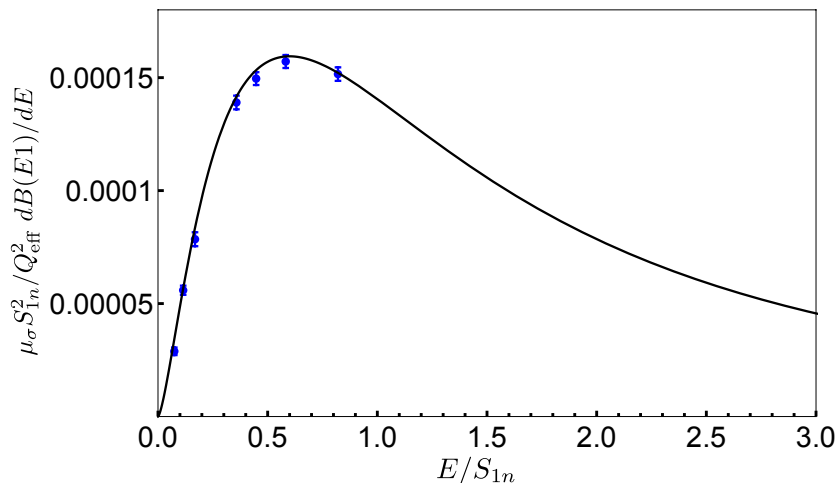


Figure 15. The universal curve (107), compared to the E1 contribution to deuteron photo disintegration obtained from the data in Ref. [170].

long as there is no enhanced p-wave channel. If we define x as the dimensionless energy ratio $x \equiv E/S_{1n}$ then the dimensionless quantity $\mu_\sigma S_{1n} \frac{dB(E1)}{dE}$ can be written

$$\mu_\sigma S_{1n}^2 \frac{dB(E1)}{dE} = \frac{C_\sigma^2}{C_{\sigma,LO}^2} \frac{3\alpha_{em} Q_{eff}^2}{\pi^2} \frac{x^{3/2}}{(1+x)^4}, \quad (107)$$

where $Q_{eff} = \frac{m_n Q_c}{m_n + m_c} = \frac{\mu_\sigma Q_c}{m_c} = \frac{Q_c}{A+1}$ is the effective charge.

Equation (106) was also derived by Rupak *et al.* in Ref. [92], where they considered the coupling of the core to the three-vector potential, \mathbf{A} , only and extracted $dB(E1)/dE$ by calculating the photo-nuclear cross-section for the E1 photon. The LO Halo EFT result (with $C_\sigma = C_{\sigma,LO}$) is also equivalent to that of Ref. [166], where a zero-range potential model was used for the neutron-core interaction. Eq. (106) can also be recovered from the framework presented in Ref. [167] (see also Ref. [168]).

Several different experimental observables can be obtained from the E1 strength distribution $\frac{dB(E1)}{dE}$. First, the total cross section for photodissociation of the nucleus by an E1 photon is then [169]:

$$\sigma^{(E1)}(\omega) = \frac{16\pi^3}{9} \omega \frac{dB(E1)}{d\omega}, \quad (108)$$

with $\omega = \frac{\gamma_{0,\sigma}^2}{2\mu_\sigma} + E$. The cross section for the core to capture the neutron into the halo state, with the excess energy radiated away via an E1 photon, is then found by detailed balance. That relation is [92, 169, 76]:

$$\sigma(E) = \frac{16\pi^3}{9} \frac{\omega^3}{2\mu_\sigma E} \frac{dB(E1)}{dE} \frac{2s+1}{2\zeta_c+1}, \quad (109)$$

where ζ_c is the spin of the core and s denotes the spin channel in which the halo is formed ‡.

‡ s is then the spin of the halo state, since we consider only captures to s -wave states in this section.

In Fig. 15 we plot a rescaled version of the curve (107), where we have divided by the factors $(C_\sigma/C_{\sigma,LO})^2$ and Q_{eff}^2 that are specific to a particular nucleus. As in Eq. (107), we have also rewritten the energies (and E1 strength) in units of the separation energy S_{1n} . This curve should then be universal to all one-neutron halos, up to the higher-order corrections that encode p-wave final-state interactions [76, 171]. To demonstrate it works for the simplest one-neutron halo we include the E1 strength for deuterium on the plot, as extracted from the asymmetry measured in Ref. [170] †. In order to remove the deuteron-specific factor of $\left(\frac{C_\sigma}{C_{\sigma,LO}}\right)^2$ from the data we have divided it by 1.69, the value of this ratio for deuterium [75].

Experimental observables for Coulomb dissociation are obtained by convolving the result (106) for the differential B(E1) transition strength as a function of energy with the distribution of (nearly real) photons generated in the target-halo collision. Results for the latter have been derived in Refs. [172, 173, 166, 169] for the case of E1-dominated dissociation upon small-angle scattering by a charged target at high beam energy. The energy spectrum resulting from the dissociation of a halo of binding energy S_{1n} is:

$$\frac{d\sigma}{dE} = \frac{16\pi^3}{9} N_{E1}(S_{1n} + E, R) \frac{dB(E1)}{dE}, \quad (110)$$

where

$$N_{E1}(\omega, R) = 2 \frac{Q_t^2 \alpha_{em}}{\pi \beta^2} \left[\xi K_0(\xi) K_1(\xi) - \frac{\beta^2}{2} \xi^2 ((K_1(\xi))^2 - (K_0(\xi))^2) \right], \quad (111)$$

with $\xi = \omega R \sqrt{1 - \beta^2} / \beta$, is the virtual photon number for the E1 multipolarity, integrated over all impact parameters larger than R , with β the beam velocity, and K_ν modified Bessel functions.

The differential cross section with respect to the center of mass angle between the dissociated fragments and the longitudinal momentum distribution of the dissociation cross section can be obtained by convolving $\frac{dB(E1)}{dE}$ with appropriate functions representing the number of virtual photons for each case, see Ref. [94] for details. The arguments used to obtain such formulae are semi-classical, involve only first-order coupling of the nucleus to the photon field, and neglect the halo-target interaction. But all those approximations are accurate for a high-charge target, such as ^{208}Pb , in the regime of small-angle/large-impact-parameter scattering [174, 175].

Refs. [63, 95] describe such a Coulomb-dissociation experiment for ^{19}C . There ^{19}C was scattered from a ^{208}Pb target, and the neutron spectrum obtained as a function of both energy and angle. The data for impact parameters $R > 30$ fm, where the nuclear contribution to the breakup is negligible, is plotted (after rescaling as described above) in Fig. 16.

These data are in good agreement with the universal curve if we take $S_{1n} = 0.58$ MeV. This shows that the older value adopted for the separation energy, $S_{1n} = 0.16(11)$

† Both here and in Ref. [170], the E1 photodissociation cross section is obtained from the measured asymmetry via multiplication by the N²LO EFT cross section of Ref. [76, 171]. That calculation is consistent with all extant low-energy cross section data. The errors shown for the E1 part of the cross section in Fig. 15 do not include any uncertainty from the EFT's N²LO total cross section.

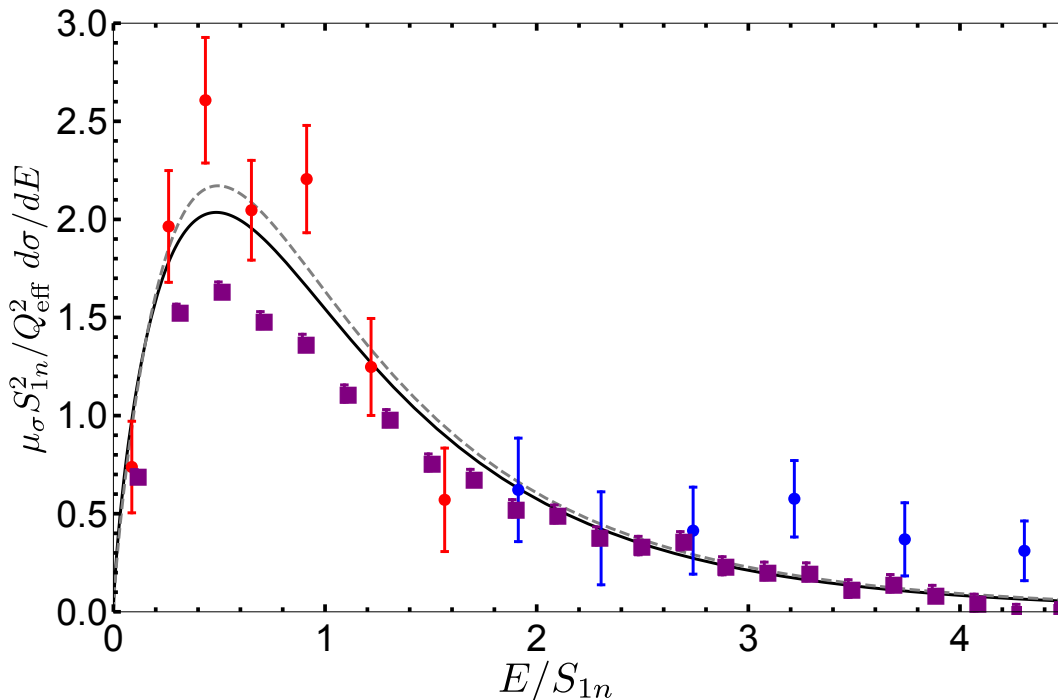


Figure 16. Rescaled Coulomb dissociation data from Refs. [87] (for ^{11}Be , purple squares) and [95] (for ^{19}C , red and blue circles), each divided by the pertinent $\left(\frac{C_\sigma}{C_{\sigma,LO}}\right)^2$, compared to the universal leading-order Halo EFT prediction for $d\sigma/dE$. Note that while the EFT prediction is universal, the experimental conditions (beam energies, detector resolution, impact parameter) for the two Coulomb-dissociation experiments were different, so the black curve shows the result for ^{19}C and the grey dashed curve for ^{11}Be .

MeV [176, 177], cannot be correct. The universal behavior of the E1 strength, in combination with these Coulomb-dissociation data, rule out such a small S_{1n} for ^{19}C .

In fact, the ^{19}C Coulomb-dissociation data are divided by the ratio $(C_\sigma/C_{\sigma,LO})^2$ extracted in Ref. [94] (see Sec. 4.4) using the red data points. The Halo EFT result is then a prediction for the blue data points. Ref. [87] discusses an analogous experiment for ^{11}Be , where p-wave interactions play a larger role—see the next subsection for discussion. In this case we take $S_{1n} = 0.50$ MeV and the data are divided by the ratio $(C_\sigma/C_{\sigma,LO})^2$ computed using the *ab initio* No-Core Shell Model with Continuum approach [91] that is described further in Sec. 6. The agreement between the ^{19}C Halo EFT result and the data is excellent, although it must be remembered that part of the data was used to fix the ANC in this case. The rescaled Halo EFT curve also does quite a good job in describing the shape of the ^{11}Be data, although there the p-wave interactions that generate the excited bound state of ^{11}Be in the $j = 1/2$ channel reduce the cross section from the universal curve, as we now discuss.

4.3. The role of p-wave final-state interactions

The formulae given in the previous section apply to any one-neutron halo without a low-energy p-wave resonance or bound state. ^{19}C fits this description, see Table 1, and its Coulomb dissociation was calculated in Ref. [94]. In contrast, some halo systems (e.g., ^{15}C and ^{11}Be) have significant final-state p-wave interactions that affect their dipole-strength distribution. These p-wave FSIs modify the above formulae. However, in the power counting we have adopted in this review the modification occurs only at NLO, because the p-wave phase shift is perturbatively small unless the scattering energy is close to the bound state or resonances, see Eq. (85). That is not the power counting that was adopted in Ref. [92] for ^{15}C : there the power counting in which both $a_1^{(1/2)}$ and $r_1^{(1/2)}$ were fine tuned was employed for the $^2\text{P}_{3/2}$ channel (we note that $r_1^{(1/2)}$ was also taken to be positive in that work). Here we focus on the case of ^{11}Be , where a perturbative treatment of the FSI is well established.

In ^{11}Be the $^2\text{P}_{3/2}$ channel can be taken as non-interacting at NLO accuracy. Meanwhile, the $^2\text{P}_{1/2}$ channel of ^{10}Be -neutron scattering has effective-range parameters that obey $a_1^{(1/2)} \sim M_{\text{core}}^{-1} M_{\text{halo}}^{-2}$ and $r_1^{(1/2)} \sim M_{\text{core}}$ (see Sec. 3). This means the the next-to-leading-order formula for the E1 strength has a term resulting from explicit calculation of the second diagram in Fig. 14. The $j = 1/2$ amplitude can be written as:

$$\begin{aligned} \mathcal{M}_{E1}^{(j=1/2)} &= \frac{C_\sigma}{C_{\sigma,LO}} Q_{\text{eff}} \sqrt{2\gamma_{0,\sigma} \alpha_{em}} e^{i\delta_1^{(1/2)}(p)} \\ &\times \frac{2p^3 \cos(\delta_1^{(1/2)}(p)) + (\gamma_{0,\sigma}^3 + 3p^2 \gamma_{0,\sigma}) \sin(\delta_1^{(1/2)}(p))}{p^2(\gamma_{0,\sigma}^2 + p^2)^2}, \end{aligned} \quad (112)$$

where $p = \sqrt{2\mu_\sigma E}$ is the final-state momentum of the neutron-core state in its center-of-mass frame. Eq. (112) is true regardless of the power counting employed for the phase shift $\delta_{1/2}$. We convert this result to the $j = 1/2$ contribution to $d\text{B}(E1)/dE$ via Eq. (105), and then use (85) to expand the result in powers of $M_{\text{halo}}/M_{\text{core}}$ and retain only the leading- and next-to-leading-order terms in that expansion. This yields:

$$\frac{d\text{B}(E1)}{dE}^{(j=1/2),\text{NLO}} = Q_{\text{eff}}^2 \mu_\sigma \alpha_{em} \frac{\gamma_{0,\sigma}}{\pi^2} \frac{4p^3}{(p^2 + \gamma_{0,\sigma}^2)^4} \left(\frac{C_\sigma^2}{C_{\sigma,LO}^2} + \frac{2\gamma_{0,\sigma}}{r_1^{(1/2)}} \frac{\gamma_{0,\sigma}^2 + 3p^2}{p^2 + \gamma_1^2} \right). \quad (113)$$

We note that the first term here is present even if there is no p-wave FSI. It tends to increase the cross section. Meanwhile, the second term opposes this enhancement, since $r_1^{(1/2)} < 0$. It depends on the parameters of the p-wave FSI: the effective ‘‘range’’ $r_1^{(1/2)}$, and the pole position γ_1 . This result must then be added to the contribution to the E1 strength from the $j = 3/2$ channel, cf. Eq. (104).

4.4. Application to ^{19}C and ^{11}Be

Since FSI is only a NLO effect in this power counting it follows that both nuclei have a leading-order E1-strength distribution given by Eq. (106) with $C_\sigma = C_{\sigma,LO}$. At NLO C_σ receives corrections that make it different from unity, and in ^{19}C these are the only

NLO effects. Eq. (106) then gives the $dB(E1)/dE$ strength distribution once $\gamma_{0,\sigma}$ and C_σ are known. The result is accurate up to FSI corrections, and these are suppressed by $(M_{\text{halo}}/M_{\text{core}})^3$ compared to leading. In fact, these FSI corrections can be calculated using the approach of the previous subsection if the p-wave parameters in the pertinent channel are known. The first counterterm in the E1 dissociation of an s-wave halo does not occur until N⁴LO (see term proportional to $L_{E1}^{(3/2)}$ in Eq. (97)).

Ref. [94] fit the parameters $\gamma_{0,\sigma}$ and C_σ to the data of Ref. [95] taken at impact parameters $R > 30$ fm and final-state $n - ^{18}\text{C}$ energies < 1 MeV. The 1σ confidence intervals obtained were (520, 630) keV for S_{1n} and (1.7, 3.2) fm for the effective range. The mean values $r_{0,\sigma} = 2.6$ fm and $S_{1n} = 575$ keV were then used in the formula (27) to remove the nucleus-specific factor $(C_\sigma/C_{\sigma,LO})^2$ from the Coulomb-dissociation data in Fig. 16.

Meanwhile ^{11}Be is governed by the NLO formula (113). The p-wave inputs $r_1^{(1/2)}$ and γ_1 —as well as C_σ and $\gamma_{0,\sigma}$ —are needed for a prediction here, Eq. (113) receives corrections at N²LO. Some of these are from N²LO terms we simply dropped in deriving the result. But the strong p-wave FSI also means that $L_{E1}^{(1/2)}$ affects the E1 dissociation of these s-wave halos already at N²LO. Since this counterterm also enters the $1/2^+$ to $1/2^-$ E1 transition amplitude (see Sec. 4.8) it can, in principle, be fixed there. However, only NLO accuracy has been achieved for ^{11}Be Coulomb dissociation in Halo EFT.

4.5. Electric radius for s-wave halos

In this section we compute the electric form factor for an s-wave halo. Measurement of any part of this form factor beyond the \mathbf{q}^2 part, i.e. the electric radius, is beyond present experimental capabilities. However, experiments such as ELISE (Electron-Ion Scattering in a Storage Ring Experiment) at FAIR [178] or SCRIT (Self-Confining Radioactive Ion Target) at RIKEN [179] should be able to perform collisions between electrons and exotic nuclei, thus mapping out the form factor’s \mathbf{q} -dependence is not beyond the bounds of possibility (cf. Ref. [180]). Of course, for the lightest s-wave one-neutron halo, deuterium, this has already been done extensively [181].

The s-wave form factor is computed by calculating the σ -irreducible vertex function for $A_0\sigma\sigma$ interactions. This object represents a photon of four-momentum q coupling to the σ state. After application of wave-function renormalization it is equal to $-ieQ_c F_E^{(\sigma)}(|\mathbf{q}|)$, where \mathbf{q} is the three-momentum of the virtual photon in the Breit frame. At LO it turns out there is only one contribution to this vertex function, the first diagram in Fig. 17. A straightforward calculation yields the LO—and hence universal—result for the electric form factor of an s-wave one-neutron halo:

$$F_E^{(\sigma)}(|\mathbf{q}|) = \frac{2\gamma_{0,\sigma}}{f|\mathbf{q}|} \arctan\left(\frac{f|\mathbf{q}|}{2\gamma_{0,\sigma}}\right), \quad (114)$$

with $f = m_n/M_\sigma = \mu_\sigma/m_c = \frac{1}{A+1}$. Note that $F_E^{(\sigma)}(0) = 1$, as it should. For the deuteron, we have $f = 1/2$, and this reduces to the LO result of Ref. [76].

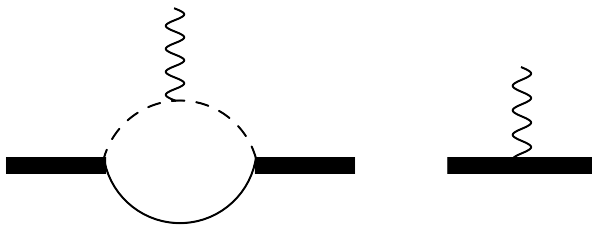


Figure 17. The LO and NLO contribution to the irreducible vertex for an A_0 photon to couple to the dimer representing an s-wave one-neutron halo. The same diagrams arise for a p-wave one-neutron halo, although in that case they both occur at leading order.

The electric radius of the s-wave state can be extracted according to:

$$F_E^{(\sigma)}(|\mathbf{q}|) \equiv 1 - \frac{1}{6} \langle r_E^2 \rangle^{(\sigma)} \mathbf{q}^2 + \dots, \quad (115)$$

and an expansion of Eq. (114) in powers of $|\mathbf{q}|$ then yields

$$\langle r_E^2 \rangle^{(\sigma)} = \frac{\mu_\sigma^2}{2m_c^2 \gamma_{0,\sigma}^2} + \langle r_E^2 \rangle_c + Q_c^{-1} \langle r_E^2 \rangle_n. \quad (116)$$

Here we have added the electric radius of the core to the right-hand side of the equation—as well as the typically much smaller radius of the neutron—since the observable that is computed in Halo EFT is the electric radius of the halo ground state taking the core and neutron as point particles. In atomic spectroscopy experiments the measured isotopoe shift is, in fact, proportional to $\langle r_E^2 \rangle^{(\sigma)} - \langle r_E^2 \rangle_c$, but in order to facilitate comparison with the way radii are usually quoted it is sensible to write the result as in Eq. (116).

At NLO there are two additions to this calculation: first, the NLO wave-function renormalization, not the LO one, must be used in calculating the contribution of Fig. 17 to $F_E^{(\sigma)}$. This increases the size of $F_E^{(\sigma)}$ by a factor of $(C_\sigma/C_{\sigma,LO})^2$. The second addition is that we must consider the operator associated with gauging the dimer kinetic term, i.e. the piece of $w_\sigma \sigma^\dagger D_0 \sigma$ in Eq. (12) that is proportional to A_0 . This generates a constant shift in the form factor that guarantees $F_E^{(\sigma)}(0) = 1$ (see right-hand diagram in Fig. 17). This second effect does not, however, affect the $|\mathbf{q}|$ dependence of $F_E^{(\sigma)}$. The overall result is an increased point electric radius at NLO, as long as $r_0 > 0$, cf. Refs. [71, 11, 66]:

$$\langle r_E^2 \rangle_{\text{pt}}^{(\sigma)} \equiv \langle r_E^2 \rangle^{(\sigma)} - \langle r_E^2 \rangle_c - Q_c^{-1} \langle r_E^2 \rangle_n = \frac{C_\sigma^2 f^2}{2C_{\sigma,LO}^2 \gamma_{0,\sigma}^2}. \quad (117)$$

The astute reader will already have noticed that the right-hand side of Eq. (117) is of a very similar form to the Halo EFT result for the matter radius $\langle r_{nc}^2 \rangle$, Eq. (34). In fact, the only difference is that $\langle r_E^2 \rangle_{\text{pt}}^{(\sigma)}$ is smaller than $\langle r_{nc}^2 \rangle$ by an overall factor of $f^2 = 1/(A+1)^2$. This factor arises because only the core has an electric coupling, and the electric radius is suppressed by a concomitant mass factor. However, the two radii probe the same physics: that of the tail of the s-wave halo state's wave function.

As emphasized in Sec. 2.2 the Halo EFT formula for the matter radius can be obtained from a quantum-mechanical calculation with a zero-range s-wave wave

function. A more rigorous way of obtaining the same result is to consider the form factor for a current that couples to the mass, rather than to the electric charge, and then imitate the field-theoretic presentation given in this section.

The result (117) for the point electric radius $\langle r_E^2 \rangle_{\text{pt}}^{(\sigma)}$, is accurate up to corrections of relative order $(M_{\text{halo}}/M_{\text{core}})^3$. The first correction to it comes only from the operator multiplying the constant $L_{C_0}^\sigma$ in Eq. (96). After wave-function renormalization this gives an effect that is parameterically $\sim M_{\text{halo}}/M_{\text{core}}^3$, and so is markedly suppressed compared to the leading $1/M_{\text{halo}}^2$ piece of the difference of squared radii. Of course, in the case of the electric radii this counting assumes that the suppression by f^2 also enters this counterterm. If that is not the case, e.g., the counterterm represents a change in the structure of the core induced by the presence of the neutron, then this short-distance physics will have a larger impact than indicated by this simple power-counting estimate.

4.6. Application: electric radii of one-neutron halos

We have demonstrated that both $\langle r_E^2 \rangle$ and $\langle r_{nc}^2 \rangle$ are sensitive to the same halo physics. Table 1 collected a number of measurements of matter radii and compared them to predictions from Halo EFT. Good agreement was seen in almost all cases. However, matter radii can be difficult to extract from data. In contrast, the measurement of an isotope shift provides much cleaner information on $\langle r_E^2 \rangle$. Unfortunately though, with one exception, the electric radius is not as sensitive to the halo physics as the matter radius, because of the suppression of the halo contribution by $f^2 = 1/(A+1)^2$.

The one exception is deuterium. From the measurement of Ref. [84] of the hydrogen-deuterium isotope shift of the 1S-2S transition we extract $\langle r_E^2 \rangle_{\text{pt}}^{1/2} = 1.97556(57)$ fm (using a neutron charge-radius squared of $\langle r_n^2 \rangle = -0.1161(22)$ fm² [182]). This is slightly discrepant with, but more accurate than, the deuteron point-charge radius we obtain from combining the CREMA collaboration's measurements of the 2S-2P transitions in muonic deuterium and muonic hydrogen, $\langle r_E^2 \rangle_{\text{pt}}^{1/2} = 1.97335(102)$ fm [183] ‡. Both are in remarkable agreement with the Halo EFT (or EFT($\not{\pi}$)) prediction [76, 75], $\langle r_E^2 \rangle_{\text{pt}}^{1/2} = 1.977$ fm.

Applying Eq. (117) to the ground state of ¹¹Be, using as input the numbers for S_{1n} and $C_\sigma/C_{\sigma,LO}$ from Table 1, we obtain $\langle r_E^2 \rangle_{\text{pt},^{11}\text{Be}}^{(\sigma)} = 0.39$ fm² at NLO. This is a post-diction of the observable associated with the isotope shift, and extracted via precise atomic spectroscopy: $\langle r_E^2 \rangle_{\text{pt},^{11}\text{Be}}^{(\sigma)} = 0.54(17)$ fm² [184]. The NLO Halo EFT result is consistent with this measurement. It assumes the ANC of the ¹¹Be ground-state obtained in the NCSMC calculation of Calci *et al.* [91]. For deuterium the ANC can be obtained by analytic continuation of the neutron-proton ³S₁ amplitude measured in scattering experiments to the bound-state pole.

In the case of ¹⁹C Ref. [94] extracted the ¹⁹C ANC listed in Table 1 from Coulomb dissociation data (cf. Sec. 4.4). Taking that prediction and the above formula for the

‡ For the purposes of this review we make no distinction between charge radii and electric radii.

radius of an s-wave one-neutron halo yields

$$\langle r_E^2 \rangle_{\text{pt},^{19}\text{C}}^{(\sigma)} = 0.09_{-0.03}^{+0.02} \text{fm}^2. \quad (118)$$

Most of the error in this (very small) predicted isotope shift comes from uncertainties in the ^{19}C binding energy and ANC extracted from the Coulomb dissociation data. A bound can be placed on the point electric radius of ^{19}C using the extractions of point-proton radii of ^{19}C and ^{18}C from the charge-changing reaction cross sections reported in Ref. [88]. Assuming the errors quoted there are uncorrelated that bound is $\langle r_E^2 \rangle_{\text{pt},^{19}\text{C}}^{(\sigma)} \leq 0.38 \text{fm}^2$ (at the 1σ level).

To our knowledge, for none of the other s-wave one-neutron halos we have discussed has an electric radius been measured.

4.7. Sum rules for the dipole strength

The non-energy weighted sum rule (NEWSR) relates the two observables considered so far in this section: the distribution of E1 strength, and the electric radius of the one-neutron halo. Its quantum-mechanical derivation rests on writing

$$\langle \sigma | \mathbf{r}^2 | \sigma \rangle = \sum_n \langle \sigma | \mathbf{r} | n \rangle \langle n | \mathbf{r} | \sigma \rangle, \quad (119)$$

where $|\sigma\rangle$ is the ground state of the nc halo and $|n\rangle$ is any complete set of states. In order to relate $\langle \sigma | \mathbf{r}^2 | \sigma \rangle$ to $dB(E1)/dE$ the states $|n\rangle$ must be eigenstates of the Hamiltonian that governs the neutron-core interaction. For a one-neutron halo without p-wave enhancement, the NEWSR is usually written:

$$\int dE \frac{dB(E1)}{dE} = \frac{3}{4\pi} \alpha_{em} Q_{\text{eff}}^2 \langle r_{nc}^2 \rangle. \quad (120)$$

Direct integration of Eq. (106) indeed produces a result that is in accord with Eq. (34).

An energy-weighted sum rule can also be derived—for any local potential—by consideration of the matrix element of $[\mathbf{r}, [H, \mathbf{r}]]$, and use of the fundamental commutator $[\mathbf{r}_i, \mathbf{p}_j] = i\delta_{ij}$. This sum rule is:

$$\int_0^\infty (E + S_{1n}) \frac{dB(E1)}{dE} = \frac{9\alpha_{em} Q_{\text{eff}}^2}{8\pi\mu_\sigma}. \quad (121)$$

It is important to note that the energy that appears in the integrand here is $E + S_{1n}$, and not just E [185]. The LO Halo EFT result for $\frac{dB(E1)}{dE}$, Eq. (106) with $C_\sigma = C_{\sigma,LO}$, obeys Eq. (121). At NLO the EWSR is *not* satisfied: the non-zero effective range is not generated by a local potential in Halo EFT.

4.8. Bound-state observables for p-wave halos

We now discuss a variety of electromagnetic observables that can be measured in p-wave one-neutron halo nuclei. We begin by examining the electric radius and the $B(E1)$ value for a transition from an s-wave to a p-wave halo state, both of which were first calculated in Halo EFT in Ref. [66]. We examine how these results apply to ^{11}Be , where such a transition occurs.

As in the s-wave case, we get the p-wave form factor by calculating contributions to the π -irreducible vertex function for $A_0\pi\pi$ interactions. There are two diagrams at LO; they have the topologies depicted in Fig. 17. The first diagram is analogous to the LO one for the s-wave state, although in the p-wave case the dimer-neutron-core vertices involve a derivative coupling that is not indicated in the figure. The second again represents a direct coupling of the photon to the π field, but, in contrast to the s-wave case, it occurs already at LO, since the p-wave dimer π must be dynamical at leading order.

In the Breit frame the coupling of an A_0 photon to the $1/2^-$ state can be written:

$$\langle \pi_\gamma^{(1/2)}(\mathbf{p}') | J^0 | \pi_\gamma^{(1/2)}(\mathbf{p}) \rangle = -ieQ_c \sum_{\delta ij} \left(\frac{1}{2} \delta 1i \middle| \frac{1}{2} \gamma \right) \left(\frac{1}{2} \delta 1j \middle| \frac{1}{2} \gamma \right) \times \left[F_E^{(\pi)}(|\mathbf{q}|) \delta_{ij} + \frac{1}{2M_\sigma^2} F_Q^{(\pi)}(|\mathbf{q}|) \left(q_i q_j - \frac{\mathbf{q}^2 \delta_{ij}}{3} \right) \right], \quad (122)$$

where $\mathbf{q} = \mathbf{p}' - \mathbf{p}$ is the three-momentum of the virtual photon. Here we have expressed the vertex function in terms of the electric and quadrupole form factors of a vector field, although the quadrupole form factor is, in fact, unobservable in the $1/2^-$ state. Choosing $\mathbf{q} = |\mathbf{q}| \hat{z}$ once again and performing a straightforward calculation yields:

$$F_E^{(\pi)}(|\mathbf{q}|) = \frac{1}{r_1^{(1/2)} + 3\gamma_1} \left[r_1^{(1/2)} + \frac{1}{|\mathbf{q}|f} \left(2|\mathbf{q}|f\gamma_1 + (|\mathbf{q}|^2 f^2 + 2\gamma_1^2) \arctan \left(\frac{f|\mathbf{q}|}{2\gamma_1} \right) \right) \right], \quad (123)$$

where again $f = m_n/M_\sigma = 1/(A+1)$. For a strict LO result $r_1^{(1/2)} + 3\gamma_1$ should be replaced by $r_1^{(1/2)}$ in Eq. (123).

$F_E^{(\pi)}(0) = 1$, as required by charge conservation. The electric radius of the p-wave state relative to the ^{10}Be ground state can be extracted according to Eq. (115), and we obtain

$$\langle r_E^2 \rangle_{\text{pt}}^{(\pi)} = -\frac{5f^2}{2\gamma_1 r_1^{(1/2)}} \quad (124)$$

Note that, once the suppression by f^2 is accounted for, this radius is $\sim M_{\text{halo}}^{-1} M_{\text{core}}^{-1}$, i.e. the p-wave halo is intrinsically more compact than an s-wave one.

This can be easily understood using simple quantum-mechanical arguments and asymptotic wave functions for the p-wave state. From this point of view the LO radius of the p-wave state is:

$$\langle r_E^2 \rangle_{\text{pt}}^{(\pi)} = \frac{2\gamma_1^2}{-r_1^{(1/2)}} f^2 \int_0^\infty dr r^2 \left(1 + \frac{1}{\gamma_1 r} \right)^2 e^{-2\gamma_1 r}. \quad (125)$$

which reproduces Eq. (124). Since the integral is finite, we can compute the contribution to it from values of $r \ll 1/\gamma_1$, and deduce that the short-distance part of the integral contributes to the total result according to:

$$\frac{\langle r_E^2 \rangle_{\text{SD}}^{(\pi)}}{\langle r_E^2 \rangle_{\text{pt}}^{(\pi)}} \sim \frac{M_{\text{halo}}}{M_{\text{core}}}. \quad (126)$$

Such arguments using the asymptotic form of the co-ordinate space wave function can be formalized using the renormalization group [186]. The parametric dependence of this short-distance contribution on $1/M_{\text{core}}$ agrees with the size of the counterterm obtained from naive dimensional analysis in Sec. 4.1.

It might seem counterintuitive that there is a short-distance contribution to $\langle r_E^2 \rangle^{(\pi)}$ already at NLO—especially when the corresponding effect does not occur in $\langle r_E^2 \rangle^{(\sigma)}$ until N³LO (see Eq. (98) and Ref. [76]). The physics of this is associated with the p-wave neutron’s tendency to get caught between the attractive potential that produces the excited state of ¹¹Be and the centrifugal barrier. Observables associated with a shallow p-wave bound state will, therefore, generically exhibit counterterms at lower order than their s-wave counterparts.

A similar effect enhances the importance of short-distance physics in the E1 transition from the $1/2^+$ state to the $1/2^-$ state (for a spin-zero core). Recall that in Sec. 4.1 we already determined that the first counterterm would enter this observable at NLO. The irreducible vertex for the s-wave-to-p-wave transition is depicted in Fig. 18. We compute the transition for a photon of arbitrary four momentum $k = (\omega, \mathbf{k})$, and the sum of diagrams yields the transition vertex function $-i\Gamma_{s's\mu}$ where s' (s) is the spin projection of the $1/2^-$ ($1/2^+$) state and μ is the polarization index of the photon.

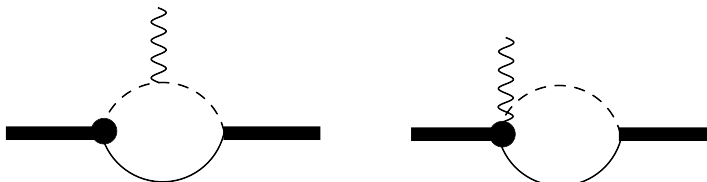


Figure 18. The two diagrams needed for the irreducible vertex that governs the s-to-p-state transition, $\Gamma_{j\mu}$ in Halo EFT at leading order.

The two diagrams depicted in Fig. 18 are both divergent, but the divergences cancel, as they must since gauge invariance precludes us from writing down any contact interaction that contributes to this observable at leading order. We also find that the sum of the two diagrams yields a conserved current [187]:

$$k^\mu \Gamma_{s's\mu} = 0. \quad (127)$$

If only the long-distance E1 mechanism on the left-hand side of Fig. 18 is considered, as was done, for example, in Ref. [188], then Eq. (127) is not satisfied.

Since we are considering electric properties, and the spin of the neutron is not affected by the photon interaction, we can choose the photon to be traveling in the \hat{z} direction, *i.e.*, $\mathbf{k} = |\mathbf{k}|\hat{z}$, and it then follows, using the definition of B(E1) strength (see, e.g. [148]), that the transition strength is related to the reduced, renormalizable irreducible vertex Γ_{++3} by:

$$\text{B(E1)} = \frac{3}{4\pi} \left(\frac{\Gamma_{++3}}{\omega} \right)^2. \quad (128)$$

Current conservation (127) provides an alternative way to calculate Γ_{++3} , since it relates the third component of the pertinent current to the zeroth component:

$$\omega\Gamma_{++0} = |\mathbf{k}|\Gamma_{++3}. \quad (129)$$

But, for Γ_{++0} , the diagram on the right of Fig. 18 needs not be considered, and so

$$\Gamma_{++0}(\mathbf{k}) \propto \int d^3r \frac{e^{-\gamma_1 r}}{r} \left(1 + \frac{1}{\gamma_1 r}\right) Y_{10}(\hat{\mathbf{r}}) e^{i\mathbf{k}\cdot\mathbf{r}} \frac{e^{-\gamma_{0,\sigma} r}}{r}, \quad (130)$$

where there is a constant of proportionality here that we have omitted. As $|\mathbf{k}| \rightarrow 0$ Eq. (130) reduces to the canonical form of the E1 matrix element.

Evaluating the integral in either momentum or co-ordinate space yields:

$$B(E1) = \frac{Q_c^2 e^2 f^2}{3\pi} \frac{\gamma_{0,\sigma}}{-r_1^{(1/2)}} \left[\frac{2\gamma_1 + \gamma_{0,\sigma}}{(\gamma_{0,\sigma} + \gamma_1)^2} \right]^2 \quad (131)$$

as the LO Halo EFT result. No cutoff parameter is needed in order to get this finite result for B(E1): our value is finite without regularization, c.f. Ref. [188]. We note that the result (131) is “universal” in the sense that it applies to any E1 s-to-p-wave transition in a one-neutron halo nucleus. Once $r_1^{(1/2)}$, γ_1 , and $\gamma_{0,\sigma}$ are known for a given one-neutron halo the prediction (131) is accurate up to corrections of order $M_{\text{halo}}/M_{\text{core}}$.

At the next order in the expansion there are corrections to the s-wave and p-wave ANCs. Both tend to increase B(E1) over the LO prediction. Short-distance effects also enter B(E1) at NLO. The B(E1) ($1/2^+ \rightarrow 1/2^-$) transition therefore cannot be predicted at NLO. This can be seen either from the presence of the operator $\sim L_{E1}^{(1/2)}$ in Eq. (96), or from a co-ordinate space argument similar to the one made above for the $1/2^-$ state’s charge radius.

4.9. Application: radius of and E1 transition to $1/2^-$ state in ^{11}Be

We choose to fix the value of the effective “range” $r_1^{(1/2)}$ in the $1/2^-$ channel in ^{11}Be by demanding that the experimental number for B(E1) obtained in Ref. [189]:

$$B(E1) = (0.098 \pm 0.004) e^2 \text{fm}^2 \quad (132)$$

is reproduced by the LO expression (131). This gives:

$$r_1^{(1/2)\text{LO}} = -0.71 \text{ fm}^{-1}, \quad (133)$$

where we do not bother to propagate the error from the experiment, since NLO effects are presumably a much larger source of uncertainty.

Numerical evaluation of the LO expression (124) then leads to the prediction for the charge radius of the ^{11}Be p-wave state relative to the ^{10}Be ground state $\langle r_E^2 \rangle_{\text{pt}}^{(\pi)} = 0.32 \text{ fm}^2$ at LO. The NLO correction to the p-wave ANC $C_1^{(1/2)}$ produces a 20% increase in $\langle r_E^2 \rangle_{\text{pt}}^{(\pi)}$, in agreement with the expectation from the power counting for ^{11}Be . However, we remind the reader that there is no prediction for the charge radius at NLO, since the operator $\sim \pi_\alpha^{(j)\dagger} (\nabla^2 A_0) \pi_\alpha^{(j)}$ enters at that order. Thus the only prediction we can offer here is a leading-order one. Using again the experimental result for the ^{10}Be charge

radius [184], we predict the (full, with core-radius included) electric radius of the $1/2^-$ state as:

$$\langle r_E^2 \rangle_{11\text{Be}^*}^{1/2} = (2.42 \pm 0.1) \text{ fm} \quad (134)$$

with the error solely from the anticipated size of NLO effects. To our knowledge there is, as yet, no experimental determination of the electric radius of the $1/2^-$ state in ^{11}Be .

4.10. Radiative capture into a p-wave halo

We now turn our attention to radiative capture from an s-wave neutron-core state to a shallow p-wave bound state, as occurs in the transition $^7\text{Li} + n \rightarrow ^8\text{Li} + \gamma$. In this section we present a LO calculation of this process, as reported in Ref. [136].

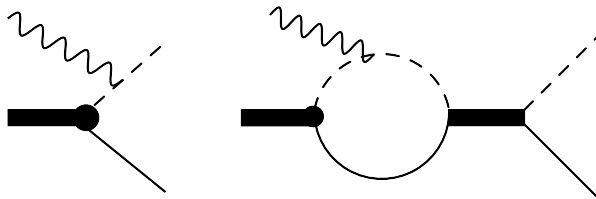


Figure 19. Tree and loop diagrams for neutron-capture to ^8Li and $^8\text{Li}^*$. The first diagram is LO for both the initial spin channels: $s = 2$ and $s = 1$. The dominant components in the initial state are 5S_2 and 3S_1 , but d-wave components also contribute. In the second diagram the incoming particles scatter in the s-wave, with that scattering amplitude encoded in the EFT via an s-wave dimer propagator. Only the $s = 2$ channel contributes at LO, while perturbative initial-state scattering effects in the $s = 1$ channel enter at NLO.

The LO tree-level diagrams for the capture reaction are shown in Fig. 19. The general incoming n - ^7Li state can be decomposed to states of initial spin $s = 2$ and $s = 1$. Both spin channels play a role in the formation of the p-wave ^8Li state, as discussed in Sec. 3.6. Therefore, in each spin channel both s- and d-wave initial-state components can contribute to the reaction. For the second, loop, diagram in Fig. 19 only the incoming s-wave contributes, and then only for $s = 2$, where there is an unnaturally large scattering length $a_{(^5S_2)} = -3.63(5) \text{ fm}$ [190]. The $s = 1$ loop diagrams do not appear until NLO because the scattering length in that channel is natural: $a_{(^3S_1)} = 0.87(7) \text{ fm}$ [190].

The loop diagram thus generates an initial-state interaction that affects only the $^5S_2 \rightarrow ^8\text{Li}(2^+) + \gamma$ partial cross section. The Lagrangian (96) implies that there is a contact term associated with this E1 $^5S_2 \rightarrow ^8\text{Li}$ transition already at NLO. However, the LO capture amplitude in this channel is a prediction of the EFT.

The differential cross section for radiative capture of two non-relativistic particles into a non-relativistic bound state is

$$\frac{d\sigma}{d\Omega} = \frac{\mu_\sigma \omega}{8\pi^2 p} \sum_i |\boldsymbol{\epsilon}_i \cdot \mathcal{M}|^2, \quad (135)$$

where ω is the energy of the outgoing photon, $p = \sqrt{2\mu_\sigma E}$ is the relative momentum of the incoming particle pair and $\boldsymbol{\epsilon}_i$ are the photon polarization vectors. The vector

amplitude \mathcal{M} is for the capture process with a vector photon A_i being emitted. Any spin indices associated with the incoming particles have been implicitly averaged over, and those associated with the bound state are implicitly summed. Note that we are working in Coulomb gauge, where the relation

$$\boldsymbol{\epsilon}_i \cdot \mathbf{q} = 0 , \quad (136)$$

for a real photon with momentum \mathbf{q} , is fulfilled.

The diagrams in Fig. 19 then yield a partial cross section:

$$\begin{aligned} \sigma = & \frac{5\pi}{2} \alpha_{em} Q_c^2 C_{({}^5P_2)}^2 \frac{\omega}{m_c^2 S_{1n} p} \\ & \times \left[|1 + X(p; a_{({}^5S_2)}, \gamma_1)|^2 - \frac{4E}{3(E + S_{1n})} \left(\frac{S_{1n}}{E + S_{1n}} + \text{Re}[X(p; a_{({}^5S_2)}, \gamma_1)] \right) \right]. \quad (137) \end{aligned}$$

In Eq. (137) $S_{1n} = \frac{\gamma_1^2}{2\mu_\sigma}$ is the one-neutron separation energy of ${}^8\text{Li}$ and X is a function that encodes loop contributions for capture from an s-wave state of relative momentum p , where there is a large scattering length, a_0 , to a p-wave state with binding momentum γ_1 . It is defined as:

$$X(p; a_0, \gamma_1) \equiv \frac{-i}{a_0^{-1} + ip} \left[p - \frac{2}{3} i \frac{\gamma_1^3 - ip^3}{\gamma_1^2 + p^2} \right]. \quad (138)$$

The factors of X are absent for the 3S_1 initial state at leading order, since the scattering length is natural there.

We display the LO result for capture into the ground and excited state in Fig. 20. The nominal accuracy of the LO amplitude is $\sim \gamma_1/r_1 \approx 20\%$, which translates into an uncertainty of $\approx 40\%$ for the cross section. There is also a much smaller uncertainty ($< 5\%$) in the cross-section prediction due to the uncertainties in the VMC ANCs, see table 3. We find agreement between theory and experiment within the combined error bars.

There is also data on the ratio of the partial cross sections associated with different initial spin states as well as for the branching ratios to different final states. LO Halo EFT results based on VMC ANCs agree very well with these data on relative amplitudes. Considering first the relative contributions of different initial spin states at $p = 0$ gives

$$\frac{\sigma[({}^3S_1) \rightarrow 2^+]}{\sigma[({}^5S_2) \rightarrow 2^+]} = \frac{\left(C_{({}^3P_2)}^{\text{LO}} \right)^2}{\left(C_{({}^5P_2)}^{\text{LO}} \right)^2 \left(1 - \frac{2}{3} \gamma_1 a_{({}^5S_2)} \right)^2}. \quad (139)$$

which says that the partial cross section for threshold or near-threshold capture from the 5S_2 initial state contributes 93% of the total. In Ref. [192] (c.f. Ref. [193]), an experimental lower bound of 86% for this ratio has been reported. Ref. [136] also predicted the corresponding ratio of $s = 2$ and $s = 1$ partial cross sections for capture to the excited state, but there is no experimental data on this ratio.

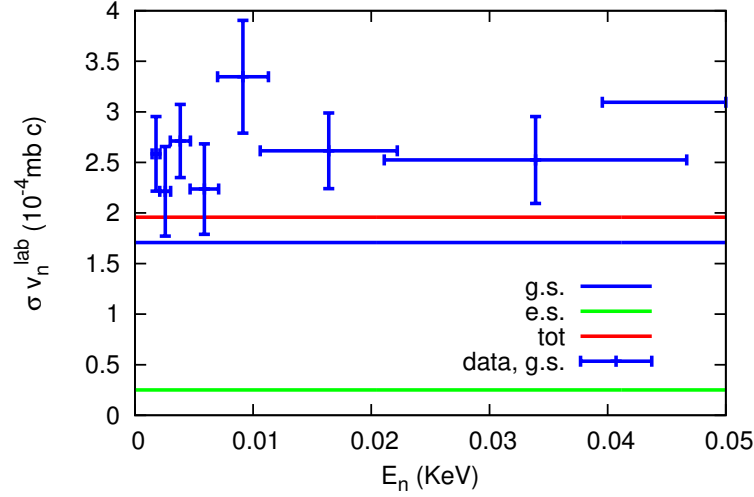


Figure 20. Total cross section \times neutron velocity vs. neutron lab energy for ${}^7\text{Li}(n, \gamma)$ at leading order in Halo EFT. “g.s.” and “e.s.” correspond to capture to ${}^8\text{Li}$ and ${}^8\text{Li}^*$, while “tot” is the sum of these two; data from Ref. [191]. Figure from Ref. [136].

Finally, we discuss the branching ratio for capture to the ground state. Near threshold, the ratio of capture cross sections is

$$\frac{\sigma(\rightarrow 1^+)}{\sigma(\rightarrow 2^+)} = \frac{3 \left(\tilde{C}_{({}^3P_1)}^{\text{LO}} \right)^2 + \left(\tilde{C}_{({}^5P_1)}^{\text{LO}} \right)^2 \left| 1 - \frac{2}{3} \tilde{\gamma}_1 a_{({}^5S_2)} \right|^2}{5 \left(C_{({}^3P_2)}^{\text{LO}} \right)^2 + \left(C_{({}^5P_2)}^{\text{LO}} \right)^2 \left| 1 - \frac{2}{3} \gamma_1 a_{({}^5S_2)} \right|^2}. \quad (140)$$

Numerical evaluation then predicts a branching ratio of 0.88 for capture to the ground state, with a theory uncertainty of ± 0.04 [136]. Note that the initial-state interaction effect of the large s-wave scattering length in $s = 2$ channels plays a role here. Refs. [194, 195], report branching ratios of 0.89 ± 0.01 for thermal neutrons and neutrons with energies of 20–70 keV respectively. Both of these are in excellent agreement with the Halo EFT number.

We note that this additional input information from *ab initio* calculations let Ref. [136] predict ratios of partial cross sections in the ${}^7\text{Li}(n, \gamma){}^8\text{Li}$ and ${}^7\text{Li}(n, \gamma){}^8\text{Li}^*$ reactions as dynamical quantities related to the couplings in the EFT Lagrangian. In contrast, the couplings of spin channels in the final state were assumed for simplicity to be equal in Ref. [146, 145] so that the branching ratios there carry no link to the actual short-range physics at work in the n - ${}^7\text{Li}$ system. Reference [146] consequently failed to satisfy the experimental lower bound on the fraction of the cross section to the ground state that comes from the 5S_2 initial state.

Nucleus	S_{2n} [MeV]	$\langle r_E^2 \rangle_{\text{pt}}$ [fm ²]
³ H	8.48	1.30
¹¹ Li	0.3693(6)	0.744
¹⁴ Be	1.27(13)	0.126
²² C	0.11(6)	0.519 ⁺ _{-0.274}

Table 4. Two-neutron separation energies and leading-order electric radii squared for four different two-neutron halos. Adapted from Refs. [133] and [130].

4.11. Electromagnetic radii of two-neutron halos

Once the radius $\langle r_{c-nn}^2 \rangle$ has been computed as described in Section 2.5 we can then form the point-electric radius of a two-neutron halo:

$$\langle r_E^2 \rangle_{\text{pt}} = \left(\frac{2}{A+2} \right)^2 \langle r_{c-nn}^2 \rangle. \quad (141)$$

This can be converted to a total electric radius by accounting for the finite electric radii of the core and the neutrons. Ref. [196] developed a gauge invariant formalism for the electric form factors of two-neutron halo nuclei and computed the electric radii of several halo nuclei. However, their calculation contained an error in the pre-factor of one term, as noted by Vanasse in Ref. [130]. In Table 4 we quote Vanasse’s LO electric radii for ¹¹Li, ¹²Be, and ²²C, together with his earlier computation of the electric radius of ³H [133]. The input parameters are the neutron-neutron scattering length, the neutron-core resonance energy, S_{1n} —which is negative for all but ³H since the other three are Borromean systems—and the two-neutron separation energy, S_{2n} . The relevant S_{1n} ’s are given in Table 1 and the assumed S_{2n} is shown in Table 4.

Electric radii have been measured for ³H and ¹¹Li. In the latter case Ref. [197] updated the earlier experimental result of Ref. [198] to obtain $\langle r_E^2 \rangle_{^{11}\text{Li}, \text{pt}} = 1.104(85)$ fm². This disagrees with the LO Halo EFT result—but the disagreement could be explained by the anticipated $\approx 40\%$ NLO corrections that the point radius will receive due to range effects. Indeed, in the case of the triton the LO result is also well away from the experimental number of 2.55(11) fm². However, Vanasse’s NLO calculation is in perfect agreement with this result: corrections due to the finite effective ranges in the NN system turn out to be large in this observable. Order-by-order results are:

$$\langle r_{^3\text{H}}^2 \rangle_{\text{pt}} = 1.30 + 1.23 + 0.096 \text{ fm}^2. \quad (142)$$

However, the triton remains the only two-neutron halo for which ranges are well-enough determined for an accurate NLO calculation like this to have been completed. An NLO computation of the ¹¹Li electric radius would be an important further development—especially in terms of investigating the role that p-wave interactions in the ¹⁰Li system have on this observable. However, in order for a definitive NLO number for the ¹¹Li electric radius to emerge the value of the effective range for s-wave n -⁹Li scattering needs to be pinned down.

4.12. Coulomb dissociation of two-neutron halos

The E1 response of a two-neutron halo is also governed by a universal function, in close analogy to the one-neutron case discussed above. Preliminary Halo EFT calculations in this direction were reported in Refs. [185, 199, 200], following work within three-body models in Refs. [201, 202]. In the case of ^{11}Li , the calculation showed good agreement with the E1 strength extracted from Coulomb dissociation data in Ref. [203] at transition energies within the domain of validity of Halo EFT.

5. Halo EFT with Coulomb

5.1. Formalism

Halo systems with two or more charged particles also have electromagnetic interactions. In Coulomb gauge, the interaction can be split into an instantaneous Coulomb interaction and the exchange of transverse photons. In the low-energy regime, the dominant effect is given by the Coulomb interaction, i.e., a static $1/r$ potential between charged particles. The exchange of transverse photons, as well as magnetic interactions, are suppressed by $(\mathbf{p}/m)^2$ where \mathbf{p} is a typical momentum and m the mass of the particle.

In halo nuclei the Coulomb interaction is repulsive. Its presence introduces a new scale, the Coulomb momentum k_C , which is given by the inverse Bohr radius of the system. This scale k_C is independent of the scales M_{halo} and M_{core} and complicates the power counting. In the effective Lagrangian, the Coulomb interaction between the core and a halo proton can be incorporated as a non-local term

$$\mathcal{L}_{\text{Cb}} = \frac{-e^2 Q_c}{\mathbf{q}^2} \int d^3y e^{-i\mathbf{q}\cdot(\mathbf{x}-\mathbf{y})} c^\dagger(\mathbf{x})c(\mathbf{x})p^\dagger(\mathbf{y})p(\mathbf{y}) \Big|_{y_0=x_0}, \quad (143)$$

where Q_c is the charge of the core, \mathbf{q} is the three-momentum transfer, and c (p) denote core (proton) fields, respectively. The full interaction between the proton and the core then consists of the long-range Coulomb photon exchange and the short-range strong interactions. In Halo EFT, the latter are represented by contact interactions while the Coulomb interaction must be treated explicitly. A central issue is the relative importance of these contributions, which is characterized by the Sommerfeld parameter $\eta = k_C/p$, where $k_C = Q_c \alpha_{em} \mu$ is the Coulomb momentum scale, with μ the reduced mass of the system and p a typical momentum of order M_{halo} . Thus, at low energies $\eta \gtrsim 1$ and Coulomb becomes non-perturbative. At sufficiently high (binding) energy, however, Coulomb can be included in perturbation theory. We will discuss several examples below.

The Coulomb interaction was first included in the framework of pionless EFT by Kong and Ravnal for the case $\eta \gtrsim 1$ [204, 205]. They calculated low-energy proton-proton scattering in an effective field theory with four-proton contact interactions. Here, we focus on halo nuclei and use a dimer formalism following the discussion in Refs. [206, 207]. We will also consider the case $\eta \gtrsim 1$.



Figure 21. Integral equation for the full halo propagator (thick line). The double solid/dashed line denotes the bare halo propagator, the dashed single line denotes the core field, the solid single line denotes the proton field and the shaded blob the Coulomb four-point function χ defined in Fig. 22.



Figure 22. The four-point function χ defined iteratively. The wiggly line denotes a Coulomb photon exchange. External propagators are amputated. Otherwise, the notation is as in Fig. 21.

We start with s-wave interactions and later discuss the extension to p-waves. The Lagrangians for the strong proton-core and proton-proton interactions are as in Eqs. (11, 12), with n replaced by p , respectively. Similarly, the propagators for c and p are obtained from Eq. (14). For convenience, we will also define the noninteracting proton-core Green's function in the center-of-mass frame,

$$iG_0(E, \mathbf{p}) = \frac{i}{E - \mathbf{p}^2/(2\mu_\sigma) + i\epsilon}, \quad (144)$$

where μ_σ denotes the reduced mass of the proton-core system which is represented by the σ field. Analogously, the proton-proton system is represented by the d field.

In the dimer propagators for the σ and d fields, the Coulomb interaction has to be included. Since we only consider one-proton halos, we discuss the σ propagator in detail. The d propagator, which is relevant for the proton-proton system and for two-proton halos, can be obtained analogously.

The proton-core propagator at rest is given by

$$iD_\sigma^{(bare)}(E, \mathbf{0}) \equiv iD_\sigma^{(bare)}(E) = \frac{i}{\Delta_\sigma + w_\sigma(E + i\epsilon)}. \quad (145)$$

The corresponding propagator for finite momentum \mathbf{p} can always be obtained by replacing $E \rightarrow E - \mathbf{p}^2/(2M_\sigma)$. The power counting for large scattering length requires that the s-wave interaction is summed up to all orders [208, 72, 73]. The resulting full σ propagator is thus given by the integral equation shown in Fig. 21. For a σ field at rest, we obtain

$$iD_\sigma(E) = \frac{i}{\Delta_\sigma + w_\sigma(E + i\epsilon) - \Sigma(E)}. \quad (146)$$

The irreducible self-energy, Σ , now includes strong and Coulomb interactions and will be discussed below.

We include the Coulomb interaction between the core and the valence proton through the full Coulomb Green's function,

$$\langle \mathbf{k} | G_C(E) | \mathbf{p} \rangle = -G_0(E, \mathbf{k}) \chi(\mathbf{k}, \mathbf{p}; E) G_0(E, \mathbf{p}), \quad (147)$$

where \mathbf{p} and \mathbf{k} are the relative incoming and outgoing momenta and E is the energy. The momentum-space Coulomb four-point function χ in the center-of-mass frame of the proton and the core is given by the integral equation depicted in Fig. 22. To distinguish coordinate-space from momentum-space states we denote the former with round brackets, i.e., $|\mathbf{r}\rangle$. The Coulomb Green's function can be expressed via its spectral representation in coordinate space

$$\langle \mathbf{r} | G_C(E) | \mathbf{r}' \rangle = \int \frac{d^3p}{(2\pi)^3} \frac{\psi_{\mathbf{p}}(\mathbf{r}) \psi_{\mathbf{p}}^*(\mathbf{r}')}{E - \mathbf{p}^2 / (2\mu_\sigma) + i\epsilon}, \quad (148)$$

where the Coulomb wave function $\psi_{\mathbf{p}}(\mathbf{r})$ is the solution of the Schrödinger equation for a Coulomb potential. We express $\psi_{\mathbf{p}}(\mathbf{r})$ through its partial wave expansion

$$\psi_{\mathbf{p}}(\mathbf{r}) = \sum_{l=0}^{\infty} (2l+1) i^l \exp(i\sigma_l) \frac{F_l(\eta, \rho)}{\rho} P_l(\hat{\mathbf{p}} \cdot \hat{\mathbf{r}}), \quad (149)$$

where $\rho = pr$ and $\eta = k_C/p$ is the Sommerfeld parameter. We have also introduced the pure Coulomb phase shift $\sigma_l = \arg \Gamma(l+1+i\eta)$. For the Coulomb functions F_l and G_l , we use the conventions of Ref. [209]. The regular Coulomb function F_l can be expressed in terms of the Whittaker M-function according to

$$F_l(\eta, \rho) = A_l(\eta) M_{i\eta, l+1/2}(2i\rho), \quad (150)$$

with

$$A_l(\eta) = \frac{|\Gamma(l+1+i\eta)| \exp[-\pi\eta/2 - i(l+1)\pi/2]}{2(2l+1)!}. \quad (151)$$

We will also need the irregular Coulomb wave function, G_l , which is given by

$$G_l(\eta, \rho) = iF_l(\eta, \rho) + B_l(\eta) W_{i\eta, l+1/2}(2i\rho), \quad (152)$$

where W is the Whittaker W-function and the coefficient B_l is defined as

$$B_l(\eta) = \frac{\exp(\pi\eta/2 + i\pi/2)}{\exp(i \arg \Gamma(l+1+i\eta))}. \quad (153)$$

Finally, the absolute value and the argument of the Γ -function are given by

$$|\Gamma(l+1+i\eta)| = \sqrt{\Gamma(l+1+i\eta)\Gamma(l+1-i\eta)} \quad (154)$$

and

$$\exp(i \arg \Gamma(l+1+i\eta)) = \sqrt{\frac{\Gamma(l+1+i\eta)}{\Gamma(l+1-i\eta)}}. \quad (155)$$

To obtain the full σ propagator D_σ , which includes strong and Coulomb interactions, we calculate the irreducible self-energy shown in Fig. 23. Using Eq. (147), it can be expressed as

$$-i\Sigma(E) = -ig_\sigma^2 \int \frac{d^3k_1 d^3k_2}{(2\pi)^6} \langle \mathbf{k}_2 | G_C(E) | \mathbf{k}_1 \rangle, \quad (156)$$

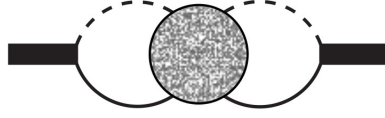


Figure 23. Feynman diagram for the irreducible self energy. The injected four-momentum is $(E, \mathbf{0})$. External legs are amputated. Otherwise, the notation is as in Fig. 21.

which can be written in coordinate space using Fourier transformations:

$$\begin{aligned}\Sigma(E) &= g_\sigma^2 \langle 0 | G_C(E) | 0 \rangle \\ &= g_\sigma^2 \left(\frac{\Lambda}{2} \right)^{4-D} \int \frac{d^{D-1}p}{(2\pi)^{D-1}} \frac{\psi_{\mathbf{p}}(0) \psi_{\mathbf{p}}^*(0)}{E - \mathbf{p}^2 / (2\mu_\sigma) + i\epsilon},\end{aligned}\quad (157)$$

where we have continued the last integral to $D - 1$ spatial dimensions, and introduced the renormalization scale Λ to maintain the correct dimensionality of $\Sigma(E)$. Evaluating this integral using dimensional regularization, we obtain [205]

$$\Sigma(E) = -g_\sigma^2 \frac{k_C \mu_\sigma}{\pi} H(\eta) - \Sigma^{div}, \quad (158)$$

with

$$H(\eta) = \psi(i\eta) + \frac{1}{2i\eta} - \log(i\eta), \quad (159)$$

where $\psi(z) = \Gamma'(z)/\Gamma(z)$ is the logarithmic derivative of the Gamma function and $\eta = k_C/k$. In the strong Coulomb regime with $\eta \gtrsim 1$, the function $H(\eta)$ can be expanded as

$$H(\eta) = \frac{1}{12\eta^2} + \frac{1}{120\eta^4} + \dots + \frac{i\pi}{e^{2\pi\eta} - 1}, \quad (160)$$

leading to a simplified treatment of the Coulomb interaction [210]. Note that $H(\eta)$ has nothing to do with the three-body force $H(\Lambda)$ that appeared earlier. The difference between the two functions is obvious from the context.

Using PDS [72, 73], the divergent part of Σ is given by

$$\Sigma^{div} = -\frac{g_\sigma^2 k_C \mu_\sigma}{\pi} \left[\frac{1}{3-D} + \log\left(\frac{\sqrt{\pi}\Lambda}{2k_C}\right) + 1 - \frac{3C_E}{2} \right] + \frac{g_\sigma^2 \mu_\sigma \Lambda}{2\pi}, \quad (161)$$

where $C_E = 0.5772$ is Euler's constant. Note that Σ^{div} is independent of energy and therefore will vanish when we take the energy derivative of the irreducible self-energy to arrive at the LSZ residue below. Moreover, Eq. (161) absorbs two divergences into a single parameter: the linear dependence on Λ from the PDS scheme and a logarithmic term in Λ from the one photon exchange. An alternative scheme for the perturbative case $\eta \ll 1$ that isolates the linear and logarithmic divergences has been suggested in Ref. [211].

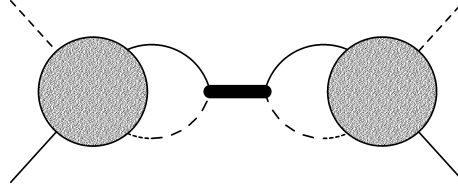


Figure 24. Scattering amplitude, t_{CS} , for elastic proton-core scattering. The notation is as in Fig. 21.

5.2. Renormalization

Expressions for EFT low-energy constants such as g_σ and Δ_σ defined above are frequently obtained by matching them to elastic scattering observables. The full amplitude for elastic proton-core scattering consists of two parts: the amplitude for pure Coulomb scattering t_C and the Coulomb-modified strong scattering amplitude t_{CS} . The former is essentially given by the four-point function χ depicted in Fig. 22. For matching to the Coulomb-modified effective range expansion only the latter amplitude t_{CS} is required. The amplitude t_{CS} is obtained from the diagram in Fig. 24 and evaluates to

$$it_{0,\sigma}(E) = ig_\sigma^2 \exp(2i\sigma_0) C_\eta^2 D_\sigma(E) , \quad (162)$$

with the Gamow-Sommerfeld factor $C_\eta^2 = \Gamma(1+i\eta)\Gamma(1-i\eta)$. The index CS has been dropped for convenience.

In the absence of the Coulomb interaction, the t-matrix is usually expressed in terms of effective range parameters. However, it is not possible to separate the strong interaction from the Coulomb interaction in a model-independent way [204, 205]. Therefore one uses the so-called Coulomb-modified effective range expansion [212] to relate the phase shifts to redefined effective range parameters. The t-matrix is then written

$$t_{0,\sigma}(E) = -\frac{2\pi}{\mu_\sigma} \frac{C_\eta^2 \exp(2i\sigma_0)}{k C_\eta^2 (\cot \delta_0 - i)} , \quad (163)$$

where the total phase shift is given by $\sigma_0 + \delta_0$. The s-wave Coulomb-modified ERE is

$$k C_\eta^2 (\cot \delta_0 - i) + 2k_C H(\eta) = -\frac{1}{a_{0,\sigma}^C} + \frac{1}{2} r_{0,\sigma}^C k^2 + \dots , \quad (164)$$

where $a_{0,\sigma}^C$ and $r_{0,\sigma}^C$ are the Coulomb-modified scattering length and effective range, respectively. In Eq. (164), the imaginary part of $2k_C H(\eta)$ exactly cancels $-ik C_\eta^2$, leaving an analytic, real function of k^2 .

Comparing Eqs. (162) and (163), order by order in the momentum k , we can express the Coulomb-modified scattering length and effective range in terms of the low-energy coupling constants g_σ and Δ_σ

$$\frac{1}{a_{0,\sigma}^C} = \frac{2\pi}{g_\sigma^2 \mu_\sigma} (\Delta_\sigma + \Sigma^{\text{div}}) , \quad (165)$$

$$r_{0,\sigma}^C = -\frac{2\pi w_\sigma}{g_\sigma^2 \mu_\sigma^2} . \quad (166)$$

These equations are the equivalent of Eqs. (19a), (19b) in the presence of Coulomb interactions. Equation (165) shows how the low-energy constant Δ_σ absorbs the divergent part of the irreducible self-energy Σ^{div} . Note that here and below LO results can be obtained by setting $w_\sigma = 0$. When this is done results in the EFT depend only on the combination Δ_σ/g_σ^2 .

The residue at the bound state, $E = -B$, of the full σ propagator defines the wave-function renormalization, which is required for the calculation of bound-state observables. Note that we keep the formalism general here. In our application to proton halos below, B is to be identified with the one-proton separation energy, S_{1p} . Using Eq. (23) and the matching condition Eq. (166), we obtain

$$Z_\sigma = \frac{1}{w_\sigma - \Sigma'(-B)} = \frac{6\pi k_C}{g_\sigma^2 \mu_\sigma^2} \frac{-1}{\tilde{H}(\gamma, k_C) - 3k_C r_{0,\sigma}^C}, \quad (167)$$

In writing Eq. (167), we have defined the function

$$\tilde{H}(\gamma, k_C) = \frac{6k_C^2}{\mu_\sigma} \frac{d}{dE} H(\eta) \Big|_{E=-B}, \quad (168)$$

with the binding momentum $\gamma = \sqrt{2\mu_\sigma B}$. The expression Eq. (167) is valid at next-to-leading order (NLO), since it includes the effective-range correction. The corresponding expression at leading order (LO) is obtained by setting $r_{0,\sigma}^C$ to zero in Eq. (167).

If the ratio between the binding momentum and Coulomb momentum γ/k_C is small, we can use the expansion in Eq. (160) to obtain

$$\tilde{H}(\gamma, k_C) = 1 - \frac{\gamma^2}{5k_C^2} + \frac{\gamma^4}{7k_C^4} + \dots \quad (169)$$

Thus, for systems where the separation $\gamma \ll k_C$ is fulfilled we can use $\tilde{H}(\gamma, k_C) \rightarrow 1$ in all expressions [210].

The residue Z_σ can be related to the asymptotic normalization coefficient (ANC), C_σ , or to experimental radiative capture data. The ANC is defined as the coefficient in the asymptotic bound state wavefunction

$$w_l(r) = C_\sigma W_{-i\eta, l+1/2}(2\gamma r), \quad (170)$$

where W is the Whittaker-W function. The Z -factor is related to the ANC according to

$$Z_\sigma = \frac{-\pi}{g_\sigma^2 \mu_\sigma^2 [\Gamma(1 + k_C/\gamma)]^2} C_\sigma^2. \quad (171)$$

At LO, the wave-function renormalization is determined solely by γ and k_C , as can be seen in Eq. (167) with $r_{0,\sigma}^C = 0$, and as such the ANC is predicted to LO accuracy as

$$C_{\sigma,LO} = \sqrt{\frac{6k_C}{\tilde{H}(\gamma, k_C)}} \Gamma(1 + k_C/\gamma). \quad (172)$$

At NLO, $r_{0,\sigma}^C$ contributes as well. It is advantageous to use the z -parametrization and fix Z_σ directly from the ANC. For this purpose, it is useful to define the NLO

wavefunction renormalization in terms of the matching to the ANC, Eq. (171). The ratio to the LO residue is then obtained as

$$\frac{Z_\sigma}{Z_{\sigma,LO}} = \frac{C_\sigma^2}{C_{\sigma,LO}^2}. \quad (173)$$

It is important to note that Z_σ and the ANC receive contributions from all ERE parameters. As such the expression (167) is only valid at NLO. However, the matching (171) itself is valid at any order in the power counting and there is no EFT error due to the non-inclusion of higher-order contact interactions.

For completeness, we also provide expressions for the effective range and the scattering length in the z -parameterization, up to corrections due to higher-order ERE parameters. For a given one-proton separation energy $B = \gamma^2/(2\mu_\sigma)$, the ANC determines the Coulomb-modified effective range

$$r_{0,\sigma}^C = \frac{\tilde{H}(\gamma, k_C)}{3k_C} - \frac{2[\Gamma(1 + k_C/\gamma)]^2}{C_\sigma^2} \quad (174)$$

combining Eqs. (167) and (171). The Coulomb-modified scattering length is then obtained from the pole position of the t-matrix (163), that is

$$a_{0,\sigma}^C = -\frac{2}{4k_C H(-ik_C/\gamma) + \gamma^2 r_{0,\sigma}^C}. \quad (175)$$

These s-wave effective-range-expansion results are accurate up to corrections due to the shape parameter in the ERE. It is therefore important to note that, if the ERE parameters are to be extracted to high accuracy from the ANC, one would need to derive the expressions (174) and (175) to higher orders. Vice versa, if the ANC is to be predicted accurately from elastic scattering data, then the expression (167) needs to be improved by including dependencies of additional ERE parameters.

5.3. Applications to Scattering

Kong and Ravndal first included Coulomb interactions in the pionless effective field theory using the PDS regularization scheme [204, 205]. They considered proton-proton scattering near threshold where the Coulomb interaction is strong and needs to be included nonperturbatively at leading order. In particular, they showed that the extraction of a strong proton-proton scattering length a_{pp} from the standard Coulomb-modified scattering length a_{pp}^C is scheme-dependent and depends on the renormalization scale Λ

$$\frac{1}{a_{pp}(\Lambda)} = \frac{1}{a_{pp}^C} + \alpha_{em} m_n \left[\log \left(\frac{\sqrt{\pi} \Lambda}{\alpha_{em} m_n} \right) + 1 - \frac{3C_E}{2} \right], \quad (176)$$

since the short-distance parts of the Coulomb and strong interactions cannot be uniquely separated. The effective range, however, remains unaffected by Coulomb interactions. Complementary renormalization group treatments of the pp system can be found in Refs. [213, 214]. An application to proton- α scattering is discussed in [215]. The same power counting also applies to the excited $1/2^+$ state of ^{17}F . Using the

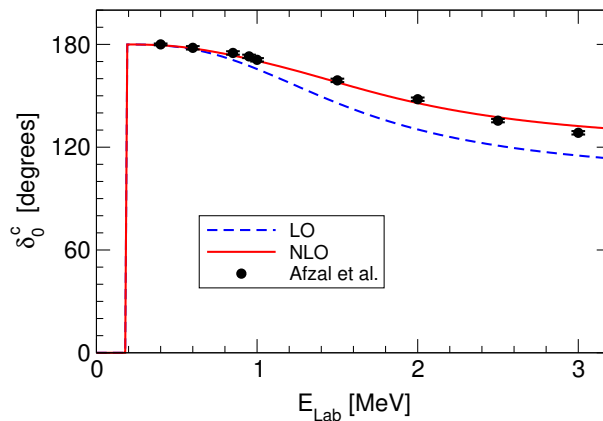


Figure 25. The $\alpha\alpha$ s -wave phase shift δ_0^c as a function of the laboratory energy E_{Lab} . The EFT results in LO and NLO from Ref. [210] are given by the (blue) dashed and (red) solid lines, respectively. The experimental phase shifts are shown as (black) solid circles with error bars [217].

formalism described above, Ryberg and collaborators calculated the electric radius and the astrophysical S-factor for low-energy proton capture [206, 207]. They also provided a general discussion of the suppression of proton halos compared to neutron halos by the need for two fine tunings in the underlying theory.

This treatment of Coulomb, however, is not appropriate for all weakly-bound systems in which Coulomb interactions are present. An example is given by the $\alpha - \alpha$ system at low energies which is highly fine tuned [210]. Due to the delicate interplay between attraction from the strong interaction and the Coulomb repulsion, there is a narrow resonance at an energy of about 0.1 MeV in this system. The scenario of Ref. [210] can be viewed as an expansion around the limit where, when electromagnetic interactions are turned off, the ${}^8\text{Be}$ ground state is at threshold and exhibits conformal invariance. This implies treating the Coulomb momentum k_C as a high-momentum scale and expanding observables in k/k_C , using the expansion in Eq. (160) such that the inverse of the amplitude t_{CS} becomes proportional to

$$-\frac{1}{a_{0,\sigma}^C} + r_{0,\sigma}^C k^2/2 - 2k_C H(\eta) + \dots \quad (177)$$

The corresponding phase shifts are shown in Fig. 25. When Coulomb interactions are turned off, the third term of Eq. (177) becomes the usual unitarity term ik . Since $a_{0,\sigma}^C \sim M_{\text{core}}/M_{\text{halo}}^2$ and $r_{0,\sigma}^C \sim M_{\text{core}}^{-1}$, the first two terms are subleading corrections for momenta $k \sim M_{\text{halo}}$ and only the unitarity term remains at leading order. Therefore, at leading order the ${}^8\text{Be}$ system shows conformal invariance, and the corresponding 3-body system ${}^{12}\text{C}$ acquires an exact Efimov spectrum [26]. This is a possible realization of the unitary limit. When Coulomb is restored, the Coulomb potential breaks scale invariance and the three terms in Eq. (177) are of comparable size. However, the fact that the ${}^8\text{Be}$ ground state stays close to threshold can be seen as a remnant of the now broken conformal symmetry. This scenario provides a possible realization of the

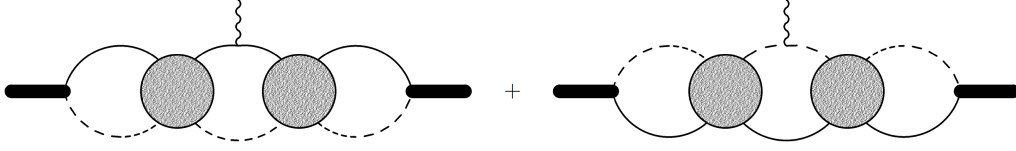


Figure 26. The diagrams contributing to the charge form factor at LO. The notation is as in Fig. 21.

conjecture that the Hoyle state in ^{12}C could be considered an approximate Efimov state of α particles [26]. The properties of this state will be modified by the long-range Coulomb interaction once it is restored [216].

5.4. Form Factors

We now move on to a calculation of the electric form factor of an s-wave proton halo to NLO. At LO there are two loop diagrams, $\Gamma_{\text{LO}}(|\mathbf{q}|)$, and at NLO a constant tree-level diagram, Γ_{NLO} , enters. We derive and evaluate these diagrams below. The electric form factor is then given by the sum of diagrams

$$F_E^{(\sigma)}(|\mathbf{q}|) = \frac{Z_\sigma}{e(Q_c + 1)} [\Gamma_{\text{LO}}(|\mathbf{q}|) + \Gamma_{\text{NLO}}(|\mathbf{q}|) + \dots] . \quad (178)$$

5.4.1. Leading order At leading order, we have to consider the diagrams shown in Fig. 26. In contrast to neutron halos, the photon couples to both single-particle lines through the operator $\psi^\dagger A_0 \psi$ where ψ can be a proton field p or a core field c . We choose incoming and outgoing total four-momenta as $(E, -\mathbf{q}/2)$ and $(E, \mathbf{q}/2)$, respectively, where $E = -B + |\mathbf{q}|^2/(8M_\sigma)$. After carrying out the integrals over the zero component of the loop momenta the resulting amplitude can be simplified using the Coulomb Green's function in Eq. (147). This leads to

$$i\Gamma_{\text{LO}}(|\mathbf{q}|) = ig_\sigma^2 e Q_c \int \frac{d^3 k_1 d^3 k_2 d^3 k_3}{(2\pi)^9} \langle \mathbf{k}_3 | G_C(-B) | \mathbf{k}_2 - f\mathbf{q}/2 \rangle \\ \times \langle \mathbf{k}_2 + f\mathbf{q}/2 | G_C(-B) | \mathbf{k}_1 \rangle + [(f \rightarrow 1 - f), (Q_c \rightarrow 1)] , \quad (179)$$

where $f = m_n/M_\sigma = 1/(A + 1)$. Fourier transforming each of the momentum-space bras and kets, we arrive at the coordinate-space integral

$$i\Gamma_{\text{LO}}(|\mathbf{q}|) = ig_\sigma^2 e Q_c \int \frac{d^3 r}{(2\pi)^3} \langle 0 | G_C(-B) | \mathbf{r} \rangle \exp(i f \mathbf{q} \cdot \mathbf{r}) \langle \mathbf{r} | G_C(-B) | 0 \rangle \\ + [(f \rightarrow 1 - f), (Q_c \rightarrow 1)] , \quad (180)$$

which is much more convenient to use. In Eq. (180), the diagram in Fig. 26 is also better visualized. It consists of two Coulomb Green's functions, that propagate the fields from separation zero to \mathbf{r} and back from separation \mathbf{r} to zero, respectively, and the current operator in between the propagators. Since the Coulomb Green's functions have one end

at zero separation, only their s-wave part will contribute. We thus expand the Coulomb Green's function in partial waves

$$\langle \mathbf{r}' | G_C(E) | \mathbf{r} \rangle = \sum_{l=0}^{\infty} (2l+1) G_C^{(l)}(E; r', r) P_l(\hat{\mathbf{r}}' \cdot \hat{\mathbf{r}}). \quad (181)$$

and obtain [207]

$$\langle 0 | G_C(-B) | \mathbf{r} \rangle = G_C^{(0)}(-B; 0, r) = -\frac{\mu_\sigma \Gamma(1 + k_C/\gamma)}{2\pi} \frac{W_{-k_C/\gamma, 1/2}(2\gamma r)}{r}. \quad (182)$$

The integral (180) can now be written as

$$i\Gamma_{LO}(|\mathbf{q}|) = i \frac{g_\sigma^2 e Q_c \mu_\sigma^2}{8\pi^4} [\Gamma(1 + k_C/\gamma)]^2 \int dr j_0(fr|\mathbf{q}|) [W_{-k_C/\gamma, 1/2}(2\gamma r)]^2 + [(f \rightarrow 1-f), (Q_c \rightarrow 1)], \quad (183)$$

which can be evaluated numerically. The charge form factor is given by Eq. (178) and the LO electric radius is obtained in terms of the loop-integral $\Gamma_{LO}(|\mathbf{q}|)$ and the wavefunction renormalization Z_{LO} :

$$\langle r_E^2 \rangle_{\text{pt}, LO}^{(\sigma)} = -\frac{3Z_{\sigma, LO}}{e(Q_c + 1)} \frac{d^2}{d|\mathbf{q}|^2} \Gamma_{LO}(|\mathbf{q}|) \Big|_{|\mathbf{q}|=0}. \quad (184)$$

We go on to demonstrate that the electric form factor is normalized correctly to 1 at $|\mathbf{q}| = 0$. Starting from the coordinate-space integral (180) at $|\mathbf{q}| = 0$ and the spectral representation of the Coulomb Green's function

$$\langle 0 | G_C(E) | \mathbf{r} \rangle = \int \frac{d^3p}{(2\pi)^3} \frac{\psi_{\mathbf{p}}(0) \psi_{\mathbf{p}}^*(\mathbf{r})}{E - \mathbf{p}^2/(2\mu_\sigma) + i\varepsilon}, \quad (185)$$

we find that

$$\begin{aligned} \Gamma_{LO}(0) &= g_\sigma^2 e (Q_c + 1) \int d^3r |\langle 0 | G_C(-B) | r \rangle|^2 \\ &= g_\sigma^2 e (Q_c + 1) \int \frac{d^3p}{(2\pi)^3} \frac{\psi_{\mathbf{p}}(0) \psi_{\mathbf{p}}^*(0)}{(-B - \mathbf{p}^2/(2\mu_\sigma))^2} \\ &= -e(Q_c + 1) \Sigma'(-B). \end{aligned} \quad (186)$$

In the first step above the orthonormality of the Coulomb wavefunctions was used. The correct normalization of the LO electric form factor now follows from combining Eqs. (178), (186) and (167).

5.4.2. Next-to-leading order At NLO the full LSZ residue Z_σ from Eq. (171) must be used instead of $Z_{\sigma, LO}$ and the NLO operator $\sigma^\dagger A_0 \sigma$ enters through the right diagram in Fig. 17. Its contribution is given by the Feynman rule for an A_0 photon coupling to the σ field

$$i\Gamma_{NLO} = -iw_\sigma e(Q_c + 1). \quad (187)$$

Thus the NLO correction (187) is independent of the momentum transfer $|\mathbf{q}|$.

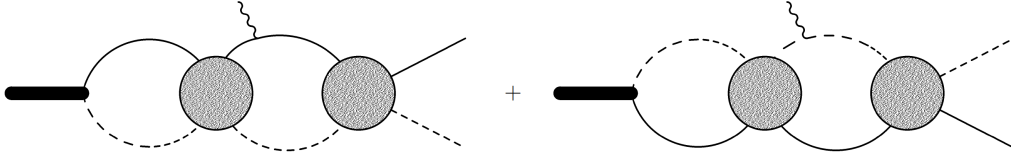


Figure 27. The diagrams for radiative capture at LO. The notation is as in Fig. 21 and time flows from right to left.

The NLO electric form factor is given by the sum of the diagrams up to NLO, according to Eq. (178). Using Eqs. (186), (167), and (187), as well as the formula (178) it is clear that the electric form factor at $|\mathbf{q}| = 0$ is still normalized to unity. The electric radius is then given by the order $|\mathbf{q}|^2$ part of the LO loop-integral (183) together with the full wavefunction renormalization (171). The resulting electric radius is

$$\langle r_E^2 \rangle_{\text{pt},NLO}^{(\sigma)} = -\frac{3Z_\sigma}{e(Q_c + 1)} \left. \frac{d^2}{d|\mathbf{q}|^2} \Gamma_{LO}(|\mathbf{q}|) \right|_{|\mathbf{q}|=0}. \quad (188)$$

The NLO electric radius (188) is different from the LO result by a factor $Z_\sigma/Z_{\sigma,LO} = C_\sigma^2/C_{\sigma,LO}^2$ (cf. Eq. (173)) which is proportional to the square of the ANC.

At higher orders there are various types of corrections. Firstly, there are local short-range operators $\psi^\dagger [\nabla^2 A_0 - \partial_0(\nabla \cdot \mathbf{A})] \psi$ ($\psi = c, p$), which enter with finite-size contributions of the core and proton fields. Similar to what was done in Sec. 4, these higher-order finite-size contributions can be added in a straightforward way, yielding

$$\langle r_E^2 \rangle = \langle r_E^2 \rangle_{\text{pt}} + \frac{Q_c}{Q_c + 1} \langle r_E^2 \rangle_c + \frac{1}{Q_c + 1} \langle r_E^2 \rangle_p. \quad (189)$$

Secondly, there is a local short-range operator $\sigma^\dagger [\nabla^2 A_0 - \partial_0(\nabla \cdot \mathbf{A})] \sigma$, that comes in with an undetermined short-range parameter.

5.5. Radiative Capture

In this subsection we consider radiative E1 capture of a proton into a halo state including range corrections. Specifically, we assume a spin zero core and capture of the proton into an s-wave state with $J^P = 1/2^+$, which requires the incoming particle pair to have relative angular momentum $l \geq 1$. These quantum numbers are relevant for the capture process $^{16}\text{O}(p, \gamma)^{17}\text{F}^*$, which will be discussed as an application below.

We present our results in terms of the astrophysical S-factor, which is defined as

$$S(E) = E \exp(2\pi\eta) \sigma_{\text{tot}}(E), \quad (190)$$

with the incoming center-of-mass energy E and the total cross section σ_{tot} . This removes the otherwise dominant exponential suppression of the capture cross section at energies below the Coulomb barrier.

5.5.1. Leading order At leading order, we only need to consider diagrams where the photon couples to one of the single-particle lines, that is through the operator

$ie\psi^\dagger \hat{\mathbf{Q}} \mathbf{A} \cdot \nabla \psi/m$ ($\psi = c, p$). All diagrams which have the incoming particle pair in a relative s-wave vanish because we are considering E1 capture which changes the angular momentum by one unit. Since the p-wave dominates at low energies, we neglect all partial waves with $l \geq 2$. The two radiative capture diagrams of interest are shown in Fig. 27. These diagrams are to be read from the right to the left, that is with the incoming proton-core pair on the right-hand side and the outgoing bound state to the left. We will write them using the pure Coulomb t-matrix T_C [218]. The four-point function χ defined in Fig. 22 is directly proportional to the Coulomb Green's function G_C and receives contributions from the Coulomb t-matrix T_C as well as from the free propagation of the core-proton system (cf. Fig. 22). In the center-of-mass of the halo and the radiated photon, the momentum-space diagrams from Fig. 27 become

$$i\mathcal{M} = -ig_\sigma \sqrt{Z_{\sigma,LO}} \frac{eQ_c f}{\mu_\sigma} \int \frac{d^3k_1 d^3k_2}{(2\pi)^6} G_0(-B, \mathbf{k}_2 + f\mathbf{q}) \chi(\mathbf{k}_2 + f\mathbf{q}, \mathbf{k}_1 + f\mathbf{q}, -B) \\ \times G_0(-B, \mathbf{k}_1 + f\mathbf{q}) \mathbf{k}_1 \left[\delta^3(\mathbf{p} - \mathbf{k}_1) + [E - \mathbf{k}_1^2/(2\mu_\sigma)]^{-1} T_C(\mathbf{k}_1, \mathbf{p}) \right] \\ - [(f \rightarrow 1 - f), (Q_c \rightarrow 1)]. \quad (191)$$

where we have separated the contributions from the Coulomb t-matrix T_C and the free propagation of the core-proton system in the initial state. In the final state, we use the Coulomb four-point function χ as before. The total energy flowing through the diagram is $E = -B + \omega + \omega^2/(2M_\sigma) = \mathbf{p}^2/(2\mu_\sigma)$.

Then, using the relation [218]

$$\psi_{\mathbf{p}}(\mathbf{k}_1) = \delta^3(\mathbf{k}_1 - \mathbf{p}) + [E - \mathbf{k}_1^2/(2\mu_\sigma)]^{-1} T_C(\mathbf{k}_1, \mathbf{p}) \quad (192)$$

for the Coulomb wave function and replacing the four-point function χ with Eq. (147) the integral (191) can be expressed as:

$$i\mathcal{M} = -ig_\sigma \sqrt{Z_{\sigma,LO}} \frac{eQ_c f}{\mu_\sigma} \int \frac{d^3k_1 d^3k_2}{(2\pi)^6} \langle \mathbf{k}_2 | G_C(-B) | \mathbf{k}_1 + f\mathbf{q} \rangle \mathbf{k}_1 \psi_{\mathbf{p}}(\mathbf{k}_1) \\ - [(f \rightarrow 1 - f), (Q_c \rightarrow 1)] \quad (193)$$

Performing Fourier transforms and using $\mathbf{k}_1 \exp(i\mathbf{k}_1 \cdot \mathbf{r}_2) = -i\nabla_2 \exp(i\mathbf{k}_1 \cdot \mathbf{r}_2)$ we can write the integral (193) as

$$i\mathcal{M} = g_\sigma \sqrt{Z_{\sigma,LO}} \frac{eQ_c f}{\mu_\sigma} \int d^3r G_C^{(0)}(-B; 0, r) \exp(-if\omega r \cos \theta) (\nabla \psi_{\mathbf{p}}(\mathbf{r})) \\ - [(f \rightarrow 1 - f), (Q_c \rightarrow 1)]. \quad (194)$$

Finally, summing over all polarizations and doing the angular integration, the amplitude squared in Eq. (194) evaluates to

$$\sum_i |\epsilon_i \cdot \mathcal{M}|^2 = \left| \sqrt{Z_{\sigma,LO}} \sin \theta (\cos \phi + \sin \phi) \frac{4\pi g_\sigma eQ_c f \exp(i\sigma_1)}{\mu_\sigma p} \right. \\ \left. \times \int dr G_C^{(0)}(-B; 0, r) j_0(f\omega r) \frac{\partial}{\partial r} [r F_1(k_C/p, pr)] - [(f \rightarrow 1 - f), (Q_c \rightarrow 1)] \right|^2 \quad (195)$$

This integral can be calculated numerically, using the s-wave projected Coulomb Green's function and the regular Coulomb wave function.

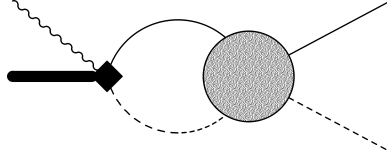


Figure 28. The capture diagram entering at N⁴LO. The notation is as in Fig. 21 and time flows from right to left. The diamond vertex corresponds to the short-range interaction of Eq. (97).

5.5.2. Next-to-leading order The higher-order ERE parameters appear with $\nabla + ie\hat{\mathbf{Q}}\mathbf{A}$ operators that, in principle, can give contributions to the radiative-capture amplitude. However, the diagrams with these higher-order ERE operators are diagrams with initial-wave scattering due to the strong force. Since we only have included the resonant s-wave part of the strong interaction these initial-wave scattering diagrams are identically zero, which can be understood from the fact that the E1 capture process changes the angular momentum by one. If we were to include also the non-resonant p-wave interaction explicitly in the field theory, then the effective range, the shape parameter, and so on, would contribute through diagrams with initial p-wave scattering. The physics of these diagrams is implicitly included in local short-range operators with growing powers of the photon energy ω . Such an operator is explicitly discussed below.

Consequently, there are no additional capture diagrams to consider at NLO. The only contribution at NLO is due to the change in the wavefunction renormalization. This leads to a constant factor

$$\frac{Z_\sigma}{Z_{\sigma,LO}} = \frac{C_\sigma^2}{C_{\sigma,LO}^2} = \frac{\tilde{H}(\gamma, k_C)}{\tilde{H}(\gamma, k_C) - 3k_C r_{0,\sigma}^C} \quad (196)$$

difference compared to the LO result. It is important to note that if $r_{0,\sigma}^C \approx \tilde{H}(\gamma, k_C)/(3k_C)$, or equivalently if the ANC C_σ is very large, then the NLO correction will be large, too. We discuss this case in more detail in Sec. 5.6.

5.5.3. Higher Orders At N⁴LO the short-range E1 operator from Eq. (97) appears. This short-range interaction is simply a contact vertex, where the incoming proton-core pair is in a relative p-wave. Note, that in the present case the $j = 1/2$ and $j = 3/2$ channels contribute. The operator (97) gives rise to the capture diagram in Fig. 28. The tree-level amplitude is given by

$$\mathcal{M} = D^{(E1)} \sqrt{Z_\sigma \omega} \exp(i\sigma_1) \mathbf{p} \sqrt{(1 + \eta^2) C_\eta^2}. \quad (197)$$

The derivation of the amplitude (197) involves the evaluation of the p-wave integral $\int \frac{d^3k}{(2\pi)^3} \mathbf{k} \psi_{\mathbf{p}}(\mathbf{k}) = -\exp(i\sigma_1) \mathbf{p} \sqrt{(1 + \eta^2) C_\eta^2}$, where σ_1 is the pure Coulomb phase shift in the p-wave. The symbol $D^{(E1)}$ has been introduced as a compact notation for the total constant of proportionality and includes both spin channels.

The next relevant operator includes an additional time derivative acting on the photon field and enters at N⁶LO and as such this calculation is valid up to N⁵LO.

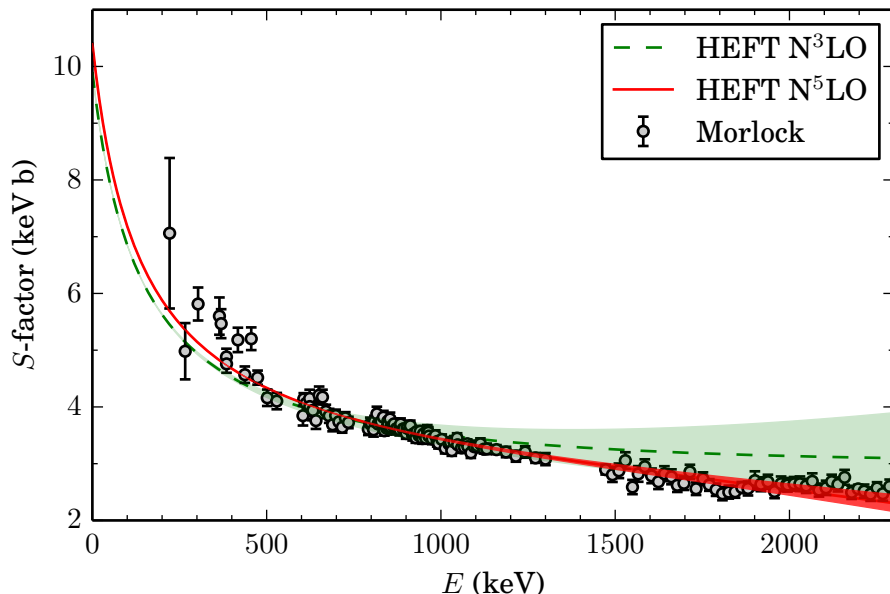


Figure 29. Energy dependent S-factor for $^{16}\text{O}(p, \gamma)^{17}\text{F}^*$ fitted to experimental data by Morlock *et al.* [219]. The error bands correspond to the model error from omitted terms at higher orders. See text for details. (Figure taken from Ref. [207].)

It should be noted that if the strong p-wave interaction is included explicitly into the field theory then there would also exist local non-minimal operators of the form [66] $\pi^\dagger(\partial_0 A_j - \nabla_j A_0)\pi$, where π is a p-wave dicluster field (the spin indices on the dicluster fields have been suppressed). If the p-wave is enhanced this operator would appear already at NLO. However, as has already been mentioned, we have no reason to suspect that the p-wave interaction is enhanced. In the following application to $^{16}\text{O}(p, \gamma)^{17}\text{F}^*$, we will assume that it does not enter up to N⁵LO.

5.5.4. Application to $^{16}\text{O}(p, \gamma)^{17}\text{F}^$* In Ref. [207], this formalism was applied to the excited $1/2^+$ state of ^{17}F which is an s-wave halo state of the valence proton and the $^{16}\text{O}(0^+)$ core. Their results for the radiative proton capture reaction $^{16}\text{O}(p, \gamma)^{17}\text{F}^*$, together with data by Morlock *et al.* [219], are shown in Fig. 29. The green dashed line is the Halo EFT result valid up to N³LO. The single free parameter of the theory is the ANC which was fitted to the experimental data by Morlock *et al.* [219] by minimizing an objective function that takes into account experimental errors and theoretical errors from the truncation of the EFT expansion (See Ref. [207] for details). Taking energy-dependent EFT errors into account allowed them to include data up to a center-of-mass energy of 2.3 MeV. They determined the amplitude, C_{EFT} , of the EFT error which scale as $(p/M_{\text{core}})^4$ by the statistical guiding principle that the total χ^2 per degree of freedom should be unity.† The constant C_{EFT} is expected to be of natural size and is

† Note that the Morlock data has a normalization error of 10%, which was subtracted in quadrature from the total experimental error during the fitting procedure. This normalization error was added

determined iteratively such that the χ^2 per degree of freedom is minimized to unity. This systematical theory error at N³LO is shown as a green band in Fig. 29, with $C_{\text{EFT}} = 6.9$ and the breakdown scale given by $M_{\text{core}} = 76$ MeV. Although somewhat large, this value of C_{EFT} is still consistent with our power counting estimate.

Similarly, the red line is given by a fit of the N⁵LO result to the same data set where the systematic theory error estimate scales as $(p/M_{\text{core}})^6$. At this order we find $C_{\text{EFT}} = 1.9$ with $M_{\text{core}} = 76$ MeV. It is clearly seen that the result converges with increasing order of the EFT and that the S-factor value at threshold is stable. From these fits, they extracted a threshold S-factor

$$S(0) = \begin{cases} (9.9 \pm 0.1 \text{ (stat)} \pm 1.0 \text{ (norm)}) \text{ keV b} , \text{ N}^3\text{LO} \\ (10.4 \pm 0.1 \text{ (stat)} \pm 1.0 \text{ (norm)}) \text{ keV b} , \text{ N}^5\text{LO} \end{cases} \quad (198)$$

with the 1% error due to the EFT fit (mainly statistical error) and the 10% error from the uncertainty in the absolute normalization of the experimental data. These results give the ANC

$$C_\sigma = \begin{cases} (77.4 \pm 0.2 \text{ (stat)} \pm 3.8 \text{ (norm)}) \text{ fm}^{-1/2} , \text{ N}^3\text{LO} \\ (79.3 \pm 0.2 \text{ (stat)} \pm 3.9 \text{ (norm)}) \text{ fm}^{-1/2} , \text{ N}^5\text{LO} \end{cases} . \quad (199)$$

The ANC for this system has also been extracted by Huang et al. [220], using a single-particle model fit of radiative capture data, as $C_\sigma = 77.21 \text{ fm}^{-1/2}$ and experimentally by Gagliardi et al. [221], using the transfer reaction $^{16}\text{O}(^3\text{He}, d)^{17}\text{F}$, as $C_\sigma = (80.6 \pm 4.2) \text{ fm}^{-1/2}$. The ANCs are consistent with the values extracted using Halo EFT.

The electric radius of the $^{17}\text{F}^*$ can now be obtained by using the extracted ANC. Using the ^{16}O -proton ANC extracted from the N⁵LO radiative proton capture fit, the resulting NLO electric radius is given by

$$\sqrt{\langle r_E^2 \rangle_{\text{NLO}}^{(\sigma)}} = (2.20 \pm 0.04 \text{ (EFT)} \pm 0.11 \text{ (ANC)}) \text{ fm} . \quad (200)$$

The NLO EFT error in Eq. (200) was estimated from the EFT expansion parameter squared, $(\gamma/M_{\text{core}})^2$, using a breakdown scale $M_{\text{core}} = 76$ MeV. The dominant error in Eq. (200) is from the normalization error of the Morlock data, through the extracted ANC. However, there could also be additional EFT errors for this result due to the non-inclusion of the operators that are responsible for the finite-size contributions of the constituents [222]. Alternatively, the result (200) can be interpreted as the radius relative to the ^{16}O core.

5.6. Fine tuning in s-wave proton halos

Along the neutron drip-line there exist several neutron halo states. These states are characterized by an unnaturally large neutron-core scattering length, which brings the state very close to threshold. However, proton halos are much more rare. In the s-wave back after the fit had been performed.

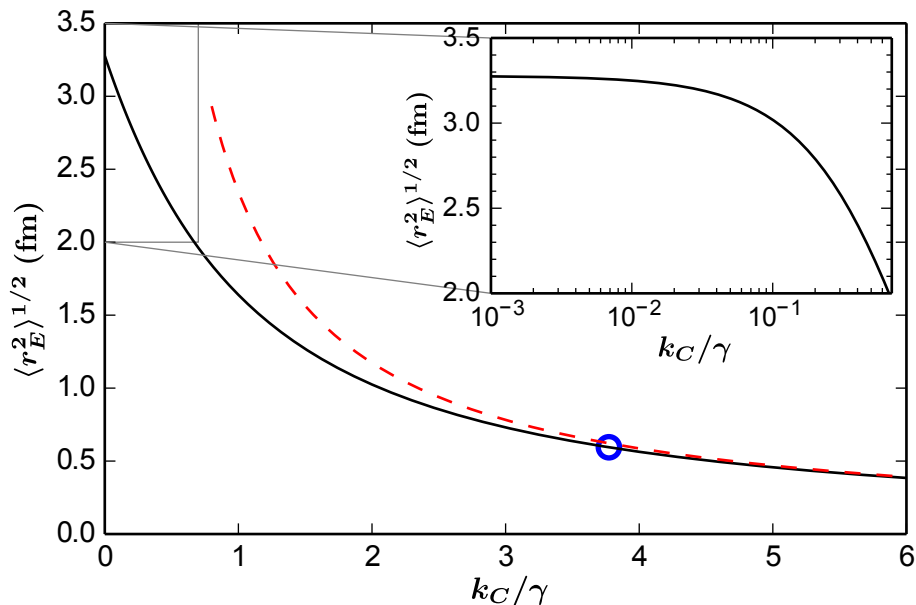


Figure 30. The dependence of the LO electric radius on k_C/γ . The solid black line is the LO Halo EFT result, the blue circle denotes the $^{17}\text{F}^*$ system, and the dashed red line is the asymptotic $1/k_C$ behavior. The inset shows the low-energy region in a semi-logarithmic scale, illustrating the hypothetical neutron halo limit (201). The curve was generated using a binding momentum $\gamma = 13.6$ MeV. (Figure taken from Ref. [207].)

case this can be understood by considering the Coulomb repulsion between the valence proton and the core. For a proton halo state to exist, we need the attractive strong force to be almost cancelled by the Coulomb repulsion, resulting in a threshold state [223, 224]. This cancellation can be seen within our formalism as an additional fine-tuning in the effective range. Note that for an s-wave proton halo state this means that the proton-core scattering length needs to be unnaturally large and that the effective range must be fine-tuned to cancel the Coulomb repulsion. The existence of proton halos is therefore doubly suppressed by the need for two fine-tunings.

Comparing the ANCs from Eq. (199) with the LO result (172), $C_{\sigma,LO} = 21.4 \text{ fm}^{-1/2}$, makes clear that the effective range must be very close to the pole position $1/(3k_C)$, such that the LSZ residue becomes large. This implies that the effective range correction for this system is much larger than what one naively expects. This is connected to the fact that proton halos contain k_C as a second scale and $k_C \gg \gamma$ for this system. Within our framework, k_C is a parameter that is independent of the Coulomb-modified effective-range parameters. When $k_C/\gamma \gg 1$, we are in the extreme Coulomb regime. In this regime the two particles tend to be close together, since otherwise the system is ripped apart by the Coulomb repulsion. This limit is realized for the $^{17}\text{F}^*$ system, where $k_C/\gamma = 3.8$. In Fig. 30 the LO electric radius is shown as a function of the Sommerfeld parameter k_C/γ , where we have used the binding momentum for $^{17}\text{F}^*$, $\gamma = 13.6$ MeV.

The blue circle is the parameter point corresponding to the physical $^{17}\text{F}^*$ system. It is clear that this system is almost in the extreme Coulomb regime. Note that the resulting LO electric radius is very small for a strong Coulomb repulsion, since it has an asymptotic $1/k_C$ behavior. At the far left, where $k_C \ll \gamma$, the system mimics that of a neutron halo, with the only difference being that the photon also can couple through minimal substitution to the nucleon field. The limiting value for $k_C/\gamma \rightarrow 0$ is therefore given by [66]

$$\lim_{k_C/\gamma \rightarrow 0} \langle r_E^2 \rangle^{(\sigma)} = \frac{1}{Q_c + 1} \frac{Q_c f^2 + (1 - f)^2}{2\gamma^2}. \quad (201)$$

In the standard power counting for systems with large s-wave scattering length the effective range enters at NLO. The hierarchy of scales in this case is $\gamma, k_C \ll 1/r_{0,\sigma}^C \sim M_{\text{core}}$, where M_{core} is the momentum scale set by the core. However, the discussion above implies that we can have $k_C r_{0,\sigma}^C \sim 1$ instead of $k_C \ll 1/r_{0,\sigma}^C$. In the zero-range limit, the inverse Coulomb momentum sets the scale for the LO electric radius and the effective-range contributions will therefore be numerically large since the LSZ-factor for s-wave proton halo nuclei with the effective range included behaves as

$$Z_\sigma \propto \frac{1}{1 - 3k_C r_{0,\sigma}^C}. \quad (202)$$

It appears to be fine tuned to the pole position with $r_{0,\sigma}^C \sim 1/(3k_C)$. In the case of the $^{17}\text{F}^*$ system the effective-range correction results in a factor 3.6–3.8 larger electric radius. This hierarchy-of-scales problem can be solved by fixing the bound-state pole position of the t-matrix at leading order and the ANC at NLO. This procedure ensures that corrections beyond NLO scale naturally again and is similar in spirit to the so-called Z-parameterization as introduced in Ref. [75].

5.7. Radiative capture in p-wave proton halos: $^7\text{Be}(p, \gamma)^8\text{B}$ and solar neutrinos

Radiative proton capture to p-wave proton-halo nuclei has also been considered in Halo EFT. In particular, the radiative capture process $^7\text{Be}(p, \gamma)^8\text{B}$, which determines the ^8B neutrino flux from the sun, was investigated [225, 226, 227]. The low-energy ($E_{cm} < 500$ keV) S -factor for $^7\text{Be}(p, \gamma)^8\text{B}$ consists entirely of electric-dipole (E1) capture from s- and d-wave initial states to the p-wave final states which dominate $^7\text{Be} + p$ configurations within ^8B . Beyond $E_{cm} = 500$ keV higher-order terms in Halo EFT presumably become important, and resonances unrelated to the S -factor in the Gamow peak appear.

The Halo EFT treatment of this E1 capture is similar to that of neutron capture reaction $^7\text{Li}(n, \gamma)^8\text{Li}$ discussed in Sec. 4 and Ref. [136]. Analogous to the $^7\text{Li} + n$ case, the $^7\text{Be} + p$ system is described by a local quantum field theory that contains fields for the proton and the ^7Be core expanded in powers of their relative momentum. (The internal structure of the proton and the core are included perturbatively at higher orders through low-energy constants matched to experiment and/or *ab initio* calculations.) However, in the $^7\text{Be} + p$ case the point-Coulomb part of the potential must be iterated to all orders when computing the scattering and bound-state wave functions [225, 226]. This can

be done exactly using the formalism discussed in Sec. 5.2, where we saw that the EFT result for the strong interaction is fully determined by the order at which the Lagrangian is truncated [206, 225, 226, 227].

The amplitude for E1 capture in Halo EFT is organized in an expansion in $M_{\text{halo}}/M_{\text{core}}$. The momentum scale M_{core} is set by the ${}^7\text{Be}$ binding energy relative to the ${}^3\text{He} + {}^4\text{He}$ threshold, 1.59 MeV, so $M_{\text{core}} \approx 70$ MeV, corresponding to a co-ordinate space cutoff of approximately 3 fm. The ${}^8\text{B}$ ground state, which is 0.1364(10) MeV below the ${}^7\text{Be} - p$ scattering continuum [78, 79], is a shallow p-wave bound state in Halo EFT. In the case of ${}^7\text{Li} + n$ we had to also include the first excited state of ${}^7\text{Li}$ as a degree of freedom in the EFT, and here too, the $J^\pi = \frac{1}{2}^-$ bound excited state of ${}^7\text{Be}$ is a field in the EFT Lagrangian. ${}^7\text{Be}^*$ is 0.4291 MeV above the ground state.

Meanwhile, the ${}^7\text{Be}$ ground state is $\frac{3}{2}^-$, and so—again as in ${}^7\text{Li} + n$ —there are two possible initial spin channels, denoted here by $s = 1, 2$. They correspond, respectively, to 3S_1 and 5S_2 components in the incoming scattering state, and E1 capture links them to, respectively, the 3P_2 and 5P_2 configurations in ${}^8\text{B}$. In this case there are large (~ 10 fm) ${}^7\text{Be} - p$ scattering lengths in both spin channels and these play a key role in the low-energy dynamics. In Eq. (137) this effect was captured through the function X , but here the large scattering lengths occur in the context of an effective-range expansion that is modified by Coulomb, see Eq. (164) above. For $p + {}^7\text{Be}$ scattering $k_C \approx 24$ MeV, and the binding momentum of ${}^8\text{B}$ is 15 MeV, so these low-momentum scales, which we generically denote by M_{halo} , are well separated from M_{core} . We anticipate that $M_{\text{halo}}/M_{\text{core}} \approx 0.2$.

5.7.1. Leading order The LO amplitude includes only direct capture. And since the core is structureless at this order only “external direct capture” (in the terminology of models, see Sec. 5.7.3 below) is possible. The parameters that appear at LO are the two asymptotic normalization coefficients (ANCs), C_s , for the ${}^7\text{Be} - p$ configuration in ${}^8\text{B}$ in each of the spin channels, together with the corresponding s-wave scattering lengths, $a_{0,s}^C$ ($s = 1, 2$) [136, 225, 226]. (Since there are two relevant spin channels here, we have removed the subscript σ that was used in Sec. 2 and indexed each scattering length by the spin channel in which it occurs.) Directly at threshold only the two ANCs $C_s, s = 1, 2$ contribute.

But these ANCs also enter the expression for the radius of ${}^8\text{B}$ (see Eq. (196) in the same combination. This *a priori* unknown combination can thus be eliminated in the S -factor expression and a correlation between $S(0)$ and $\langle r_E^2 \rangle_{\text{pt}}$ of ${}^8\text{B}$ established [226]. In other words, provided that the one-proton separation energy of ${}^8\text{B}$ is fixed, at LO in Halo EFT the electric radius is directly correlated with the S -factor at threshold at LO:

$$\langle r_E^2 \rangle \approx \left(1.5 + 0.054 \frac{S(0)}{(\text{eV b})} \right)^2 \text{ fm}^2. \quad (203)$$

This provides another example how different observables are related in Halo EFT. Note however, that this direct correlation does not exist at NLO since additional

counterterms enter. Corrections to this correlation are thus expected to be of order $M_{\text{halo}}/M_{\text{core}} \approx 20\%$.

5.7.2. Next-to-leading order This encourages us to improve the Halo EFT formula for $S(E)$ to a next-to-leading-order result, in order to obtain a precision result. At NLO $S(E)$ is [227]:

$$S(E) = f(E) \sum_s C_s^2 \left[|\mathcal{S}_{\text{EC}}(E; \delta_s(E)) + \bar{L}_s \mathcal{S}_{\text{SD}}(E; \delta_s(E)) + \epsilon_s \mathcal{S}_{\text{CX}}(E; \delta_s(E))|^2 + |\mathcal{D}_{\text{EC}}(E)|^2 \right]. \quad (204)$$

Here, $f(E)$ is an overall normalization composed of final-state phase space over incoming flux ratio, dipole radiation coupling strength, and a factor related to Coulomb-barrier penetration [225]. \mathcal{S}_{EC} is proportional to the spin- s E1 [228, 225, 136] external direct-capture matrix element between continuum ${}^7\text{Be} - p$ s-wave and ${}^8\text{B}$ ground-state wave functions. \mathcal{S}_{CX} is the contribution from capture with core excitation, i.e. into the ${}^7\text{Be}^* - p$ component of the ground state, whose size is parametrized by ϵ_s . (Since ${}^7\text{Be}^*$ is spin-half this component only occurs for $s = 1$, so $\epsilon_2 = 0$.) Because the inelasticity in ${}^7\text{Be} - p$ s-wave scattering is small [229, 230] it is an NLO effect.

The short-distance contributions, \mathcal{S}_{SD} , are also NLO. They originate from NLO contact terms in the EFT Lagrangian (96). The size of these is set by the parameters \bar{L}_s , which must be fit to data. \mathcal{S}_{EC} , \mathcal{S}_{SD} , and \mathcal{S}_{CX} are each functions of energy, E , but initial-state interactions mean they also depend on the s-wave phase shifts δ_s . At NLO, $\delta_s(E)$ is parametrized by a Coulomb-modified effective-range expansion (164) that includes all terms up to that proportional to $r_{0,s}^C k^2$, where $r_{0,s}^C$ is the effective range for spin-channel s [210, 209]. Finally, \mathcal{D}_{EC} is the E1 matrix element between the d-wave scattering state and the ${}^7\text{Be}$ bound-state wave function. It is not affected by initial-state interactions up to NLO, and hence is the same for $s = 1, 2$ channels and introduces no new parameters.

This leaves 9 parameters in total: C_s^2 , $a_{0,s}^C$ ($s = 1, 2$) at LO and five more at NLO: $r_{0,s}^C$, \bar{L}_s , and ϵ_1 [227]. (We have dropped the subscript σ for simplicity since we only consider different spin channels in the s-wave p - c interaction in this application.) The NLO amplitudes in E1 capture have been fitted to the experimental $S(E)$ data in the low-energy region in [227], but the nine parameters cannot be independently constrained from the existing capture data. However, calculations of the solar neutrino flux do not require that all parameters be known: it is enough to determine S at an energy $E = (18 \pm 6)$ keV.

In Ref. [227], the 9-dimensional posterior probability distribution function (pdf) of the NLO Halo EFT parameters was determined via a Bayesian analysis of 42 data points from all modern experiments with more than one data point for the direct-capture S -factor in the low-energy region: Junghans *et al.*, (experiments “BE1” and “BE3”) [231], Filippone *et al.*, [232], Baby *et al.*, [233, 234], and Hammache *et al.*, (two measurements published in 1998 and 2001) [235, 236]. Refs. [227, 237] contain further details. The pdf

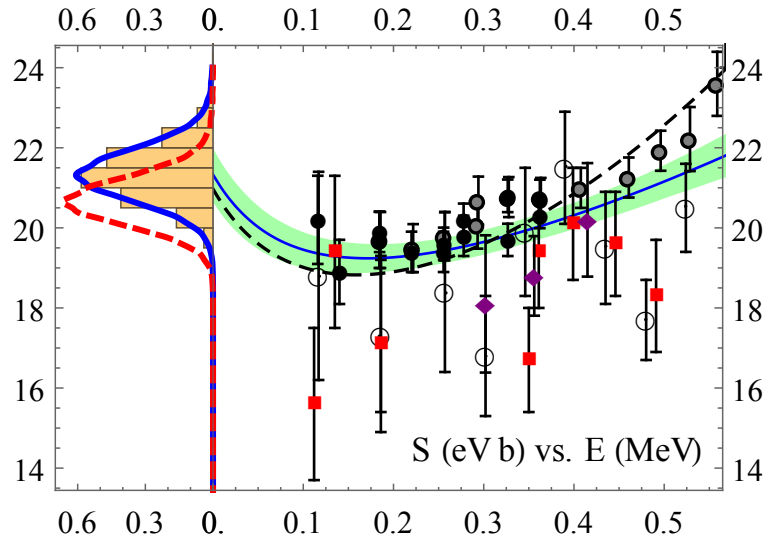


Figure 31. Right panel: NLO S -factor at different energies, including the median values (solid blue curve). Shading indicates the 68% interval. The dashed line is the LO result. The data used for parameter determination are also shown: Junghans *et al.*, BE1 and BE3 [231] (filled black circle and filled grey circle), Filippone *et al.*, [232] (open circle), Baby *et al.*, [233, 234] (filled purple diamond), and Hammache *et al.*, [235, 236] (filled red box). Left panel: 1d probability distribution functions for $S(0)$ (blue line and histogram) and $S(20 \text{ keV})$ (red-dashed line). Figure taken from Ref. [227], doi:10.1016/j.physletb.2015.11.005 under the terms of the Creative Commons Attribution License, <https://creativecommons.org/licenses/by/4.0/>.

of the Halo EFT parameters was then used to obtain the pdfs for the S -factor at energies within the domain of validity of the theory. From these a median value (the thin solid blue line in Fig. 31), and 68% interval (shaded region in Fig. 31) were extracted. The probability distribution functions for S at $E = 0$ and 20 keV are also shown on the left of the figure: the blue line and histogram are for $E = 0$ and the red-dashed line is for $E = 20 \text{ keV}$.

The S -factor at zero energy is constrained by this analysis to be

$$S(0) = (21.3 \pm 0.7) \text{ eV b}, \quad (205)$$

which is an uncertainty smaller by a factor of two than the value $S(0) = (20.8 \pm 1.6) \text{ eV b}$ recommended by Adelberger *et al.* [238] (theoretical and experimental uncertainties are added in quadrature). Zhang *et al.* also found particular choices of the EFT-parameter vector that correspond to natural coefficients, produce curves close to the median $S(E)$ curve of Fig. 31, and have large values of the posterior probability.

5.7.3. Comparison to models of this reaction In the next section we will more broadly compare and contrast Halo EFT and other theories of halo nuclei. But the case of ${}^7\text{Be}(p,\gamma)$ provides a specific instance where we can consider what Halo EFT does (and does not) do as compared to other treatments of this process.

Halo EFT provides a simple, transparent, and systematic way to organize the low-energy extrapolation of this reaction from experimentally accessible energies to the threshold region. Since the EFT incorporates all dynamics at momentum scales $< M_{\text{core}}$ its radius of convergence is larger than other efforts at systematic expansions of this S -factor [239, 135, 240, 241, 242, 243, 244, 245, 246].

Model, descriptions of this process are—like Halo EFT—dominated by “external direct capture” [247, 248]. These models involve some arbitrary choices (like Woods-Saxon shapes or matching radii) and differ in how they combine the tails of the final state with phase shift information and in how they model the non-negligible contribution from short-range, non-asymptotic regions of the wave functions.

At NLO Halo EFT includes both external direct capture and (as independent parameters) the contribution to the E1 matrix element from the short-distance part of the E1 integral ($r < \text{about } 3 \text{ fm}$) in both the $s = 1$ and $s = 2$ channel. Compared with a potential model, Halo EFT has about twice as many adjusted parameters. Statistical tests imply the resulting amplitude (204) can describe the experimental data on $S(E)$ in the low-energy region $E_{\text{cm}} < 500 \text{ keV}$. But, it can also represent all the models whose disagreement constitutes the 1.4 eV b uncertainty quoted in Ref. [238]—including the microscopic calculation of Ref. [249]. This is what allows NLO Halo EFT to obtain the high precision for $S(0)$ quoted above; by appropriate choices of its nine parameters, NLO Halo EFT spans the space of models of E1 capture in the low-energy region [227]. It therefore captures much of the model uncertainty in this problem, and allows it to be quantified—and ultimately constrained—by the capture data.

6. Comparison with other approaches

The EFT description of halo nuclei laid out here is complementary and supplementary to traditional shell-model and modern *ab initio* descriptions of nuclear structure. As such, it has much in common with phenomenological R-matrix or potential-model treatments of these systems. In this section we explore the connection of Halo EFT to these other approaches.

In the traditional shell-model approach to these systems the nucleons are viewed as largely independent particles moving in single-particle orbitals generated by the other nucleons. Residual two-body interactions between valence nucleons are included too; these are typically fit to the spectra of nuclei in a given shell.

This picture of nuclei is a different language to that we have used for discussing halo systems, since in it co-ordinates are typically discussed with respect to the center of the nucleus or, equivalently, the origin of the single-particle potential. Partial waves, and interactions, are thus expressed in this co-ordinate system. In contrast, our Halo EFT calculations refer to partial-wave interactions defined in the relative co-ordinate of the core and the halo. Such an interaction may project into several such “independent-particle basis” partial waves. In particular, in a two-neutron halo, such as ${}^6\text{He}$, the p-wave interaction between the neutron and the core can populate a variety of p-shell

independent-particle levels.

The shell-model approach also describes states as a superposition of independent-particle orbitals. For example, a nuclear ground state of spin-parity J^π could be written

$$|\Psi(J^\pi)\rangle = \sum_{NLS} C_{NLS} |N(LS)J\rangle \times |\Phi\rangle \quad (206)$$

with C_{NLS}^2 “the spectroscopic factor” of a particular single-particle state within the nuclear state $|\Psi(J^\pi)\rangle$ and $|\Phi\rangle$ the wave function of the core. Even though our description of one-nucleon halos looks like it is framed in this manner, it is not—for three reasons.

First, the halo is, by definition, weakly bound, and the halo nucleon or nucleons have a substantial fraction of their wave function outside the nuclear mean field. In a shell-model calculation such a state necessarily involves significant “coupling to the continuum”. In the Halo EFT approach any bound states appear as eigenstates of the Hamiltonian of a negative energy, and the “coupling to the continuum” is automatically included.

Second, Halo EFT does not emphasize, or even require, spectroscopic factors. At long distances a single partial wave dominates all the halos we have considered here. Therefore the long-distance part of the wave function can be defined unambiguously, and the Halo EFT wave function has only one component. In the shell-model representation it may well be that several single-particle states contribute, but it is clear that in a basis with the correct long-distance behavior of the halo wave function only one component is required to describe that part. Other components can—and will—enter at short distances [250]. But we do not consider that piece of the wave function in our treatment, and so spectroscopic factors are not needed. Instead, all the interior effects that are modeled by inclusion of many shell-model states in the wave function of the state $|\Psi(J^\pi)\rangle$ are transformed into short-distance operators, whose impact on low-energy observables is then organized according to the EFT power counting.

These short-distance operators can also take account of the impact that deformation of the nuclear core has on some observables. For example, comparing our calculation of ^{11}Be with a shell-model treatment of the same nucleus, it is clear that one effect which is subsumed into the NLO counterterm $L_{E1}^{(1/2)}$ is the transition of a neutron from a $d_{5/2}$ to a $p_{3/2}$ orbital, with that neutron coupled to the 2^+ state of ^{10}Be . This 2^+ state is 3.4 MeV above the ^{10}Be ground state, so the dynamics associated with it takes place at distances $1/M_{\text{core}}$. Hence in our EFT it can only appear in short-distance operators such as that multiplying $L_{E1}^{(1/2)}$ in Eq. (96). The computation of Ref. [251] suggests that such a contribution reduces the E1 matrix element by $\approx 30\%$, which is the anticipated size of an NLO effect when the $M_{\text{halo}}/M_{\text{core}}$ expansion is employed in the ^{11}Be system. We thus see that Halo EFT can use a point-like core, and avoid the traditional treatment in terms of a deformed rotator, as long as the energy required to excite the corresponding rotational band is large compared to the energy of the halo system. Archaeology of Halo EFT’s short-distance operators in terms of shell-model descriptions of the same system could be interesting, since the shell model has historically had much success describing the dynamics of nuclei at distances of order $\sim 1/M_{\text{core}}$.

A contrasting example, where low-lying excited states of the core (albeit not due to deformation) are included in the EFT is the treatment of ${}^7\text{Li}(n, \gamma){}^8\text{Li}$ in Ref. [136]. The first excited state of ${}^7\text{Li}$ lies only 0.48 MeV above the ground state; the effects of this state cannot be replaced by contact operators for reactions that take place at this energy scale. Generally speaking, once energies comparable to its excitation energy are attained a state cannot be integrated out of the EFT’s Fock space. Instead, these low-lying excitations of the core must be included explicitly in the calculation. Halo EFT is sufficiently flexible that this can be done if it will improve the convergence of the theory.

The No-Core Shell Model (NCSM) involves an exact diagonalization of a particular $\text{NN} + 3\text{N}$ Hamiltonian, \hat{H} , in the harmonic-oscillator basis [252]. The choice of oscillator parameter predicates the convergence of this *ab initio* method to nuclei whose size is of order the oscillator length. Systems that are weakly bound compared to that length scale, and so have exponential tails that persist outside the parabolic potential, converge very slowly with basis size in the NCSM. This was recognized early in the development of the NCSM, and some early studies ameliorated this issue by matching the NCSM wave function to the asymptotic form [253, 254]. The issue of incorrect asymptotics also initially precluded the treatment of scattering within the NCSM. However, over the last decade the NCSM has been successfully combined with Resonating-Group Method (RGM) ideas. The basis for diagonalization now includes the NCSM set of solutions of the A -body problem, together with clustered wave functions corresponding to a few low-lying two-body channels. If the clusters contain a and b particles respectively (with $A = a + b$) then these clustered wave functions are products of solutions of \hat{H} in the a - and b -body spaces, with the wave function representing the relative degree of freedom between the two clusters initially unknown [255, 256]:

$$|\Psi(J^\pi)\rangle = \sum_{\lambda} |A\lambda J^\pi\rangle + \sum_{\text{channels } ab, \nu} \frac{\gamma_{\nu}(r_{ab})}{r_{ab}} \mathcal{A}_{\nu} [|a\lambda_a J_a^\pi\rangle |b\lambda_b J_b^\pi\rangle]^s Y_l(\hat{r}_{ab})]^{J^\pi}. \quad (207)$$

In the first, standard NCSM, term, λ indicates states of A particles in the harmonic-oscillator basis (quantum numbers N , L , and spins) ‡. The second term includes all relevant two-body clusterizations and has ν as a collective label that enumerates the states in the product representation of the two harmonic oscillator bases, coupled to appropriate spin, orbital angular momentum, total J , and isospin (not shown): $\nu = \{\lambda_a J_a^\pi; \lambda_b J_b^\pi; s, l\}$. \mathbf{r}_{ab} is the relative co-ordinate between the centers-of-mass of the a and b clusters. Lastly, the anti-symmetrizer \mathcal{A}_{ν} ensures that the resulting wave function is anti-symmetric. (For a full discussion with more explicit notation, see Refs. [255, 256].)

Ab initio calculations that use the basis (207) are referred to as “No-Core Shell Model with Continuum” (NCSMC). The basis is over-complete, but this is dealt with using an extension of the standard RGM procedure of constructing a norm kernel and thereby obtaining orthogonalized cluster-channel states [256]. The division between

‡ Note that, in contrast to the above discussion of the nuclear shell model, here the wave function is formulated in relative coordinates.

long- and short-distance is not as straightforward as that the first, NCSM, term gives the short-distance behavior and the second, clustered, part gives the long-distance behavior. For one thing the norm kernel explicitly induces short-distance effects due to anti-symmetrization of nucleons between the two clusters. For another, the inclusion of clusters in the NCSMC basis can improve the convergence of the short-distance part of the wave function with basis size. Nevertheless, at long distances only the clustered piece of the wave function survives, and from it the scattering phase shifts between the a -body and b -body clusters can be obtained. The intimate connection between the scattering matrix and low-energy bound states that we've emphasized throughout this review then guarantees that halo states should be accessible within the NCSMC, too. And indeed, the clustered part of the NCSMC basis contains exactly the states needed to improve the convergence of the diagonalization for halos built on those clusters. In practice, an R-matrix technique is used to solve the NCSMC equations: beyond r_0 it is assumed that only the Coulomb potential acts between the two clusters, and the solution of \hat{H} for $r < r_0$ is matched to Whittaker (or Coulomb) functions at that radius. The NCSMC (or its predecessor the NCSM + RGM) have now been successfully applied to one-nucleon halo systems discussed in this review: ${}^5\text{He}$ [257, 258, 256], ${}^8\text{B}$ [230], and ${}^{11}\text{Be}$ [91]. The NCSM + RGM has also recently been extended to three-body configurations, for example, ${}^4\text{He} + n + n$ [259, 144], and augmented with NCSM six-body eigenstates to produce both bound and scattering solutions for ${}^6\text{He}$ [260].

RGM-augmented NCSM wave functions of the form (207) are not the only method that has been employed to circumvent the harmonic-oscillator basis' difficulties in describing halo nuclei. The so-called "Gamow shell model" diagonalizes \hat{H} on a basis with the correct asymptotics for shallow bound states, and has been employed to obtain the energies and widths of the low-energy p-wave resonances in the ${}^4\text{He} + n$ system [261]. The Gamow-shell-model basis can also be combined with an RGM-type expansion à la Eq. (207) to compute scattering phase shifts [262, 263].

Finally, we note that although we have dwelt on these issues in the context of the NCSM they are not exclusive to this *ab initio* technique. To take one other example, Green's Function Monte Carlo calculations of halo states have been slow to emerge in part because the method is predicated on a finite volume, and the calculation of halo states is therefore computationally (even more) challenging. GFMC calculations of the charge radius of ${}^6\text{He}$ had to be tuned very carefully in order to ensure that this long-distance observable in the halo system was completely converged [264]. Halo EFT could perhaps be used to compute the finite-volume effects that complicate convergence in such cases [265].

The ability of *ab initio* methods like the NCSMC to solve for structure and low-energy reactions in systems like ${}^{11}\text{Be}$ and ${}^6\text{He}$, that have been analyzed in Halo EFT, opens new possibilities for the EFT to take *ab initio* results as input, and so divorce itself from the need to fix the coefficients of contact operators from experiment. This provides consistency checks on the implementation of long-distance physics in the *ab initio* calculation, and insights into the EFT convergence pattern. It also means the EFT

can be combined with the *ab initio* input to predict observables that remain challenging for direct computation in the *ab initio* approach.

The R-matrix employed to solve the NCSMC equations is an *ab initio* R-matrix, constructed from knowledge of the interior wave function. Since Halo EFT is agnostic about this portion of the nuclear state it perhaps has more in common with the phenomenological R-matrix, where, for scattering, the exterior of the wave function ($r > r_0$) is expressed in terms of phase shifts and asymptotic solutions (typically Whittaker or Coulomb functions) and the only thing known about the interior is the R-matrix that encodes the log derivatives and channel couplings at the boundary $r_{ab} = r_0$. Any resonances needed to describe scattering in the kinematic domain of interest are incorporated explicitly into the R-matrix fit—just as in Halo EFT resonances can be added as explicit degrees of freedom. In contrast to Halo EFT, the non-resonant part of the scattering is described through a combination of scattering due to a hard core of radius r_0 and “background resonances” at higher energies. The effective-range expansion emerges from the R-matrix description for low scattering energies [266], but the parameters of the phenomenological R-matrix fit must be tuned to obtain specific values of the effective-range parameters.

For capture reactions the distinction between interior and exterior contributions again makes the connection with EFT strong: for each resonance there is an “external” ($r > r_0$) part of the capture that is computed explicitly using the asymptotic wave function of that resonance. The interior part of every resonance’s capture matrix element is parameterized, and must be fit to capture data. This means that R-matrix predicts the rapidly-varying-with-energy pieces of the capture cross section (effects due to resonances, Coulomb and angular-momentum barriers, external direct capture) and fits the short-distance, more slowly varying, pieces to experiment. This is very similar to the EFT formulation of $n + p \rightarrow d + \gamma$, ${}^7\text{Li}(n, \gamma){}^8\text{Li}$, ${}^7\text{Be}(p, \gamma){}^8\text{B}$, etc. Indeed, it has been shown that—at least in the cases of np scattering and $d + {}^3\text{H} \rightarrow n + {}^4\text{He}$ —Halo EFT is obtained in the limit of an R-matrix calculation with $r_0 \rightarrow 0$ [165, 267]. The extension of this result to radiative captures awaits proof, but seems plausible. All of this suggests that—at least at low energies—R-matrix analyses may be amenable to error estimates and uncertainty quantification of the type advocated for and carried out in EFT frameworks in Refs. [60, 61, 227, 268, 269]. Another place that Halo EFT could augment R-matrix is in the consistent treatment of three-body reactions. The phenomenological R-matrix has traditionally not been applied in such channels, and only recently have attempts been made at a phenomenological R-matrix formulation of, e.g., ${}^4\text{He} + n + n$ [270].

Lastly, Halo EFT also has much in common with potential models based on clusters. After all, many of the EFT Lagrangians employed here can be recast as Schrödinger-equation calculations with particular two-body (and three-body) potentials. The physics of Halo EFT is very much the same physics as was expressed in these potential models. However, because EFT is a minimal formulation of the halo physics at a given accuracy it can diagnose the correlations that drive the phenomenology of reactions and halo

structure, and so help to explain why different potential models produce different results. For example, Rupak and Higa showed that differences in potential-model predictions for ${}^7\text{Li}(n, \gamma)$ were entirely due to those models having different values of the p-wave effective range r_1 in the channel(s) where ${}^8\text{Li}$ binds: disparate predictions stemmed from variations in the bound-state ANC, and were not due to any sensitivity to the form of the potential [146]. Another key difference between EFT and potential models is the use of power counting to organize the contributions to the potentials, as well as the recognition that two-body potentials will not, in general, exhaust the physics of a system. Higher-body operators—three-body forces in multi-particle systems and two-cluster currents in electromagnetic processes—will always enter, and no amount of tuning of the two-body potential can ensure that all of them go to zero. Once again, the systematic organization of the EFT is key, as it ensures that this set of higher-body operators does not become a plethora, but instead can be organized to make the calculation manageable. In few-nucleon systems the use of such organization—and the associated uncertainty quantification it provides—has brought renewed vigour to the study of few-nucleon systems in the past two decades. Similar possibilities await halo nuclei.

7. Conclusion, sins of omission, and future paths

7.1. Summary

Effective field theory provides a robust method for the study of low-energy observables in halo nuclei. Halo EFT is based on a systematic expansion exploiting the hierarchy between the momentum scales associated with the halo (M_{halo}) and the core (M_{core}). In contrast to standard pionless EFT explicit fields are introduced for tightly bound clusters of nucleons. The uncertainty of Halo EFT calculations is estimated and improved by using the expansion in $M_{\text{halo}}/M_{\text{core}}$, which provides a systematic organization for calculations of halo observables. Such calculations capture the physics that is essential to the long-distance properties of halo nuclei and clustered systems. Short-distance effects are not resolved explicitly but their effect on long-distance observables is captured by local operators. In particular, the EFT predicts that halo observables are connected by few-body universality: the idea that low-energy properties of weakly-bound few-body systems share properties that are independent of the details of the interactions at short distances.

In this review, we have discussed the Halo EFT approach for calculating structure and reaction observables in halo nuclei. In one- and two-neutron s-wave halos we built the Lagrangian and explained the formalism for calculating binding energies, matter radii, and Efimov states. The formalism was then extended to resonances and bound states in one- and two-neutron halos involving p-wave neutron-core interactions. By introducing external electromagnetic currents, we explained the EFT calculations of Coulomb dissociation, radiative capture, and the electric radii of halo nuclei. The Halo

EFT formalism with electromagnetic interactions was then extended to proton halos, whose structure depends on a delicate interplay of the strong and Coulomb interactions between the proton and core. Lastly, we connected Halo EFT to other theoretical approaches for investigating weakly-bound halo nuclei and discussed possible synergies.

7.2. Sins of omission

There are some frontier topics that have been treated within the Halo EFT framework but are not covered in detail by this review. Here we briefly discuss two examples: halo systems with strangeness and four-body systems.

7.2.1. Halo systems with strangeness Halo structures also exist in a unique type of nuclear system produced by strangeness-exchange reactions, namely hypernuclei. In such systems, one or two of the constituent nucleons are replaced by hyperons (see, e.g., Ref. [271] for a review). The lightest known hypernucleus is the hypertriton ${}^3_{\Lambda}\text{H}$, which consists of a proton, a neutron, and a Λ hyperon. ${}^3_{\Lambda}\text{H}$ is a non-Borromean system: the np pair can be bound, while the $n\Lambda$ and $p\Lambda$ pairs are unbound. The separation energy of the Λ in ${}^3_{\Lambda}\text{H}$ is $S_{\Lambda} = 0.13(5)$ MeV [272, 273], one order of magnitude smaller than the binding of the deuteron. As a consequence, the very low energy properties of ${}^3_{\Lambda}\text{H}$ can be described in an EFT with Λ and deuteron degrees of freedom [274]. Above the deuteron breakup threshold a three-body treatment is required. Due to the limited data from $N\Lambda$ scattering experiments, and the fact they are available only at relatively high energy, the $N\Lambda$ interaction is not as well constrained as the NN interaction. A recent calculation based on SU(3) chiral EFT potentials at next-to-leading order determined the $N\Lambda$ scattering lengths to be -2.9 fm in the singlet channel and -1.6 fm in the triplet channel [275]. These values are consistent with phenomenological models [276, 277] and markedly larger than the range of the $N\Lambda$ interaction, which is driven by two-pion exchange. Therefore, we can, once again, use the $M_{\text{halo}}/M_{\text{core}}$ scale hierarchy and study weakly bound systems in hypernuclei using the EFT discussed in this review: the $N\Lambda$ potentials are represented by contact interactions. In this spirit, in Ref. [278] Hammer performed a leading-order EFT calculation in ${}^3_{\Lambda}\text{H}$, where an Efimov-like limit cycle behavior was found in the $np\Lambda$ three-body system. In addition, the low-energy phase shift parameters for the doublet Λ - ${}^2\text{H}$ scattering was calculated through their universal correlations with the ${}^3_{\Lambda}\text{H}$ binding energy. Hammer found $a_{\Lambda-{}^2\text{H}} = 16.8^{+4.4}_{-2.4}$ fm and $r_{\Lambda-{}^2\text{H}} = 2.3(3)$ fm, with the errors associated with the uncertainty in the ${}^3_{\Lambda}\text{H}$ binding energy. Intrigued by experimental hints of a possibly bound ${}^3_{\Lambda}n$ state [279], Ando *et al.* recently applied the same EFT to investigate the $nn\Lambda$ three-body system as a Borromean halo [280].

Light double- Λ hypernuclei open other opportunities for studying halo/clustering phenomena. The investigation of such exotic systems is crucial for understanding the hyperon-hyperon interaction. The observation of ${}^6_{\Lambda\Lambda}\text{He}$ in hybrid emulsion experiments determined the two Λ separation energy, $B_{2\Lambda} \approx 7$ MeV, and the Λ - Λ interaction energy

of approximately 1 MeV [281, 282]. These energy scales are considerably shallower than the excitation energy of the ${}^4\text{He}$ nucleus. This suggests a halo structure Λ - Λ - ${}^4\text{He}$ in ${}^6_{\Lambda\Lambda}\text{He}$. Using Halo EFT, Ando *et al.* investigated ${}^6_{\Lambda\Lambda}\text{He}$ and predicted a universal correlation between $B_{2\Lambda}$ and the Λ - Λ scattering length at leading-order accuracy [283]. Similar EFT arguments were applied to ${}^4_{\Lambda\Lambda}\text{H}$ to describe its halo features in a Λ - Λ - ${}^2\text{H}$ configuration [274].

7.2.2. Four-body systems Halo EFT studies have also been carried out for systems with more than three particles. These also manifest few-body universality in the large scattering length limit. Combining an EFT formulation at leading order with Yakubovsky equations in the presence of a three-body coupling [284], Platter *et al.* found that the discrete scaling symmetry (4) persists in systems of four identical bosons [28, 29] and no four-body force is required for renormalization at leading order in the $M_{\text{halo}}/M_{\text{core}}$ expansion. They predicted that there are two four-body states (tetramers) universally tied to each three-body state (trimer), given that the momentum scales of these tetramers, $(mB_4)^{1/2}$, are much smaller than M_{core} . This four-body EFT formalism was then extended to describe the α -particle as a four-nucleon system, and the well-known empirical correlation between the binding energies of the triton and the α -particle (the Tjon line) was explained by the absence of a four-body force at leading order [285].

The universal behavior of Efimov tetramers was also found by calculations in short-range potential models [286, 287, 288], and has been observed in experiments using ultracold atomic gases of ${}^7\text{Li}$ [289], ${}^{39}\text{K}$ [290], and ${}^{133}\text{Cs}$ [291]. The long-predicted excited Efimov trimer of ${}^4\text{He}$ atoms has been recently observed in a Coulomb explosion imaging measurement [292]. This finding motivates further investigations searching for ${}^4\text{He}$ Efimov tetramers. These studies on Efimov tetramers in cold atoms raise the question of whether there are analogous structures in halo nuclei.

However, it is difficult to find a three-neutron halo that is stable, due to Pauli-blocking effects in a configuration with three valence neutrons. In such a system at least one of the valence neutrons must interact with the core in a p-wave, which tends to increase the ground-state energy of the three-neutron halo compared to the corresponding two-neutron isotope. While such a system could have universal properties it would not display an Efimov character and discrete scale invariance. However, neutron halos are just one example of a clustered few-body system that exhibits large-scattering-length physics. The first excited state of the α particle is a 0^+ state, and is thought to be a breathing mode of the ground state [293, 294, 295]. It is a possible candidate for a four-nucleon Efimov resonance and lies only 0.4 MeV above the ${}^3\text{H}+p$ threshold. However, the structure of this state is complicated by the presence of the long-range Coulomb interaction between protons since the Coulomb momentum is comparable to the momentum scale of this excited state. The excited 0^+ state in ${}^{10}\text{Be}$, whose binding energy is only 1.2 MeV below the ${}^6\text{He}+\alpha$ threshold, may also be thought of as a four-body Efimov state of the αann system. Its structure is complicated not only

by nonperturbative α - α Coulomb interactions, but also by the presence of the p-wave resonances that dominate in the n - α subsystem at low energies. The possibility to realize—even if only approximately—aspects of Efimov physics in these and other halo four-body systems remains an important subject for future study.

7.3. Future paths

The EFT formalism can be extended to new directions to further enhance understanding of halo nuclei. For example, a number of radiative capture processes whose physics parallels ${}^7\text{Be}(p, \gamma){}^8\text{B}$ are important in astrophysics. Halo EFT should be applicable to many of them.

In nuclear reactions with exotic beams, the interplay between nuclear forces and electromagnetic interactions determines the relevant reaction mechanisms at different incident beam energies. Coulomb dissociation requires either a very low incident energy or a very forward-angle fragmentation, so that the halo projectile does not penetrate the Coulomb barrier of the high-charge nuclear target. With a light nuclear target, the reaction mechanism is dominated by nuclear interactions, provided the momentum transferred is at least of order the Coulomb momentum between the target and projectile. Such reactions are realized, in elastic scattering (e.g., (p, p) [296, 297, 298]), nucleon knockout reactions (e.g., (p, pn) [299, 300]), and nucleon transfer reactions (e.g., (p, d) [301], (p, t) [302], and (d, p) [303, 304]).

Theoretical analyses of “direct” reaction mechanisms have been performed with the development of many independent approaches, including the distorted-wave Born approximation (DWBA), the dynamical eikonal approximation (DEA), the continuum discretized coupled channels (CDCC) method, and the Faddeev-Yakubovsky scattering calculation (see *e.g.* Refs. [305, 306, 307, 308, 309, 310, 311] for applications in halo nuclei). If the momentum transfer in the reaction is near the halo scale M_{halo} , it should be feasible to extend the existing Halo EFT calculations to describe the corresponding reaction mechanism. Using the $M_{\text{halo}}/M_{\text{core}}$ expansion, one can systematically construct the hierarchy of different interaction channels that contribute to the reaction. This controlled expansion may reduce or clarify the optical-potential-model dependence in traditional reaction theories. The Halo EFT is based on a Faddeev-Yakubovsky scattering calculation and uses consistent nucleon-core interactions within the halo and among projectile and target fragments. Therefore it can, in principle, provide a unified description of structure and reaction observables.

Acknowledgments

We thank our collaborators for fruitful investigations and informative conversations on the topics discussed here. We are especially grateful to Bijaya Acharya for providing the updated calculations that appear in Fig. 8 and to Jared Vanasse for carefully reading the manuscript and supplying the cross sections used in Fig. 15. We also thank

Pierre Capel and Takashi Nakamura for supplying data and information relevant to Fig. 16. We appreciated useful comments on this manuscript made by Carl Brune and Sofia Quaglioni. We thank the ECT* and the organizers of the workshops “Three-body systems in reactions with rare isotopes ” and “Open quantum systems: from atomic nuclei to ultracold atoms and quantum optics”, as well as the organizers of the KITP program “Universality in few-body systems”: all three constituted an excellent environment in which to work on this article. DRP’s work at the KITP was supported in part by the National Science Foundation under Grant No. NSF PHY11-25915. This research was also supported by the U.S. Department of Energy under grant DE-FG02-93ER40756, by the German Federal Ministry of Education and Research under contract 05P15RDFN1, and by the Deutsche Forschungsgemeinschaft (SFB 1245).

References

- [1] M. V. Zhukov, B. V. Danilin, D. V. Fedorov, J. M. Bang, I. J. Thompson, and J. S. Vaagen. Bound state properties of Borromean Halo nuclei: ${}^6\text{He}$ and ${}^{11}\text{Li}$. *Phys. Rept.*, 231:151–199, 1993.
- [2] P. G. Hansen, A. S. Jensen, and B. Jonson. Nuclear halos. *Ann. Rev. Nucl. Part. Sci.*, 45:591–634, 1995.
- [3] B. Jonson. Light dripline nuclei. *Phys. Rept.*, 389(1):1 – 59, 2004.
- [4] A. S. Jensen, K. Riisager, D. V. Fedorov, and E. Garrido. Structure and reactions of quantum halos. *Rev. Mod. Phys.*, 76:215–261, 2004.
- [5] K. Riisager. Halos and related structures. *Phys. Scripta*, T152:014001, 2013.
- [6] I. Tanihata. Nuclear Physics with RIB’s: How it all started. *Eur. Phys. J. Plus*, 131(4):90, 2016.
- [7] P. G. Hansen and B. Jonson. The Neutron halo of extremely neutron-rich nuclei. *Europhys. Lett.*, 4:409–414, 1987.
- [8] H. Georgi. Effective field theory. *Ann. Rev. Nucl. Part. Sci.*, 43:209–252, 1993.
- [9] D. B. Kaplan. Effective field theories. In *Beyond the standard model 5. Proceedings, 5th Conference, Balholm, Norway, April 29-May 4, 1997*, 1995.
- [10] A. V. Manohar. Effective field theories. *Lect. Notes Phys.*, 479:311–362, 1997.
- [11] D. R. Phillips. Building light nuclei from neutrons, protons, and pions. *Czech. J. Phys.*, 52:B49, 2002.
- [12] C. P. Burgess. Introduction to Effective Field Theory. *Ann. Rev. Nucl. Part. Sci.*, 57:329–362, 2007.
- [13] H.-W. Hammer and Sebastian König. General aspects of effective field theories and few-body applications. *Lect. Notes Phys.*, 936:93, 2017.
- [14] S. R. Beane, P. F. Bedaque, W. C. Haxton, D. R. Phillips, and M. J. Savage. From hadrons to nuclei: crossing the border. In *At the frontier of particle physics—handbook of QCD*, pages 133–271. World Scientific, Singapore, 2001.
- [15] P. F. Bedaque and U. van Kolck. Effective field theory for few-nucleon systems. *Ann. Rev. Nucl. Part. Sci.*, 52:339–396, 2002.
- [16] E. Epelbaum, H.-W. Hammer, and U.-G. Meißner. Modern Theory of Nuclear Forces. *Rev. Mod. Phys.*, 81:1773–1825, 2009.
- [17] J. Vanasse. Three-body systems in pionless effective field theory. *Int. J. Mod. Phys.*, E25(05):1641002, 2016.
- [18] C. A. Bertulani, H.-W. Hammer, and U. Van Kolck. Effective field theory for halo nuclei. *Nucl. Phys.*, A 712:37–58, 2002.
- [19] P. F. Bedaque, H.-W. Hammer, and U. van Kolck. Narrow resonances in effective field theory. *Phys. Lett.*, B 569:159–167, 2003.

- [20] V. N. Efimov. Weakly-bound states of 3 resonantly interacting particles. *Sov. J. Nucl. Phys.*, 12:589, 1971.
- [21] V. Efimov. Low-energy properties of 3 resonantly interacting particles. *Sov. J. Nucl. Phys.*, 29:546, 1979.
- [22] E. Braaten and H.-W. Hammer. Universality in few-body systems with large scattering length. *Phys. Rept.*, 428:259–390, 2006.
- [23] P. F. Bedaque, H.-W. Hammer, and U. van Kolck. The Three boson system with short range interactions. *Nucl. Phys.*, A646:444–466, 1999.
- [24] P. F. Bedaque, H.-W. Hammer, and U. van Kolck. Renormalization of the three-body system with short range interactions. *Phys. Rev. Lett.*, 82:463–467, 1999.
- [25] A. C. Phillips. Consistency of the Low-energy Three-nucleon Observables and the Separable Interaction Model. *Nucl. Phys.*, A107:209, 1968.
- [26] V. Efimov. Energy levels arising from the resonant two-body forces in a three-body system. *Phys. Lett.*, B33:563–564, 1970.
- [27] E. Braaten, H.-W. Hammer, and M. Kusunoki. Universal equation for Efimov states. *Phys. Rev.*, A67:022505, 2003.
- [28] L. Platter, H.-W. Hammer, and U.-G. Meißner. The Four-boson system with short-range interactions. *Phys. Rev.*, A70:052101, 2004.
- [29] H.-W. Hammer and L. Platter. Universal Properties of the Four-Body System with Large Scattering Length. *Eur. Phys. J.*, A32:113–120, 2007.
- [30] R. Schmidt and S. Moroz. Renormalization group study of the four-body problem. *Phys. Rev.*, A81:052709, 2010.
- [31] J. Kirscher, N. Barnea, D. Gazit, F. Pederiva, and U. van Kolck. Spectra and Scattering of Light Lattice Nuclei from Effective Field Theory. *Phys. Rev.*, C92(5):054002, 2015.
- [32] S. König, H. W. Griebhammer, H.-W. Hammer, and U. van Kolck. Nuclear Physics Around the Unitarity Limit. *Phys. Rev. Lett.* 118:202501, 2017.
- [33] A. Deltuva. Efimov physics in bosonic atom-trimer scattering. *Phys. Rev.*, A82:040701, 2010.
- [34] A. Deltuva. Shallow Efimov tetramer as inelastic virtual state and resonant enhancement of the atom-trimer relaxation. *Europhys. Lett.*, 95:43002, 2011.
- [35] A. Deltuva. Universality in bosonic dimer-dimer scattering. *Phys. Rev.*, A84:022703, 2011.
- [36] A. Deltuva. Universal bosonic tetramers of dimer-atom-atom structure. *Phys. Rev.*, A85:042705, 2012.
- [37] J. Kirscher, H. W. Griebhammer, D. Shukla, and H. M. Hofmann. Universal Correlations in pionless EFT with the Resonating Group Model: Three and Four Nucleons. *Eur. Phys. J.*, A44:239–256, 2010.
- [38] G. J. Hanna and D. Blume. Energetics and structural properties of three-dimensional bosonic clusters near threshold. *Phys. Rev. A*, 74:063604, 2006.
- [39] J. von Stecher. Weakly Bound Cluster States of Efimov Character. *J. Phys.*, B43:101002, 2010.
- [40] J. von Stecher. Universal Five- and Six-Body Droplets Tied to an Efimov Trimer. *Phys. Rev. Lett.*, 107:200402, 2011.
- [41] A. N. Nicholson. N-body Efimov states from two-particle noise. *Phys. Rev. Lett.*, 109:073003, 2012.
- [42] B. Bazak, M. Eliyahu, and U. van Kolck. Effective Field Theory for Few-Boson Systems. *Phys. Rev.*, A94(5):052502, 2016.
- [43] M. Gattobigio, A. Kievsky, and M. Viviani. Spectra of helium clusters with up to six atoms using soft core potentials. *Phys. Rev.*, A84:052503, 2011.
- [44] M. Gattobigio, A. Kievsky, and M. Viviani. Energy spectra of small bosonic clusters having a large two-body scattering length. *Phys. Rev.*, A86:042513, 2012.
- [45] M. Gattobigio and A. Kievsky. Universality and scaling in the N -body sector of Efimov physics. *Phys. Rev.*, A90(1):012502, 2014.
- [46] A. Kievsky, M. Viviani, M. Gattobigio, C. Romero-Redondo, and E. Garrido. Structure and

- dynamics of few-helium clusters using soft-core potentials. *Phys. Atom. Nucl.*, 77:463–471, 2014.
- [47] A. Kievsky, N. K. Timofeyuk, and M. Gattobigio. N -boson spectrum from a Discrete Scale Invariance. *Phys. Rev.*, A90(3):032504, 2014.
- [48] U. van Kolck, Unitarity and discrete scale invariance *Few-Body Syst.* 58:112, 2017.
- [49] F. Ferlaino, A. Zenesini, M. Berninger, B. Huang, H.-C. Nägerl, and R. Grimm. Efimov Resonances in Ultracold Quantum Gases. *Few-Body Systems*, 51:113–133, 2011.
- [50] A. Zenesini, B. Huang, M. Berninger, S. Besler, H.-C. Nägerl, F. Ferlaino, R. Grimm, C. H. Greene, and J. von Stecher. Resonant five-body recombination in an ultracold gas of bosonic atoms. *New Journal of Physics*, 15(4):043040, 2013.
- [51] P. Naidon and S. Endo. Efimov Physics: a review. *Rep. Prog. Phys.* 80, 056001, 2017.
- [52] H.-W. Hammer. Few-Body Universality in Halo Nuclei. *EPJ Web Conf.*, 113:01004, 2016.
- [53] A. O. Macchiavelli. How to Study Efimov States in Exotic Nuclei? *Few Body Syst.*, 56(11-12):773–778, 2015.
- [54] M. Jona-Lasinio, L. Pricoupenko, and Y. Castin. Three fully polarized fermions close to a p-wave feshbach resonance. *Phys. Rev. A*, 77:043611, 2008.
- [55] Y. Nishida. Impossibility of the Efimov effect for p-wave interactions. *Phys. Rev.*, A86:012710, 2012.
- [56] E. Braaten, P. Hagen, H.-W. Hammer, and L. Platter. Renormalization in the Three-body Problem with Resonant P-wave Interactions. *Phys. Rev.*, A86:012711, 2012.
- [57] K. Harada, H. Kubo, and A. Ninomiya. More about the Wilsonian analysis on the pionless NEFT. *Int. J. Mod. Phys.*, A24:3191–3225, 2009.
- [58] J. Braun and H.-W. Hammer. Electric Properties of One-Neutron Halo Nuclei in Halo EFT. In *Proceedings, 23rd European Conference on Few-Body Problems in Physics (EFB23): Aarhus, Denmark, August 8-12, 2016*. arXiv:1612.07689 [nucl-th].
- [59] C. Ji. Three-body systems in physics of cold atoms and halo nuclei. *Int. J. Mod. Phys.*, E25(05):1641003, 2016.
- [60] R. J. Furnstahl, N. Klco, D. R. Phillips and S. Wesolowski, Quantifying truncation errors in effective field theory. *Phys. Rev.* C92:024005 (2015).
- [61] J. Melendez, R. J. Furnstahl, and S. Wesolowski, Bayesian truncation errors in chiral effective field theory: nucleon-nucleon observables. *Phys. Rev.* C96:024002 (2017).
- [62] D. Baye, P. Descouvemont, Antisymmetrization effects in radiative capture reactions. *Annals Phys.*, 165:115–147, 1985.
- [63] T. Nakamura et al. Coulomb dissociation of ^{19}C and its halo structure. *Phys. Rev. Lett.*, 83:1112–1115, 1999.
- [64] E. Braaten and H.-W. Hammer. Universality in the three body problem for He-4 atoms. *Phys. Rev. A*, 67:042706, 2003.
- [65] L. Platter and D. R. Phillips. The Three-Boson System at Next-To-Next-To-Leading Order. *Few Body Syst.*, 40:35–55, 2006.
- [66] H.-W. Hammer and D. R. Phillips. Electric properties of the Beryllium-11 system in Halo EFT. *Nucl. Phys.*, A865:17–42, 2011.
- [67] D. B. Kaplan. More effective field theory for nonrelativistic scattering. *Nucl. Phys.*, B494:471–484, 1997.
- [68] P. F. Bedaque and U. van Kolck. Nucleon deuteron scattering from an effective field theory. *Phys. Lett.*, B428:221–226, 1998.
- [69] P. F. Bedaque, H.-W. Hammer, and U. van Kolck. Effective theory of the triton. *Nucl. Phys.*, A676:357–370, 2000.
- [70] P. F. Bedaque and H. W. Grißhammer. Quartet s-wave neutron-deuteron scattering in effective field theory. *Nucl. Phys.*, A671:357–379, 2000.
- [71] S. R. Beane and M. J. Savage. Rearranging pionless effective field theory. *Nucl. Phys.*, A694:511–524, 2001.

- [72] D. B. Kaplan, M. J. Savage, and M. B. Wise. A new expansion for nucleon-nucleon interactions. *Phys.Lett.*, B424:390–396, 1998.
- [73] D. B. Kaplan, M. J. Savage, and M. B. Wise. Two nucleon systems from effective field theory. *Nucl.Phys.*, B534:329–355, 1998.
- [74] D. R. Phillips, S. R. Beane, and M. C. Birse. Scheming in dimensional regularization. *J. Phys.*, A32:3397–3407, 1999.
- [75] D. R. Phillips, G. Rupak, and M. J. Savage. Improving the convergence of NN effective field theory. *Phys. Lett.*, B473:209–218, 2000.
- [76] J.-W. Chen, G. Rupak, and M. J. Savage. Nucleon-nucleon effective field theory without pions. *Nucl. Phys.*, A653:386–412, 1999.
- [77] I. Tanihata, H. Savajols, and R. Kanungo. Recent experimental progress in nuclear halo structure studies. *Prog. Part. Nucl. Phys.*, 68:215–313, 2013.
- [78] G. Audi, M. Wang, A. H. Wapstra, F. G. Kondev, M. MacCormick, X. Xu, and B. Pfeiffer. The AME2012 atomic mass evaluation. *Chinese Physics C*, 36(12):1287, 2012.
- [79] M. Wang, G. Audi, A. H. Wapstra, F. G. Kondev, M. MacCormick, X. Xu, and B. Pfeiffer. The AME2012 atomic mass evaluation. *Chinese Physics C*, 36(12):1603, 2012.
- [80] F. Ajzenberg-Selove. Energy levels of light nuclei $A = 18-20$. *Nuclear Physics A*, 475(1):1 – 198, 1987.
- [81] D. R. Tilley et al. Energy levels of light nuclei $A=8,9,10$. *Nucl. Phys.*, A745:155–362, 2004.
- [82] F. Ajzenberg-Selove. Energy levels of light nuclei $A = 13-15$. *Nucl. Phys.*, A523:1–196, 1991.
- [83] T. Herrmann and R. Rosenfelder. A Consistent calculation of dispersion corrections in elastic electron-deuteron scattering. *Eur. Phys. J.*, A2:28–40, 1998.
- [84] C. G. Parthey, A. Matveev, J. Alnis, R. Pohl, T. Udem, U. D. Jentschura, N. Kolachevsky, and T. W. Hänsch. Precision Measurement of the Hydrogen-Deuterium $1S-2S$ Isotope Shift. *Phys. Rev. Lett.*, 104:233001, 2010.
- [85] A. Ozawa et al. Measurements of interaction cross sections for light neutron-rich nuclei at relativistic energies and determination of effective matter radii. *Nucl. Phys.*, A691:599–617, 2001.
- [86] R. Palit et al. Exclusive measurement of breakup reactions with the one-neutron halo nucleus ^{11}Be . *Phys. Rev.*, C68:034318, 2003.
- [87] N. Fukuda et al. Coulomb and nuclear breakup of a halo nucleus ^{11}Be . *Phys. Rev.*, C70:054606, 2004.
- [88] R. Kanungo et al. Proton distribution radii of $^{12-19}\text{C}$ illuminate features of neutron halos. *Phys. Rev. Lett.*, 117(10):102501, 2016.
- [89] A. Ozawa, T. Suzuki, and I. Tanihata. Nuclear size and related topics. *Nucl. Phys.*, A693:32–62, 2001.
- [90] R. W. Hackenburg. Neutron-proton effective-range parameters and zero-energy shape dependence. *Phys. Rev.*, C73:044002, 2006.
- [91] A. Calci, P. Navrátil, R. Roth, Jérémy Dohet-Eraly, S. Quaglioni, and G. Hupin. Can Ab Initio Theory Explain the Phenomenon of Parity Inversion in ^{11}Be ? *Phys. Rev. Lett.*, 117(24):242501, 2016.
- [92] G. Rupak, L. Fernando, and A. Vaghani. Radiative Neutron Capture on Carbon-14 in Effective Field Theory. *Phys. Rev.*, C86:044608, 2012.
- [93] T. Nakamura et al. Neutron capture cross section of ^{14}C of astrophysical interest studied by Coulomb breakup of ^{15}C . *Phys. Rev.*, C79:035805, 2009.
- [94] B. Acharya and D. R. Phillips. Carbon-19 in Halo EFT: Effective-range parameters from Coulomb-dissociation experiments. *Nucl. Phys.*, A913:103–115, 2013.
- [95] T. Nakamura et al. Coulomb dissociation of halo nuclei. *Nucl. Phys.*, A722:C301–C307, 2003.
- [96] V. Pascalutsa and D. R. Phillips. Effective theory of the $\Delta(1232)$ in Compton scattering off the nucleon. *Phys. Rev.*, C67:055202, 2003.
- [97] J. L. Friar, J. Martorell, and D. W. L. Sprung. Nuclear sizes and the isotope shift. *Phys. Rev.*,

- A56:4579–4586, 1997.
- [98] V. Maddalena et al. Single neutron knockout reactions: Application to the spectroscopy of $^{16,17,19}\text{C}$. *Phys. Rev.*, C63:024613, 2001.
- [99] L. Fernando, A. Vaghani, and G. Rupak. Electromagnetic form factors of one neutron halos with spin $\frac{1}{2}^+$ ground state. arXiv:1511.04054 [nucl-th].
- [100] Q. Chen et al. Measurement of the neutron-neutron scattering length using the π^-d capture reaction. *Phys. Rev.*, C77:054002, 2008.
- [101] H.-W. Hammer and S. König. Constraints on a possible dineutron state from pionless EFT. *Phys. Lett.*, B736:208–213, 2014.
- [102] J. Kirscher and D. R. Phillips. Constraining the neutron-neutron scattering length using the effective field theory without explicit pions. *Phys. Rev.*, C84:054004, 2011.
- [103] I. Tanihata et al. Measurements of Interaction Cross-Sections and Nuclear Radii in the Light p-shell Region. *Phys. Rev. Lett.*, 55:2676–2679, 1985.
- [104] J. K. Smith et al. Selective population of unbound states in ^{10}Li . *Nucl. Phys.*, A940:235–241, 2015.
- [105] M. Langevin et al. Production of neutron-rich nuclei at the limits of particle stability by fragmentation of 44 MeV/u ^{40}Ar projectiles. *Phys. Lett.*, B150:71–74, 1985.
- [106] K. Tanaka et al. Observation of a Large Reaction Cross Section in the Drip-Line Nucleus ^{22}C . *Phys. Rev. Lett.*, 104:062701, 2010.
- [107] N. Kobayashi et al. One- and two-neutron removal reactions from the most neutron-rich carbon isotopes. *Phys. Rev.*, C86:054604, 2012.
- [108] S. Mosby et al. Search for ^{21}C and constraints on ^{22}C . *Nucl. Phys.*, A909:69–78, 2013.
- [109] W. Glöckle. *The Quantum Mechanical Few-Body Problem*. Springer, Berlin, Heidelberg, 1983.
- [110] L. D. Faddeev. Scattering theory for a three particle system. *Sov. Phys. JETP*, 12:1014–1019, 1961. [*Zh. Eksp. Teor. Fiz.*39,1459(1960)].
- [111] I. R. Afnan and A. W. Thomas. Fundamentals of Three-Body Scattering Theory. *Top. Curr. Phys.*, 2:1–47, 1977.
- [112] D. L. Canham and H.-W. Hammer. Universal properties and structure of halo nuclei. *Eur. Phys. J.*, A37:367–380, 2008.
- [113] B. Acharya, C. Ji, and D. R. Phillips. Implications of a matter-radius measurement for the structure of Carbon-22. *Phys. Lett.*, B723:196–200, 2013.
- [114] K. G. Wilson. The Renormalization Group and Strong Interactions. *Phys. Rev.*, D3:1818, 1971.
- [115] S. Albeverio, R. Hoegh-Krohn, and T. T. Wu. A Class of Exactly Solvable Three-body Quantum Mechanical Problems and the Universal Low-energy Behavior. *Phys. Lett.*, A83:105–109, 1981.
- [116] T. Barford and M. C. Birse. Effective theories of scattering with an attractive inverse-square potential and the three-body problem. *J. Phys.*, A38:697–720, 2005.
- [117] R. F. Mohr, R. J. Furnstahl, R. J. Perry, K. G. Wilson, and H.-W. Hammer. Precise numerical results for limit cycles in the quantum three-body problem. *Annals Phys.*, 321:225–259, 2006.
- [118] E. Nielsen, D. V. Fedorov, A. S. Jensen, and E. Garrido. The three-body problem with short-range interactions. *Physics Reports*, 347(5):373 – 459, 2001.
- [119] C. Chin, R. Grimm, P. Julienne, and E. Tiesinga. Feshbach resonances in ultracold gases. *Rev. Mod. Phys.*, 82:1225–1286, 2010.
- [120] A. E. A. Amorim, T. Frederico, and L. Tomio. Universal aspects of Efimov states and light halo nuclei. *Phys. Rev. C*, 56:R2378, 1997.
- [121] M. T. Yamashita, T. Frederico, and L. Tomio. Trajectory of excited state of neutron-neutron- ^{18}C system. *Phys. Lett.*, B660:339–344, 2008.
- [122] T. Frederico, A. Delfino, L. Tomio, and M. T. Yamashita. Universal aspects of light halo nuclei. *Prog. Part. Nucl. Phys.*, 67:939–994, 2012.
- [123] G. Hagen, P. Hagen, H.-W. Hammer, and L. Platter. Efimov Physics Around the Neutron-Rich ^{60}Ca Isotope. *Phys. Rev. Lett.*, 111(13):132501, 2013.
- [124] Y. Togano et al. Interaction cross section study of the two-neutron halo nucleus ^{22}C . *Phys. Lett.*,

- B761:412–418, 2016.
- [125] M. T. Yamashita, R. S. Marques de Carvalho, T. Frederico, and L. Tomio. Constraints on two-neutron separation energy in the Borromean ^{22}C nucleus. *Phys. Lett.*, B697:90–93, 2011. [Erratum: *Phys. Lett.*B715,282(2012)].
 - [126] H. T. Fortune and R. Sherr. Binding energy of ^{22}C . *Phys. Rev.*, C85:027303, 2012.
 - [127] P. F. Bedaque, G. Rupak, H. W. Griebhammer, and H.-W. Hammer. Low-energy expansion in the three-body system to all orders and the triton channel. *Nucl. Phys.*, A714:589–610, 2003.
 - [128] D. L. Canham and H.-W. Hammer. Range corrections for two-neutron halo nuclei in effective theory. *Nucl. Phys.*, A 836:275–292, 2010.
 - [129] C. Ji and D. R. Phillips. Effective Field Theory Analysis of Three-Boson Systems at Next-To-Next-To-Leading Order. *Few Body Syst.*, 54:2317–2355, 2013.
 - [130] J. Vanasse. Charge and Matter Form Factors of Two-Neutron Halo Nuclei in Halo Effective Field Theory at Next-to-leading-order. *Phys. Rev.*, C95(2):024318, 2017.
 - [131] J. Vanasse. Fully Perturbative Calculation of nd Scattering to Next-to-next-to-leading-order. *Phys. Rev.*, C88(4):044001, 2013.
 - [132] A. Margaryan, R. P. Springer, and J. Vanasse. nd scattering and the A_y puzzle to next-to-next-to-next-to-leading order. *Phys. Rev.*, C93(5):054001, 2016.
 - [133] J. Vanasse. The Triton Charge Radius to Next-to-next-to-leading order in Pionless Effective Field Theory. *Phys. Rev.*, C95(2):024002, 2017.
 - [134] R. Yarmukhamedov, D. Baye, and C. Leclercq-Willain. Asymptotics of three-body bound state radial wave functions of halo nuclei. *Nucl. Phys.*, A705:335–351, 2002.
 - [135] D. Baye and E. Brainis. Zero energy determination of the astrophysical S-factor and effective range expansions. *Phys.Rev.*, C61:025801, 2000.
 - [136] X. Zhang, K. M. Nollett, and D. R. Phillips. Combining ab initio calculations and Halo EFT: the case of $^7\text{Li} + n \rightarrow ^8\text{Li} + \gamma$. *Phys. Rev. C*, 89(2):024613, 2014.
 - [137] L. Trache, A. Azhari, F. Carstoiu, H. L. Clark, C. A. Gagliardi, Y. W. Lui, A. M. Mukhamedzhanov, X. Tang, N. Timofeyuk, and R. E. Tribble. Asymptotic normalization coefficients for $^8\text{B} \rightarrow ^7\text{Be} + p$ from a study of $^8\text{Li} \rightarrow ^7\text{Li} + n$. *Phys. Rev.*, C67:062801, 2003.
 - [138] E. P. Wigner. Lower Limit for the Energy Derivative of the Scattering Phase Shift. *Phys. Rev.*, 98:145–147, 1955.
 - [139] L. B. Madsen. Effective range theory. *Am. J. Phys.*, 70:811–814, 2002.
 - [140] H.-W. Hammer and Dean Lee. Causality and universality in low-energy quantum scattering. *Phys. Lett.*, B681:500–503, 2009.
 - [141] H.-W. Hammer and Dean Lee. Causality and the effective range expansion. *Annals Phys.*, 325:2212–2233, 2010.
 - [142] J. J. Sakurai. *Modern Quantum Mechanics*. Addison-Wesley, revised edition, 1993.
 - [143] C. Ji, Ch. Elster, and D. R. Phillips. ^6He nucleus in Halo Effective Field Theory. *Phys. Rev.*, C90(4):044004, 2014.
 - [144] C. Romero-Redondo, S. Quaglioni, P. Navrátil, and G. Hupin. $^4\text{He} + n + n$ continuum within an ab initio framework. *Phys. Rev. Lett.*, 113:032503, 2014.
 - [145] L. Fernando, R. Higa, and G. Rupak. Resonance Contribution to Radiative Neutron Capture on Lithium-7. *Eur. Phys. J.*, A48:24, 2012.
 - [146] G. Rupak and R. Higa. Model-Independent Calculation of Radiative Neutron Capture on Lithium-7. *Phys. Rev. Lett.*, 106:222501, 2011.
 - [147] F. Ajzenberg-Selove. Energy levels of light nuclei A=11-12. *Nucl. Phys. A*, 506:1, 1990.
 - [148] S. Typel and G. Baur. Effective-range approach and scaling laws for electromagnetic strength in neutron-halo nuclei. *Phys. Rev. Lett.*, 93:142502, 2004.
 - [149] Nuclear Data Evaluation Project, Triangle Universities Nuclear Laboratory, Energies of Light Nuclei, <http://www.tunl.duke.edu/nucldata/>.
 - [150] M. A. Caprio. LevelScheme: A Level scheme drawing and scientific figure preparation system for Mathematica. *Comput. Phys. Commun.*, 171:107, 2005.

- [151] S. A. Rakityansky and N. Elander. Multi-channel analog of the effective-range expansion. *J. Phys.*, A44:115303, 2011.
- [152] K. M. Nollett and R. B. Wiringa. Asymptotic normalization coefficients from ab initio calculations. *Phys. Rev.*, C83:041001, 2011.
- [153] R. B. Wiringa, V. G. J. Stoks, and R. Schiavilla. An Accurate nucleon-nucleon potential with charge independence breaking. *Phys. Rev.*, C51:38–51, 1995.
- [154] B. S. Pudliner, V. R. Pandharipande, J. Carlson, and R. B. Wiringa. Quantum Monte Carlo calculations of $A \leq 6$ nuclei. *Phys. Rev. Lett.*, 74:4396–4399, 1995.
- [155] K. M. Nollett. Ab initio calculations of nuclear widths via an integral relation. *Phys. Rev.*, C86:044330, 2012.
- [156] R. A. Arndt, D. D. Long, and L. David Roper. Nucleon-alpha elastic scattering analyses. *Nucl. Phys.*, A209:429–446, 1973.
- [157] G. Hale, *private communication*, 2014.
- [158] National Nuclear Data Center, Brookhaven National Laboratory, <https://www.nndc.bnl.gov>.
- [159] B. Haesner, W. Heeringa, H. O. Klages, H. Dobiash, G. Schmalz, P. Schwarz, J. Wilczynski, B. Zeitnitz, and F. Kappeler. Measurement of the ^3He and ^4He total neutron cross sections up to 40 MeV. *Phys. Rev.*, C28:995–999, 1983.
- [160] M. E. Battat et al. Total neutron cross sections of the hydrogen and helium isotopes. *Nucl. Phys.*, 12:291, 1959.
- [161] J. Rotureau and U. van Kolck. Effective Field Theory and the Gamow Shell Model: The ^6He Halo Nucleus. *Few Body Syst.*, 54:725–735, 2013.
- [162] E. Ryberg, C. Forssén, and L. Platter. Three-body halo states in effective field theory. *Few Body Syst.*, 58:143, 2017.
- [163] J. H. Macek and J. Sternberg. Properties of pseudopotentials for higher partial waves. *Phys. Rev. Lett.*, 97:023201, 2006.
- [164] Y. Nishida and S. Tan. Liberating Efimov physics from three dimensions. *Few Body Syst.*, 51:191–206, 2011.
- [165] L. S. Brown and G. M. Hale. Field Theory of the $d + t \rightarrow n + \alpha$ Reaction Dominated by a $^5\text{He}^*$ Unstable Particle. *Phys. Rev.*, C89(1):014622, 2014.
- [166] C. A. Bertulani and G. Baur. Coincidence cross sections for the dissociation of light ions in high-energy collisions. *Nucl. Phys.*, A480:615–628, 1988.
- [167] S. Typel and G. Baur. Higher-order effects in electromagnetic dissociation of neutron halo nuclei. *Phys. Rev.*, C64:024601, 2001.
- [168] S. Typel and G. Baur. Electromagnetic strength of neutron and proton single-particle halo nuclei. *Nucl. Phys.*, A759:247–308, 2005.
- [169] C. A. Bertulani. Theory and Applications of Coulomb Excitation. arXiv:0908.4307 [nucl-th].
- [170] W. Tornow, N. G. Czakon, C. R. Howell, A. Hutcheson, J. H. Kelley, V. N. Litvinenko, S. Mikhailov, I. V. Pinayev, G. J. Weisel, and H. Witala. Low-energy photodisintegration of the deuteron and big bang nucleosynthesis. *Phys. Lett.*, B574:8–13, 2003.
- [171] J. Vanasse and M. R. Schindler. Energy dependence of the parity-violating asymmetry of circularly polarized photons in $d\gamma \rightarrow np$ in pionless effective field theory. *Phys. Rev.*, C90(4):044001, 2014.
- [172] C. A. Bertulani and G. Baur. Electromagnetic Processes in Relativistic Heavy Ion Collisions. *Phys. Rept.*, 163:299, 1988.
- [173] C. A. Bertulani and G. Baur. Relativistic coulomb collisions and the virtual radiation spectrum. *Nucl. Phys.*, A442:739–752, 1985.
- [174] P. Capel and D. Baye. Coupling-in-the-continuum effects in Coulomb dissociation of halo nuclei. *Phys. Rev.*, C71:044609, 2005.
- [175] P. Capel, *private communication*, 2017.
- [176] G. Audi and A. H. Wapstra. The 1993 atomic mass evaluation: (II) Nuclear-reaction and separation energies. *Nucl. Phys.* A565:1, 1993.

- [177] G. Audi, A. H. Wapstra, and M. Dedieu. The 1993 atomic mass evaluation: (IV) Evaluation of input data, adjustment procedures. *Nucl. Phys.* A565:193, 1993.
- [178] A. N. Antonov et al. The electron-ion scattering experiment ELISe at the International Facility for Antiproton and Ion Research (FAIR): A conceptual design study. *Nucl. Instrum. Meth.*, A637:60–76, 2011.
- [179] T. Suda et al. Nuclear physics at the SCRIT electron scattering facility. *PTEP*, 2012:03C008, 2012.
- [180] C. A. Bertulani. Probing nuclear skins and halos with elastic electron scattering. *J. Phys.*, G34:315–334, 2007.
- [181] D. R. Phillips. Electromagnetic structure of two- and three-nucleon systems: an effective field theory description. *Ann. Rev. Nucl. Part. Science*, 66:421, 2016.
- [182] C. Patrignani et al. Review of Particle Physics. *Chin. Phys.*, C40(10):100001, 2016.
- [183] R. Pohl et al. Deuteron charge radius from spectroscopy data in atomic deuterium. *Metrologica*, 54:L1, 2017.
- [184] W. Nörtershäuser et al. Nuclear Charge Radii of ${}^7\text{Be}$, ${}^9\text{Be}$, ${}^{10}\text{Be}$ and the one-neutron halo nucleus ${}^{11}\text{Be}$. *Phys. Rev. Lett.*, 102:062503, 2009.
- [185] B. Acharya, Ph.D. dissertation, Ohio University, 2015.
- [186] M. Pavón Valderrama and D. R. Phillips. Power Counting of Contact-Range Currents in Effective Field Theory. *Phys. Rev. Lett.*, 114(8):082502, 2015.
- [187] D. R. Phillips and H.-W. Hammer. Electromagnetic properties of the Beryllium-11 nucleus in Halo EFT. *EPJ Web Conf.*, 3:06002, 2010.
- [188] S. Typel and G. Baur. Scaling laws and higher-order effects in Coulomb excitation of neutron halo nuclei. *Eur. Phys. J.*, A38:355–361, 2008.
- [189] E. Kwan et al. Precision measurement of the electromagnetic dipole strengths in ${}^{11}\text{Be}$. *Phys. Lett.*, B732:210–213, 2014.
- [190] L. Koester, K. Knopf, and W. Waschkowski. Neutron scattering length of lithium and boron and their isotopes. *Z. Phys. A*, 312:81, 1983.
- [191] J. C. Blackmon, A. E. Champagne, J. K. Dickens, J. A. Harvey, M. A. Hofstee, S. Kopecky, D. C. Larson, D. C. Powell, S. Raman, and M. S. Smith. Measurement of ${}^7\text{Li}(n, \gamma){}^8\text{Li}$ cross sections at $E_n=1.5\text{--}1340$ eV. *Phys. Rev.*, C54:383–388, 1996.
- [192] A. D. Gulko, S. S. Trostin, and A. Hudoklin. Radiation asymmetry and nuclear magnetic resonance of the active nuclei produced upon capture of polarized thermal neutrons. *Sov. J. Nucl. Phys.*, 6:477, 1968.
- [193] F. C. Barker. The low-energy ${}^7\text{Be}(p, \gamma){}^8\text{B}$ cross section from an R-matrix approach. *Nucl. Phys.*, A588:693–705, 1995.
- [194] J. E. Lynn, E. T. Jurney, and S. Raman. Direct and valence neutron capture by ${}^7\text{Li}$. *Phys. Rev.*, C44:764–773, 1991.
- [195] Y. Nagai, M. Igashira, T. Takaoka, T. Kikuchi, T. Shima, A. Tomyo, A. Mengoni, and T. Otsuka. ${}^7\text{Li}(n, \gamma){}^8\text{Li}$ reaction and the S_{17} factor at $E_{c.m.} > 500$ keV. *Phys. Rev.*, C71:055803, 2005.
- [196] P. Hagen, H.-W. Hammer, and L. Platter. Charge form factors of two-neutron halo nuclei in halo EFT. *Eur. Phys. J.*, A49:118, 2013.
- [197] M. Puchalski, A. M. Moro, and K. Pachucki. Isotope Shift of the $3^2\text{S}_{1/2}$ - $2^2\text{S}_{1/2}$ Transition in Lithium and the Nuclear Polarizability. *Phys. Rev. Lett.*, 97:133001, 2006.
- [198] R. Sanchez et al. Nuclear Charge Radii of ${}^9\text{Li}$, ${}^{11}\text{Li}$: The Influence of Halo Neutrons. *Phys. Rev. Lett.*, 96:033002, 2006.
- [199] B. Acharya and D. Phillips. Properties of Lithium-11 and Carbon-22 at leading order in halo effective field theory. *EPJ Web Conf.*, 113:06013, 2016.
- [200] P. Hagen, Ph.D. dissertation, University of Bonn, 2014.
- [201] S. N. Ershov, J. S. Vaagen, and M. V. Zhukov. Binding energy constraint on matter radius and soft dipole excitations of ${}^{22}\text{C}$. *Phys. Rev.*, C86:034331, 2012.
- [202] Y. Kikuchi, T. Myo, K. Kato, and K. Ikeda. Coulomb breakup reactions of ${}^{11}\text{Li}$ in the coupled-

- channel ${}^9\text{Li}+n+n$ model. *Phys. Rev.*, C87(3):034606, 2013.
- [203] T. Nakamura et al. Observation of Strong Low-Lying E1 Strength in the Two-Neutron Halo Nucleus ${}^{11}\text{Li}$. *Phys. Rev. Lett.*, 96:252502, 2006.
- [204] X.-W. Kong and F. Ravndal. Proton-proton scattering lengths from effective field theory. *Phys. Lett.*, B450:320–324, 1999. [Erratum: *Phys. Lett.*B458,565(1999)].
- [205] X.-W. Kong and F. Ravndal. Coulomb effects in low-energy proton-proton scattering. *Nucl. Phys.*, A665:137–163, 2000.
- [206] E. Ryberg, C. Forssén, H.-W. Hammer, and L. Platter. Effective field theory for proton halo nuclei. *Phys. Rev.*, C89(1):014325, 2014.
- [207] E. Ryberg, C. Forssén, H.-W. Hammer, and L. Platter. Range corrections in Proton Halo Nuclei. *Annals Phys.*, 367:13–32, 2016.
- [208] U. van Kolck. Effective field theory of short range forces. *Nucl. Phys.*, A 645:273–302, 1999.
- [209] S. König, D. Lee, and H.-W. Hammer. Causality constraints for charged particles. *J. Phys.*, G40:045106, 2013.
- [210] R. Higa, H.-W. Hammer, and U. van Kolck. $\alpha\alpha$ Scattering in Halo Effective Field Theory. *Nucl. Phys.*, A809:171–188, 2008.
- [211] S. König, H. W. Griebhammer, H.-W. Hammer, and U. van Kolck. Effective theory of ${}^3\text{H}$ and ${}^3\text{He}$. *J. Phys.*, G43(5):055106, 2016.
- [212] H. A. Bethe. Theory of the Effective Range in Nuclear Scattering. *Phys. Rev.*, 76:38–50, 1949.
- [213] T. Barford and M. C. Birse. A Renormalization group approach to two-body scattering in the presence of long range forces. *Phys. Rev.*, C67:064006, 2003.
- [214] S.-I. Ando and M. C. Birse. Renormalization-group analysis for low-energy scattering of charged particles. *Phys. Rev.*, C78:024004, 2008.
- [215] R. Higa. Electromagnetic interactions in Halo Effective Field Theory. *EPJ Web Conf.*, 3:06001, 2010.
- [216] H.-W. Hammer and R. Higa. A Model Study of Discrete Scale Invariance and Long-Range Interactions. *Eur. Phys. J.*, A37:193–200, 2008.
- [217] S. A. Afzal, A. A. Z. Ahmad, and S. Ali. Systematic Survey of the $\alpha\alpha$ Interaction. *Rev. Mod. Phys.*, 41:247–273, 1969.
- [218] J. C. Y. Chen and A. C. Chen. Nonrelativistic off-shell two-body coulomb amplitudes. *Adv. At. Mol. Phys.*, 8:71, 1972.
- [219] R. Morlock, R. Kunz, A. Mayer, M. Jaeger, A. Muller, J. W. Hammer, P. Mohr, H. Oberhammer, G. Staudt, and V. Kolle. Halo Properties of the First $\frac{1}{2}^+$ State in ${}^{17}\text{F}$ from the ${}^{16}\text{O}(p, \gamma){}^{17}\text{F}$ Reaction. *Phys. Rev. Lett.*, 79:3837–3840, 1997.
- [220] J. T. Huang, C. A. Bertulani, and V. Guimaraes. Radiative capture of nucleons at astrophysical energies with single-particle states. *Atom. Data Nucl. Data Tabl.*, 96:824, 2010.
- [221] C. A. Gagliardi et al. Tests of transfer reaction determinations of astrophysical S - factors. *Phys. Rev.*, C59:1149–1153, 1999.
- [222] E. Ryberg, U. van Kolck, and C. Forssén. *in preparation*.
- [223] M. V. Zhukov and I. J. Thompson. Existence of proton halos near the drip line. *Phys. Rev.*, C52:3505–3508, 1995.
- [224] P. J. Woods and C. N. Davids. Nuclei beyond the proton drip-line. *Ann. Rev. Nucl. Part. Sci.*, 47:541–590, 1997.
- [225] X. Zhang, K. M. Nollett, and D.R. Phillips. Combining ab initio calculations and low-energy effective field theory for halo nuclear systems: The case of ${}^7\text{Be}+p \rightarrow {}^8\text{B}+\gamma$. *Phys. Rev. C*, 89(5):051602, 2014.
- [226] E. Ryberg, C. Forssén, H.-W. Hammer, and L. Platter. Constraining Low-Energy Proton Capture on Beryllium-7 through Charge Radius Measurements. *Eur. Phys. J. A*, 50:170, 2014.
- [227] X. Zhang, K. M. Nollett, and D. R. Phillips. Halo effective field theory constrains the solar ${}^7\text{Be} + p \rightarrow {}^8\text{B} + \gamma$ rate. *Phys. Lett.*, B751:535–540, 2015.
- [228] J.D. Walecka. *Theoretical Nuclear and Subnuclear Physics*. Oxford University Press, New York,

- 1995.
- [229] P. Navratil, R. Roth, and S. Quaglioni. Ab initio many-body calculations of nucleon scattering on ^4He , ^7Li , ^7Be , ^{12}C and ^{16}O . *Phys.Rev.*, C82:034609, 2010.
- [230] P. Navratil, R. Roth, and S. Quaglioni. Ab initio many-body calculation of the $^7\text{Be}(p,\gamma)^8\text{B}$ radiative capture. *Phys. Lett.*, B 704:379–383, 2011.
- [231] A. R. Junghans, K. A. Snover, E. C. Mohrmann, E. G. Adelberger, and L. Buchmann. Updated S-factors for the $^7\text{Be}(p,\gamma)^8\text{B}$ reaction. *Phys.Rev.*, C81:012801, 2010.
- [232] B. W. Filippone, A. J. Elwyn, C. N. Davids, and D. D. Koetke. Proton capture cross section of ^7Be and the flux of high-energy solar neutrinos. *Phys.Rev.*, C28:2222–2229, 1983.
- [233] L. T. Baby et al. A New precision measurement of the $^7\text{Be}(p,\gamma)^8\text{B}$ cross-section with an implanted ^7Be target. *Phys. Rev. Lett.*, 90:022501, 2003.
- [234] L. T. Baby et al. A New measurement of the proton capture rate on ^7Be and the $S_{17}(0)$ factor. *Phys.Rev.*, C67:065805, 2003.
- [235] F. Hammache, G. Bogaert, P. Aguer, C. Angulo, S. Barhoumi, et al. New measurement and analysis of the $^7\text{Be}(p,\gamma)^8\text{B}$ cross-section. *Phys.Rev.Lett.*, 80:928–931, 1998.
- [236] F. Hammache, G. Bogaert, P. Aguer, C. Angulo, S. Barhoumi, et al. Low-energy measurement of the $^7\text{Be}(p,\gamma)^8\text{B}$ cross-section. *Phys.Rev.Lett.*, 86:3985–3988, 2001.
- [237] X. Zhang, K. M. Nollett, and D. R. Phillips. How well do we understand $^7\text{Be} + p \rightarrow ^8\text{B} + \gamma$? An Effective Field Theory perspective. *EPJ Web Conf.*, 113:06001, 2016.
- [238] E. G. Adelberger et al. Solar fusion cross sections II: the pp chain and CNO cycles. *Rev.Mod.Phys.*, 83:195, 2011.
- [239] R. D. Williams and S. E. Koonin. Direct capture cross sections at low energy. *Phys. Rev. C*, 23:2773–2774, 1981.
- [240] D. Baye. Behavior of the $^7\text{Be}(p,\gamma)^8\text{B}$ astrophysical S-factor near zero energy. *Phys.Rev.*, C62:065803, 2000.
- [241] D. Baye. Behaviour of radiative-capture reactions near zero energy. *Nucl. Phys.*, A758:114–117, 2005.
- [242] B. K. Jennings, S. Karataglidis, and T.D. Shoppa. Direct capture astrophysical S-factors at low-energy. *Phys.Rev.*, C58:579–581, 1998.
- [243] B. K. Jennings, S. Karataglidis, and T.D. Shoppa. Extrapolation of the astrophysical S-factor for $^7\text{Be}(p,\gamma)^8\text{B}$ to solar energies. *Phys.Rev.*, C58:3711–3721, 1998.
- [244] B. K. Jennings. Low-energy behavior of the $^7\text{Be}(p,\gamma)^8\text{B}$ reaction. *Phys.Rev.*, C62:027602, 2000.
- [245] R. H. Cyburt, B. Davids, and B. K. Jennings. Determination of $S_{17}(0)$ from published data. *Phys.Rev.*, C70:045801, 2004.
- [246] A. M. Mukhamedzhanov and F. M. Nunes. Low-energy behavior of the astrophysical S-factor in radiative captures to loosely bound final states. *Nucl.Phys.*, A708:437–459, 2002.
- [247] R. F. Christy and I. Duck. γ rays from an extranuclear direct capture process. *Nucl. Phys. A*, 24:89–101, 1961.
- [248] B. K. Jennings, S. Karataglidis, and T. D. Shoppa. Extrapolation of the astrophysical S-factor for $^7\text{Be}(p,\gamma)^8\text{B}$ to solar energies. *Phys. Rev. C*, 58:3711–3721, 1998.
- [249] P. Descouvemont. Reanalysis of the $^7\text{Be}(p,\gamma)^8\text{B}$ S-factor in a microscopic model. *Phys.Rev.*, C70:065802, 2004.
- [250] P. Capel, P. Danielewicz, and F. M. Nunes. Deducing spectroscopic factors from wave-function asymptotics. *Phys. Rev.*, C82:054612, 2010.
- [251] D. John Millener, J. W. Olness, E. K. Warburton, and S. S. Hanna. Strong E1 transitions in ^9Be , ^{11}Be , and ^{13}C . *Phys. Rev.*, C28:497–505, 1983.
- [252] P. Navratil, V. G. Gueorguiev, J. P. Vary, W. E. Ormand, and A. Nogga. Structure of $A=10-13$ nuclei with two- plus three-nucleon interactions from chiral effective field theory. *Phys. Rev. Lett.*, 99:042501, 2007.
- [253] P. Navratil, C. A. Bertulani, and E. Caurier. $^7\text{Be}(p,\gamma)^8\text{B}$ S-factor from ab initio wave functions. *Phys. Lett.*, B634:191–194, 2006.

- [254] P. Navrátil, C. A. Bertulani, and E. Caurier. ${}^7\text{Be}(p, \gamma){}^8\text{B}$ S-factor from ab initio no-core shell model wave functions. *Phys. Rev.*, C73:065801, 2006.
- [255] S. Baroni, P. Navrátil, and S. Quaglioni. Unified ab initio approach to bound and unbound states: no-core shell model with continuum and its application to ${}^7\text{He}$. *Phys. Rev.*, C87(3):034326, 2013.
- [256] P. Navrátil, S. Quaglioni, G. Hupin, C. Romero-Redondo, and Angelo Calci. Unified ab initio approaches to nuclear structure and reactions. *Phys. Scripta*, 91(5):053002, 2016.
- [257] S. Quaglioni and P. Navrátil. Ab Initio Many-Body Calculations of n - ${}^3\text{H}$, n - ${}^4\text{He}$, p - ${}^3,4\text{He}$, and n - ${}^{10}\text{Be}$ Scattering. *Phys. Rev. Lett.*, 101:092501, 2008.
- [258] G. Hupin, J. Langhammer, P. Navrátil, S. Quaglioni, A. Calci, and R. Roth. Ab initio many-body calculations of nucleon- ${}^4\text{He}$ scattering with three-nucleon forces. *Phys. Rev.*, C88(5):054622, 2013.
- [259] S. Quaglioni, C. Romero-Redondo, and P. Navrátil. Three-cluster dynamics within an ab initio framework. *Phys. Rev.*, C88:034320, 2013. [Erratum: *Phys. Rev.*C94,no.1,019902(2016)].
- [260] C. Romero-Redondo, S. Quaglioni, P. Navrátil, and G. Hupin. How many-body correlations and α -clustering shape ${}^6\text{He}$. *Phys. Rev. Lett.*, 117(22):222501, 2016.
- [261] G. Papadimitriou, J. Rotureau, N. Michel, M. Płoszajczak, and B. R. Barrett. Ab initio No-Core Gamow Shell Model calculations with realistic interactions. *Phys. Rev.*, C88(4):044318, 2013.
- [262] K. Fosse, N. Michel, M. Płoszajczak, Y. Jaganathen, and R. M. Id Betan. Description of the proton and neutron radiative capture reactions in the Gamow shell model. *Phys. Rev.*, C91(3):034609, 2015.
- [263] Y. Jaganathen, N. Michel, and M. Płoszajczak. Gamow shell model description of proton scattering on ${}^{18}\text{Ne}$. *Phys. Rev.*, C89(3):034624, 2014.
- [264] S. C. Pieper. Quantum Monte Carlo calculations of light nuclei. *Riv. Nuovo Cim.*, 31:709–740, 2008.
- [265] S. König and D. Lee. Volume Dependence of N-Body Bound States. arXiv:1701.00279 [hep-lat].
- [266] T. Teichmann. On the interpretation of resonance levels and their widths in terms of the scattering length and the effective range. *Phys. Rev.*, 83(1):141, 1951.
- [267] G. M. Hale, L. S. Brown, and M. W. Paris. Effective field theory as a limit of R-matrix theory for light nuclear reactions. *Phys. Rev.*, C89(1):014623, 2014.
- [268] R. J. Furnstahl, D. R. Phillips, and S. Wesolowski. A recipe for EFT uncertainty quantification in nuclear physics. *J. Phys.*, G42(3):034028, 2015.
- [269] S. Wesolowski, N. Klco, R. J. Furnstahl, D. R. Phillips, and A. Thapaliya. Bayesian parameter estimation for effective field theories. *J. Phys.*, G43(7):074001, 2016.
- [270] C. R. Brune, J. A. Caggiano, D. B. Sayre, A. D. Bacher, G. M. Hale, and M. W. Paris. R-matrix description of particle energy spectra produced by low-energy ${}^3\text{H}+{}^3\text{H}$ reactions. *Phys. Rev.*, C92(1):014003, 2015.
- [271] A. Gal, E. V. Hungerford, and D. J. Millener. Strangeness in nuclear physics. *Rev. Mod. Phys.*, 88(3):035004, 2016.
- [272] M. Juric et al. A new determination of the binding-energy values of the light hypernuclei ($15 \geq A$). *Nucl. Phys.*, B52:1–30, 1973.
- [273] D. H. Davis. A brief review of emulsion results on hypernuclei. *AIP Conf. Proc.*, 224:38–48, 1991.
- [274] S.-I. Ando, G.-S. Yang, and Y. Oh. ${}_{\Lambda\Lambda}{}^4\text{H}$ in Halo Effective Field Theory. *Phys. Rev.*, C89(1):014318, 2014.
- [275] J. Haidenbauer, S. Petschauer, N. Kaiser, Ulf-G. Meißner, A. Nogga, and W. Weise. Hyperon-nucleon interaction at next-to-leading order in chiral effective field theory. *Nucl. Phys.*, A915:24–58, 2013.
- [276] T. A. Rijken, V. G. J. Stoks, and Y. Yamamoto. Soft core hyperon-nucleon potentials. *Phys. Rev.*, C59:21–40, 1999.
- [277] J. Haidenbauer and U.-G. Meißner. The Jülich hyperon-nucleon model revisited. *Phys. Rev.*,

- C72:044005, 2005.
- [278] H.-W. Hammer. The Hypertriton in effective field theory. *Nucl. Phys.*, A705:173–189, 2002.
- [279] C. Rappold et al. Search for evidence of ${}^3_{\Lambda}n$ by observing $d + \pi^-$ and $t + \pi^-$ final states in the reaction of ${}^6\text{Li} + {}^{12}\text{C}$ at 2A GeV. *Phys. Rev.*, C88(4):041001, 2013.
- [280] S.-I. Ando, U. Raha, and Y. Oh. Investigation of the $nn\Lambda$ bound state in pionless effective theory. *Phys. Rev.*, C92(2):024325, 2015.
- [281] H. Takahashi et al. Observation of a ${}^6_{\Lambda\Lambda}\text{He}$ double hypernucleus. *Phys. Rev. Lett.*, 87:212502, 2001.
- [282] J. K. Ahn et al. Double- Λ hypernuclei observed in a hybrid emulsion experiment. *Phys. Rev.*, C88(1):014003, 2013.
- [283] S.-I. Ando and Y. Oh. ${}_{\Lambda\Lambda}{}^6\text{He}$ in cluster effective field theory. *Phys. Rev.*, C90(3):037301, 2014.
- [284] W. Gloeckle and H. Kamada. On the inclusion of 3N-forces into the 4N-Yakubovsky equations. *Nucl. Phys.*, A560:541–547, 1993.
- [285] L. Platter, H.-W. Hammer, and U.-G. Meißner. On the correlation between the binding energies of the triton and the alpha-particle. *Phys. Lett.*, B607:254–258, 2005.
- [286] J. von Stecher, J. P. D’Incao, and Chris H. Greene. Signatures of universal four-body phenomena and their relation to the efimov effect. *Nat. Phys.*, 5(6):417–421, 2009.
- [287] D. Blume and C. H. Greene. Monte carlo hyperspherical description of helium cluster excited states. *J. Chem. Phys.*, 112(18):8053–8067, 2000.
- [288] A. Deltuva. Dimer-atom-atom recombination in the universal four-boson system. *Few Body Syst.*, 54:2419–2425, 2013.
- [289] S. E. Pollack, D. Dries, and R. G. Hulet. Universality in three- and four-body bound states of ultracold atoms. *Science*, 326(5960):1683–1685, 2009.
- [290] M. Zaccanti et al. Observation of an efimov spectrum in an atomic system. *Nat Phys*, 5(8):586–591, 2009.
- [291] F. Ferlaino et al. Evidence for Universal Four-Body States Tied to an Efimov Trimer. *Phys. Rev. Lett.*, 102:140401, 2009.
- [292] M. Kunitski et al. Observation of the Efimov state of the helium trimer. *Science*, 348:551–555, 2015.
- [293] C. Werntz and H. Überall. Collective nuclear ”breathing mode” model with application to ${}^4\text{He}$ monopole state. *Phys. Rev.*, 149:762–767, 1966.
- [294] E. Hiyama, B. F. Gibson, and M. Kamimura. Four-body calculation of the first excited state of He-4 using a realistic nn interaction: ${}^4\text{He}(e, e'){}^4\text{He}(0_2^+)$ and the monopole sum rule. *Phys. Rev.*, C70:031001, 2004.
- [295] S. Bacca, N. Barnea, W. Leidemann, and G. Orlandini. Examination of the first excited state of ${}^4\text{He}$ as a potential breathing mode. *Phys. Rev. C*, 91:024303, 2015.
- [296] G. D. Alkhazov et al. Nuclear Matter Distributions in ${}^6\text{He}$ and ${}^8\text{He}$ from Small Angle p -He Scattering in Inverse Kinematics at Intermediate Energy. *Phys. Rev. Lett.*, 78:2313–2316, 1997.
- [297] A. Lagoyannis et al. Probing the ${}^6\text{He}$ halo structure with elastic and inelastic proton scattering. *Phys. Lett.*, B518:27–33, 2001.
- [298] S. R. Neumaier et al. Small-angle proton elastic scattering from the neutron-rich isotopes ${}^6\text{He}$ and ${}^8\text{He}$, and from ${}^4\text{He}$, at 0.7 GeV in inverse kinematics. *Nucl. Phys.*, A712:247–268, 2002.
- [299] Y. Kondo et al. Low-lying intruder state of the unbound nucleus ${}^{13}\text{Be}$. *Phys. Lett.*, B690:245–249, 2010.
- [300] Y. Aksyutina et al. Structure of the unbound nucleus ${}^{13}\text{Be}$: One-neutron knockout reaction data from ${}^{14}\text{Be}$ analyzed in a holistic approach. *Phys. Rev.*, C87(6):064316, 2013.
- [301] A. Sanetullaev et al. Investigation of the role of ${}^{10}\text{Li}$ resonances in the halo structure of ${}^{11}\text{Li}$ through the ${}^{11}\text{Li}(p, d){}^{10}\text{Li}$ transfer reaction. *Phys. Lett.*, B755:481–485, 2016.
- [302] I. Tanihata et al. Measurement of two-halo neutron transfer reaction $p({}^{11}\text{Li}, {}^9\text{Li})t$ at 3A MeV. *Phys. Rev. Lett.*, 100:192502, 2008.

- [303] R. Kanungo et al. Structure of states in ^{12}Be via the $^{11}\text{Be}(d, p)$ reaction. *Phys. Lett.*, B682:391–395, 2010.
- [304] K. T. Schmitt et al. Halo nucleus ^{11}Be : A Spectroscopic study via neutron transfer. *Phys. Rev. Lett.*, 108:192701, 2012.
- [305] J. Casal, M. Gómez-Ramos, and A. M. Moro. Description of the $^{11}\text{Li}(p, d)^{10}\text{Li}$ transfer reaction using structure overlaps from a full three-body model. *Phys. Lett.*, B767:307–313, 2017.
- [306] D. Baye, P. Capel, and G. Goldstein. Collisions of Halo Nuclei within a Dynamical Eikonal Approximation. *Phys. Rev. Lett.*, 95:082502, 2005.
- [307] G. Goldstein, D. Baye, and P. Capel. Dynamical eikonal approximation in breakup reactions of ^{11}Be . *Phys. Rev.*, C73:024602, 2006.
- [308] A. M. Moro and F. M. Nunes. Transfer to the continuum and breakup reactions. *Nucl. Phys.*, A767:138–154, 2006.
- [309] N. J. Upadhyay, A. Deltuva, and F. M. Nunes. Testing the continuum discretized coupled channel method for deuteron induced reactions. *Phys. Rev.*, C85:054621, 2012.
- [310] A. Deltuva. Faddeev-type calculation of (d, n) transfer reactions in three-body nuclear systems. *Phys. Rev.*, C92(6):064613, 2015.
- [311] A. Deltuva, A. Ross, E. Norvaišas, and F. M. Nunes. Role of core excitation in (d, p) transfer reactions. *Phys. Rev.*, C94(4):044613, 2016.